Title
First-principles Simulations of Minerals in Earth and Planetary Interiors

Author
Zhang, Shuai

Publication Date
2016

Peer reviewed|Thesis/dissertation

First-principles Simulations of Minerals in Earth and Planetary Interiors

by

Shuai Zhang

A dissertation submitted in partial satisfaction of the

requirements for the degree of

Doctor of Philosophy

in

Earth & Planetary Science

and the Designated Emphasis

in

Computational Science and Engineering

in the

Graduate Division

of the

University of California, Berkeley

Committee in charge:

Associate Professor Burkhard Militzer, Chair
Professor Raymond Jeanloz
Professor Mark Asta

Fall 2016

First-principles Simulations of Minerals in Earth and Planetary Interiors

Abstract

First-principles Simulations of Minerals in Earth and Planetary Interiors

by

Shuai Zhang

Doctor of Philosophy in Earth & Planetary Science

and the Designated Emphasis in Computational Science and Engineering

University of California, Berkeley

Associate Professor Burkhard Militzer, Chair

In the deep interiors of planets, the pressures and the temperatures are significantly higher than at ambient condition. The interplay between compression and thermal expansion leads to complexity in the chemistry and physical properties of minerals. Improved knowledge of the behavior of dominant minerals inside the Earth and other planets is essential for understanding the structure, dynamics, and evolution of planetary systems.

In this dissertation, I study materials in environments ranging from the deep mantle of the Earth to the core boundary of Jovian planets and to stellar interiors, using computer simulation with first-principles methods. The contents of this dissertation are as follows: Chapters 1-2 provide an overview of Earth and planetary minerals, and a background of first-principles computer simulation methodology. Chapter 3[1] discusses the thermoelasticity of iron- and aluminum-bearing $MgSiO_3$ in the Earth's lower-mantle. Chapter 4[2] is about novel phases of hydrogen-oxygen compounds at giant-planet interior conditions. Chapter 5 presents an equation of state of warm dense sodium. We conclude that lower-mantle mineralogy is in accord with the pyrolite model; we demonstrate that minerals can have counter-intuitive stoichiometry and phases at high pressure; and we provide a coherent first-principles equation of state table of sodium in a wide range of density and temperature conditions. This work illustrates the importance of first-principles simulations as powerful tools in Earth and planetary science studies. Finally, chapter 6 discusses possible directions for future work in the field of computational mineral physics.

[1]Chapter 3 has been published as S. Zhang, S. Cottaar, T. Liu, S. Stackhouse, and B. Militzer, *Earth Planet. Sci. Lett.*, vol. 434, pp. 264-273, 2016.

[2]Chapter 4 has been published as S. Zhang, H. Wilson, K. Driver, and B. Militzer, *Phys. Rev. B*, vol. 87, p. 024112, 2013.

To those who loved me.

Contents

List of Figures

List of Tables

Acknowledgments

First of all, I want to thank my advisor, Prof. Burkhard Militzer, for his beneficiary advice and continuous support. His in-depth understanding of problems, wide knowledge in physics and planetary science, and rich experience in programming helped me a lot by offering suggestions or solutions to problems that came up during my research. His efforts in always being available, attention to details, and encouragement made it a great experience working with him and other colleagues in the group.

Second, I would like to give special thanks to Profs. Raymond Jeanloz, Rudy Wenk, and Mark Asta, who are committee members of my qualification exam. Raymond supervised my side project, *multi-single-crystal X-ray diffraction experiment for studying the spin transition in ferropericlase*. From developing ideas and designing the experiment, beamtime application, to the experimental details, he shared insightful ideas with me and gave me great advice and incredible support and patience. Rudy always welcome my dropping by his office and asking questions related to texture, X-ray diffraction, and high-pressure experiments. I didn't meet Mark often after switching the major research topic, but I benefited a lot from his suggestions of taking the class on phase transformation, alternative ideas in treating the spin transition problem, and lecture on materials database. It has also been a nice experience knowing his students Kevin Ding and Maarten de Jong.

I want to thank Prof. Barbara Romanowicz, for starting the CIDER program for senior and junior geoscientists from across disciplines to gather and work together. I learned a lot from the summer program in 2014, the community meeting in 2016, and several pre- or post-AGU workshops. I appreciate Prof. Bruce Buffett for his guidance when I was trying to learn some basics in geodynamic modeling, and his help when I was a reader for his class EPS102: History and evolution of planet Earth. His class on fluid dynamics is great and I enjoyed his lectures a lot. I also have to thank Prof. Michael Manga, for his amazing style of teaching EPS50 that benefited me when I was preparing for my qualification exam, his contribution to a GRL paper by our CIDER research group, and the years of commitment in being a graduate advisor.

I owe much to my group members and visitors, Kevin Driver, François Soubiran, Sean Wahl, Tanis Leonhardi, and Stephen Stackhouse, and past members Hugh Wilson and Josh Tollefson, for the great experience working together, numerous talks on research, and their tremendous help with my preparation and application for academic jobs. I would also like to thank Raymond's group members, Zack Geballe who has been a great mentor to me, Budhiram K. Godwal and Marius Millot with whom I had many interesting discussions, Mu Eric Li who became a great friend and collaborator, Matthew Diamond and Thomas Smart for their commitment in my experimental project, and Henry Tang who was a nice officemate and friend.

I would also like to thank past and present EPS graduate student fellows, Heidi Fuqua, with whom I had a lot of fun climbing rocks and making friends with people in and outside the department, also Felipe Orellana, Brent Delbridge, Eloisa Zepeda-alarcon, Qingkai Kong, Cheng Cheng, Seth Saltiel, Sierra Boyd and Benjamin Nault, for studying together in the past

five years, and many others including Sanne Cottaar, Pamela Kaercher, Jesse Day, Percy Link, Ian Rose, Tushar Mittal, Avinash Nayak, Andrea Chiang, Mong-Han Huang, Nick Knezek, Elizabeth Niespolo, William Hawley, Carolina Muñoz, Scott French, Allen Zheng, Shuo Zhang, Jiabin Liu, Marissa Tremblay, Stephanie Wuerth, Daniele Rosa, Xueling Liu, Tyler Arbour, Daniella Rempe, David Mangiante, Noah Randolph-flagg, Stephen Breen, Liz Mitnick, Robert Citron, Kathryn Materna, Laura MacLean, Hannah Bourne, Shan Dou, Jennifer Frederick, and postdocs Kaiqing Yuan and Lingsen Meng, for their help in work or life.

I appreciate present and past EPS staff, Margie Winn, Roxanne Polk, Crysthel Catambay, Charley Paffenbarger, Judith Coyote, Nadine Spingola-Hutton, Goldie Negelev, Rachel Kowalik, Niraj Raman, Timothy Teague, Elana Sabolch, Marion Banks, Micaelee Ellswythe, Raluca Iordache, Gretchen vonDuering, Allyson Tang, and Jann Michael Pagdanganan for their help with all sorts of questions regarding working, studying, and living in McCone and at Berkeley. I cannot imagine how my past five years would be without their effort in making EPS such a lovely place.

Last but not the least, I am grateful to my family—my mother, my brother, my sister, and my wife. Life changes, but the love and support from them never fade.

Financial support from UC Berkeley Graduate Student Fellowship, Graduate Division Conference Travel Grant, CIDER, NSF, DOE, and NASA, and computational resources including NCAR, NERSC, Research Computing at University of Colorado Boulder, and UC Berkeley EPS/Astronomy clusters, are acknowledged.

Chapter 1

Overview

The world is richer than it is possible to express in any single language. - Ilya Prigogine

Deep inside the Earth and giant planets, materials are under extremely high pressures and temperatures, up to millions of times atmosphere pressure and thousands of degrees temperature. Diverse minerals and phases exist under these conditions; together they govern the specific dynamics of each planet, with differences depending on each planet's particular formation and evolution history. The chemistry and physics of minerals and their assemblages under high-pressure, temperature conditions determine the properties of planet interiors, which are dynamically related to geological signatures at the surface via convection. Therefore, the study of minerals under extreme conditions plays an important role in Earth and planetary science, and is fundamental for human beings to explore the solar system and beyond.

The basic physical quantity that governs the stability of phases at a given pressure (P) and temperature (T) is the Gibbs free energy $G = U + PV - TS$, where U is the internal energy, PV and TS correspond to the pressure-volume and the temperature-entropy term, respectively. The lower in G, the more stable a phase is. Therefore, for phases with similar internal energy, high pressure tends to stabilize those with smaller volumes, while high temperature eases the formation of those with higher entropies. Competition between the two factors leads to the particular stability region of each phases of a material. The boundary between phases is usually characterized by the Clapeyron slope, which is related to the changes in volume and entropy associated with the phase transition via $dP/dT = \Delta S/\Delta V$. The Clapeyron slope can be positive (for instance the perovskite to post-perovskite transition of $MgSiO_3$) or negative (such as the B1-B2 transition of MgO), leading to variations in the depth of phase transition in regions with temperature anomaly [1].

Some important questions for theorists include: 1) how to accurately calculate G to determine the most stable phases out of a group of candidate structures? 2) how to precisely obtain the energy-pressure-temperature-volume relations (E-P-T-V relations, or the equation of state) and properties of a system, once the structure is known? and 3) how to guide the design of expensive experiments, or verify and explain experimental discoveries?

Atomic-scale first-principles simulations have been playing important roles in seeking answers to these questions [2]. In this chapter, we introduce the interior of the Earth along with the possible structures of Jovian and extrasolar planets, followed by some important questions for mineral physicists and methods in high-pressure studies. Details of first-principles methods will be described in the next chapter.

1.1 The interior of the Earth and other planets

The interior of the Earth is in layers, as has been found by seismological and geodynamic observations. It consists primarily of the mantle, which is likely dominantly silicates and oxides, and the core, which is presumably Fe-Ni alloys with some light elements [3, 4]. Based on seismic characteristics, the mantle is divided into the upper mantle (from the bottom of the crust to 410 km depth), the transition zone (410-660 km), and the lower mantle (660-2891 km). The primary rock in the upper mantle (less than $\sim$7 GPa) is peridotite, which consists of olivine, pyroxene, and garnet [5]. With increasing pressure, at lower mantle depths (24-127 GPa), these minerals transform into bridgmanite, ferropericlase, calcium silicate perovskite, etc. [6] Up to a few hundred kilometers above the core-mantle boundary ($\sim$136 GPa), there exists the D$''$ layer, which is characterized by strong seismic anomalies and lateral heterogeneities. Deeper, in the core region, there is a liquid layer known as the outer core (2891-5150 km, 136-329 GPa), surrounding a solid inner core (5150-6371 km, 329-364 GPa) that has complex anisotropic structure [7]. It is noteworthy that the detailed mineral composition of the lower mantle (and likewise the core) is still in question, which is a topic discussed in great detail in Chapter 3 of this dissertation.

In comparison with the Earth, knowledge of giant-planet interiors is much more limited due to the lack of seismological constraints. Despite this, data from observations using telescopes and spacecrafts have helped construct models of the internal structures and compositions of Jovian planets [8]. Uranus and Neptune may each have a small rocky core surrounded by a thick layer of ice-hydrogen-rock mixture, and an outermost layer consisting of hydrogen, helium, and ice. Jupiter and Saturn each may have a small ice-rock core, which is enveloped by a very thick layer of hydrogen-helium mixtures. Here the "ices" refer to hydrides of oxygen, carbon, and nitrogen that are next to hydrogen, helium and neon in abundance; water, methane, and ammonia are examples [9]. Novel structures, such as a superionic state, have been predicted for these ices and altered our understanding of Uranus and Neptune [10, 11]. Chapter 4 and a few more works [12, 13] during my doctorate study are toward this end.

Even less is known about the interiors and compositions of exoplanets, the confirmed number of which has reached 2951 as of Aug. 5, 2016. Most of the planets recently discovered by the Kepler mission [14] are larger than the Earth and likely similar to Jovian planets. Comparing the planets' mass-radius data with the equation of state (EOS) of typical planet-forming materials enables estimating these planets' compositions [15, 16]. This gives one example that reflects the importance of EOS calculations. In fact, many areas,

including shock wave experiments, stellar physics, and high energy density physics, require EOS information. In Chapter 5 we provide the first EOS calculation for sodium over wide temperature and pressure ranges.

1.2 Essential questions for mineral physicists

In order to understand the formation and evolution of the Earth, Jovian planets, and other planets beyond the solar system, it is important to have an understanding of the fundamental components—the minerals: their various chemistry, phases, and physical properties at high temperatures and pressures corresponding to the interiors of these planets.

In the Earth's lower mantle as well as the rocky parts of Jovian and many extrasolar planets' interiors, the most important systems to study are $(Mg_{1-x-y}Fe_xAl_y)(Si_{1-x'-y'}Fe_{x'}Al_{y'})O_3$, $Mg_{1-x}Fe_xO$, SiO_2, and $CaSiO_3$. Areas of study include the structure, texture, mechanical properties (compression behavior, elasticity, etc.), transport properties (viscosity, thermal diffusivity and conductivity), and the phase diagrams of each individual system as well as their mixtures, at pressures spanning $10^5 - 10^7$ times atmosphere condition. Accurate data in these aspects are required for interpreting global and regional seismic anomalies observed in the mantle, particularly in core-mantle boundary regions. Their physical properties are also important for constraining geodynamic models of mantle convection and evolution, core-mantle interactions, and plate tectonics.

The Earth's core is of particular importance, where the flow of iron-rich fluid sustains the planet's magnetic field. The structure, density-pressure relation, and sound velocities [17] of Fe and Fe-X (X≡Si, O, S, etc.) alloys are useful for estimating the core's composition; the phase diagrams of these alloys and the behavior of the light elements [18, 19] are important for constraining the inner-outer core boundary and growth of the inner core; the melting temperature [20] constrains the mantle geotherm; and the thermal conductivity [21, 22] defines the heat flux that is important for understanding the Earth's magnetic field and the formation of the solid inner core. Tremendous effort has been invested in working on these topics, but the composition and state of the core remain uncertain.

One common feature of the above questions is the condition of high pressure. At megabar pressures, materials may exhibit new crystal structures or behaviors that are distinct from those in ambient conditions. For example, at 0 GPa, d electrons of Fe^{2+} in (Mg,Fe)O ferropericlase are in a state with high spin number ($\mathcal{S} = 2$), as indicated by Hund's rules. This "high-spin" state is no longer stable at mid-lower mantle pressure (∼40 GPa), but transitions into a "low-spin" state with $\mathcal{S} = 0$, because the changes in crystal field splitting energy surpasses the spin-paring energy, at such high pressures. The spin transition is often believed to be associated with significant softening in the bulk modulus [23] and increase in shear anisotropy [24], potentially resulting in dramatic changes in the partitioning of iron between bridgmanite and ferropericlase [25]. Such results are useful for geodynamic studies, and may explain lateral heterogeneities in seismic observations [26]. Here we highlight an additional effect of high pressure on materials, where stable phases can have counter-intuitive

stoichiometry [27], because of the changes in electronic interaction and lattice dynamics due to compression. These factors should be considered seriously when studying materials at deep-interior conditions of planets.

1.3 Methods in high-pressure studies

Techniques for studying materials at high-pressure conditions have seen substantial developments over the last few decades. There are two major experimental techniques—static compression and dynamic compression. The former is often performed using a large-volume press, such as the multi-anvil apparatus [28] that can usually attain pressures of ∼30 GPa (top of the lower mantle) and sometimes ∼100 GPa, or diamond anvil cells [29], which are capable of reaching pressures higher than 360 GPa (center of the Earth). Dynamic compression techniques involve driving a shock wave through the material using a gas gun[1], intensive laser[2], or high magnetic fields[3]. These can achieve pressures and temperatures greater than that at the center of Jupiter, and therefore plays a special role in studies of Earth and planetary interiors [30].

Static compression has the advantage of flexibility in reaching a wide range of desired temperatures and pressures. Large volume press allows operating with samples in the sizes of centimeters, which is advantageous in studying equilibrium phase relations by analyzing the recovered samples after the pressing, heating, and quenching procedure. Diamond anvil cells are frequently used for studying isolated materials up to very high pressures. The progress in this technique has benefited greatly from the development of new-generation synchrotron radiation facilities, which provide high-energy X-ray beams that are useful to determine the structure of μm-sized samples confined in chambers with limited opening angles.

Dynamic compression utilizes shock waves to generate high pressures, which are often accompanied by simultaneous high temperatures. This technique is particularly useful for measuring EOS and detecting phase transitions under extreme P-T conditions. In a shock wave experiment, the state that a target mineral can reach is along specific paths that are governed by the EOS. Therefore, one can use theoretical models or calculations to provide EOS to guide the design of experiments, which improves the efficiency and can in turn verify the theoretical data. Techniques such as pre-compression and multi-shock allows reaching states off the principle Hugoniots, and ramp compression enables high pressure measurements at low temperatures, which can be useful for studying pressure-driven phase transformations predicted by ground-state first-principles calculations.

In addition to the collaboration between experiment and simulation, the mineral physics community also has traditionally worked closely with other disciplines, such as seismology, geodynamics, geochemistry, and planetary science. Such multi-discipline synergy is very

[1]E.g., Lindhurst Laboratory for Experimental Geophysics at California Institute of Technology, and more resources listed on http://mygeologypage.ucdavis.edu/stewart/OLDSITE/ImpactLabs.html.

[2]E.g., National Ignition Facility at Lawrence Livermore National Laboratory.

[3]E.g., Z Machine at Sandia National Laboratories.

important for obtaining a complete and convincing picture on the origin and evolution of the Earth and other planets.

Chapter 2

First-principles Methods

God used beautiful mathematics in creating the world. - Paul Dirac

In quantum chemistry, first-principles methods (usually also called *ab initio* methods) refer to methods that start from physical constants, including the light velocity c, Planck constant h, electron mass m_e and charge e, and are based on physical models that do not rely on any specific experiment or observational constraints, while approximations are made. In studies of minerals in Earth and planetary interiors, first-principles methods based on density functional theory (DFT) or quantum Monte Carlo (QMC) are often used. This chapter introduces the theoretical and computational backgrounds of some of these methods, which are closely relevant to the studies in this thesis. In this discussion we divide these techniques into two broad classes: ground-state and finite-temperature.

2.1 Introduction

The starting point to describe a system of electrons and nuclei is the Shrödinger equation

$$\hat{\mathcal{H}}\Phi\{\boldsymbol{r}_i, \boldsymbol{R}_I\} = \mathcal{E}_s\Phi\{\boldsymbol{r}_i, \boldsymbol{R}_I\}. \tag{2.1}$$

In this equation, $\Phi\{\boldsymbol{r}_i, \boldsymbol{R}_I\}$ is the wavefunction of the system, $\mathcal{E}_s$ is the energy, the Hamiltonian[1]

$$\begin{aligned}\hat{\mathcal{H}} &= \hat{T} + V_{\text{ext}} + V_{\text{ee}} + \hat{T}_N + V_{NN} \\ &= -\sum_i \frac{\hbar^2}{2m_e}\nabla_i^2 - \sum_{i,I} \frac{Z_I e^2}{|\boldsymbol{r}_i - \boldsymbol{R}_I|} + \sum_{\substack{i,j \\ (i\neq j)}} \frac{e^2}{2|\boldsymbol{r}_i - \boldsymbol{r}_j|} - \sum_I \frac{\hbar^2}{2M_I}\nabla_I^2 + \sum_{\substack{I,J \\ (I\neq J)}} \frac{Z_I Z_J e^2}{2|\boldsymbol{R}_I - \boldsymbol{R}_J|},\end{aligned} \tag{2.2}$$

[1]For clarity, Gaussian units is used here. Therefore the Coulomb's constant $1/(4\pi\epsilon_0)$ (in SI units, with ϵ_0 being the vacuum permittivity) in the expressions of the Coulomb potential is 1.

where $\hat{T}$ is the electronic kinetic energy, V_{ext} is electron-nucleus Coulomb attraction[2], V_{ee} is electron-electron Coulomb repulsion, $\hat{T}_N$ is the nuclear kinetic energy, V_{NN} is nucleus-nucleus Coulomb repulsion, $\{\boldsymbol{r}_i\}$ represents the positions of electrons, and $\{\boldsymbol{R}_I\}$, $\{Z_I\}$, and $\{M_I\}$ denote the positions, charge, and mass of the nuclei, respectively. The number of electrons and nuclei in real materials are in the order of N_A (Avogadro's number), making it impossible to solve Eq. 2.1 directly. So one has to resort to approximations.

One kind of approximation is to separate the motion of electrons from that of the nuclei. Because a proton is much heavier (1823 times) than an electron, when considering the motion of electrons, the kinetic energy of the nuclei can be ignored, and the electrons could be taken as following the nuclei's move immediately without changing states. This is the idea of the Born-Oppenheimer or adiabatic approximation[3], which reduces the generalized Hamiltonian into

$$\begin{aligned}\hat{\mathcal{H}} &= \hat{T} + V_{\text{ext}} + V_{\text{ee}} + V_{NN} \\ &= -\sum_i \frac{\hbar^2}{2m_e}\nabla_i^2 - \sum_{i,I} \frac{Z_I e^2}{|\boldsymbol{r}_i - \boldsymbol{R}_I|} + \sum_{\substack{i,j \\ (i\neq j)}} \frac{e^2}{2|\boldsymbol{r}_i - \boldsymbol{r}_j|} + \sum_{\substack{I,J \\ (I\neq J)}} \frac{Z_I Z_J e^2}{2|\boldsymbol{R}_I - \boldsymbol{R}_J|}.\end{aligned} \tag{2.3}$$

Once the atomic structure is known, V_{NN} can be determined analytically, and one can obtain an equation for the system of electrons

$$\hat{H}\Psi\{\boldsymbol{r}_i\} = \mathcal{E}\Psi\{\boldsymbol{r}_i\}, \tag{2.4}$$

where the Hamiltonian

$$\begin{aligned}\hat{H} &= \hat{T} + V_{\text{ext}} + V_{\text{ee}} \\ &= -\sum_i \frac{\hbar^2}{2m_e}\nabla_i^2 - \sum_{i,I} \frac{Z_I e^2}{|\boldsymbol{r}_i - \boldsymbol{R}_I|} + \sum_{\substack{i,j \\ (i\neq j)}} \frac{e^2}{2|\boldsymbol{r}_i - \boldsymbol{r}_j|},\end{aligned} \tag{2.5}$$

the wavefunction Ψ is a function of $\{\boldsymbol{r}_i\}$, while $\{\boldsymbol{R}_I\}$ are taken as constants.

In comparison with Eq. 2.1, Eq. 2.4 has been greatly simplified. However, even if periodic boundary conditions[4] are applied, which reduces the system to study to a nm-sized cell with a few tens of atoms, it is still impossible to solve Eq. 2.4 analytically, except for

[2]In general, V_{ext} can also include electric fields and Zeeman terms.

[3]Note: any motion (yes, even including the zero-point motion!) of the nuclei is neglected. The lattice vibration contribution to the ground-state energy of the system, i.e., the zero-point motion, can be calculated later by means of the force-constant matrix via the finite displacement or perturbation methods. The adiabatic approximation is a fundamental approximation in many types of problems; however, special attention has to be paid to cases with degeneracy of electronic states or metals (see, e.g., Appendix C of [31]).

[4]The periodic boundary condition is exact for crystals, which have periodic structures that are repetitive of the primitive cell. This condition is also widely used and important for simulations of other systems, such as liquids and amorphous solids. However, the shape and size of the cell in use has to be tested carefully to eliminate the "finite-size errors" arising from interactions between image atoms.

the hydrogen-atom problem. Among the methods to solve the full interacting many-body problem, DFT is the most widely used to date because of its accuracy and computational efficiency.

2.2 Density functional theory

The basis of DFT is the Hohenberg-Kohn theorems [32]: 1) any property of a system of interacting particles can be determined by the ground-state density of electrons $n_0(\boldsymbol{r})$; and 2) for any external potential $V_{\text{ext}}(\boldsymbol{r})$, a universal energy functional $E[n]$ can be defined whose global minimum value is at $n(\boldsymbol{r}) = n_0(\boldsymbol{r})$. These theorems are formally exact and general, and were soon made easily soluble in practice and very successful in materials simulations by the Kohn-Sham approach [33], which is based on the following ansatz:

- The exact ground-state density of electrons can be represented by that of an auxiliary system[5] of non-interacting particles.
- The auxiliary Hamiltonian is chosen to have the usual kinetic operator and an effective local potential $V^{\sigma}_{\text{eff}}(\boldsymbol{r})$.

This allows converting the many-electron problem (Eq. 2.4) into an independent-particle equation

$$\hat{H}^{\sigma}_{\text{KS}}\psi^{\sigma}_i(\boldsymbol{r}) = \varepsilon^{\sigma}_i\psi^{\sigma}_i(\boldsymbol{r}) \tag{2.6}$$

for the auxiliary system, where σ denotes the spin, $\hat{H}^{\sigma}_{\text{KS}} = \hat{T}_s + V^{\sigma}_{\text{eff}}(\mathbf{r})$ is the Hamiltonian, $\hat{T}_s$ is the kinetic energy, and $V^{\sigma}_{\text{eff}}(\mathbf{r})$ is the effective mean field that each particle experiences.

Comparing with the Hohenberg-Kohn energy functional

$$\begin{aligned} E_{\text{HK}} &= T[n] + E_{\text{int}}[n] + \int d\boldsymbol{r} V_{\text{ext}}(\boldsymbol{r})n(\boldsymbol{r}) + E_{II} \\ &= F_{\text{HK}}[n] + \int d\boldsymbol{r} V_{\text{ext}}(\boldsymbol{r})n(\boldsymbol{r}) + E_{II}, \end{aligned} \tag{2.7}$$

in the method of Kohn-Sham the ground-state energy

$$E_{\text{KS}} = T_s[n] + E_{\text{Hartree}}[n] + E_{\text{xc}}[n] + \int d\boldsymbol{r} V_{\text{ext}}(\boldsymbol{r})n(\boldsymbol{r}) + E_{II}, \tag{2.8}$$

where

$$n(\boldsymbol{r}) = \sum_{\sigma}\sum_{i=1}^{N^{\sigma}} |\psi^{\sigma}_i(\boldsymbol{r})|^2 \tag{2.9}$$

[5]Note that this "auxiliary system" is a theoretically conceived system for solving the real many-electron problem (Eq. 2.4). In this system, each particle can still be regarded as an electron, whose ground-state density equals that of the real system. However, the Kohn-Sham eigenvalues are not equivalent to the energies of electrons in the real system. This leads to the "band gap" problem for semiconductors and insulators. More discussions can be found in, e.g., Chapter 7 of [31].

is the electron density that satisfies $\int d\boldsymbol{r} n(\boldsymbol{r}) = N$ (total number of electrons),

$$T_s = -\frac{\hbar^2}{2m_e}\sum_{\sigma}\sum_{i=1}^{N^\sigma}\langle\psi_i^\sigma|\nabla^2|\psi_i^\sigma\rangle = -\frac{\hbar^2}{2m_e}\sum_{\sigma}\sum_{i=1}^{N^\sigma}|\nabla\psi_i^\sigma|^2 \tag{2.10}$$

is the kinetic energy,

$$E_{\text{Hartree}}[n] = \frac{1}{2}\int d\boldsymbol{r}d\boldsymbol{r}'\frac{n(\boldsymbol{r})n(\boldsymbol{r}')}{|\boldsymbol{r}-\boldsymbol{r}'|} \tag{2.11}$$

is the classical self (Coulomb)-interaction energy of the independent-particle system, and

$$\begin{aligned} E_{\text{xc}}[n] &= F_{\text{HK}}[n] - (T_s[n] + E_{\text{Hartree}}[n]) \\ &= T[n] - T_s[n] + E_{\text{int}}[n] - E_{\text{Hartree}}[n] \end{aligned} \tag{2.12}$$

is the exchange-correlation energy that includes all many-body effects. Minimizing E_{KS} with a variational approach and the Lagrange multiplier method yields the following expression for the effective potential (in Eq. 2.6)

$$\begin{aligned} V_{\text{eff}}^\sigma(\boldsymbol{r}) &= V_{\text{ext}}(\boldsymbol{r}) + \frac{\delta E_{\text{Hartree}}[n]}{\delta n(\boldsymbol{r},\sigma)} + \frac{\delta E_{\text{xc}}}{\delta n(\boldsymbol{r},\sigma)} \\ &= V_{\text{ext}}(\boldsymbol{r}) + \frac{1}{2}\int d\boldsymbol{r}'\frac{n(\boldsymbol{r}')}{|\boldsymbol{r}-\boldsymbol{r}'|} + V_{\text{xc}}^\sigma(\boldsymbol{r}). \end{aligned} \tag{2.13}$$

The Kohn-Sham approach provides a feasible way of determining the ground-state properties of many-electron systems: given $E_{\text{xc}}[n]$ (or energy density $\epsilon_{\text{xc}}([n],\boldsymbol{r})$, as in $E_{\text{xc}}[n] = \int d\boldsymbol{r} n(\boldsymbol{r})\epsilon_{\text{xc}}([n],\boldsymbol{r})$), the exact ground-state energy and electron density can be obtained by solving Eqs. 2.6 and 2.9 in a self-consistent iterative way.

Practical considerations

Exchange correlation

There have been continuing efforts exploring practical ways to approximate the exchange-correlation effects in real systems. The local density approximation (LSDA, or simply LDA) as originated from the homogeneous electron gas is often a simple starting assumption that is reasonably successful for modeling many materials..

In LDA, the exchange-correlation energy can be written as

$$E_{\text{xc}}[n] = \int d\boldsymbol{r} n(\boldsymbol{r})\epsilon_{\text{xc}}([n],\boldsymbol{r}) = \int d\boldsymbol{r} n(\boldsymbol{r})\left[\epsilon_{\text{x}}([n],\boldsymbol{r}) + \epsilon_{\text{c}}([n],\boldsymbol{r})\right], \tag{2.14}$$

where the exchange energy density (in atomic units) follows the exact expression [31]

$$\epsilon_{\text{x}}^\sigma = -\frac{3}{4}\left(\frac{6}{\pi}n^\sigma\right)^{1/3}. \tag{2.15}$$

For spin-unpolarized systems, $n^\uparrow = n^\downarrow = n/2$, therefore

$$\epsilon_{\rm x}^\uparrow = \epsilon_{\rm x}^\downarrow = \epsilon_{\rm x} = -\frac{3}{4}\left(\frac{3}{\pi}n\right)^{1/3} = -\frac{3}{4\pi}\left(\frac{9\pi}{4}\right)^{1/3}\frac{1}{r_s}, \tag{2.16}$$

where r_s characterizes the density of electrons via $1/n = 4\pi r_s^3/3$; while in partially polarized cases,

$$\epsilon_{\rm x}(n,\zeta) = \epsilon_{\rm x}(n,0) + [\epsilon_{\rm x}(n,1) - \epsilon_{\rm x}(n,0)]f_{\rm x}(\zeta), \tag{2.17}$$

where $f_{\rm x}(\zeta) = [(1+\zeta)^{4/3} + (1-\zeta)^{4/3} - 2]/[2(2^{1/3}-1)]$ is a weight factor, $\zeta = (n^\uparrow - n^\downarrow)/n$ characterizes the degree of polarization, and $n = n^\uparrow + n^\downarrow$ is the total electron density. For the correlation energy density, the widely used expression is based on parameterization [34] of accurate quantum Monte Carlo simulations of homogeneous electron gas [35]

$$\epsilon_{\rm c}(r_s) = \begin{cases} -0.0480 + 0.031\ln r_s - 0.0116 r_s + 0.0020 r_s \ln r_s & r_s < 1, \\ -0.1423/(1 + 1.0529\sqrt{r_s} + 0.3334 r_s) & r_s > 1. \end{cases} \tag{2.18}$$

The success of LDA has also stimulated ideas on improved functionals. For example, by considering the non-uniform nature of an electron distribution, several schemes of generalized gradient approximation (GGA), in which the exchange-correlation functional is a function of both the electron density n and its gradient ∇n, have been developed. There has also been active research (see Chapter 5 of [36]) on other rungs of the Jacob's Ladder, such as meta-GGA, hybrid functionals, etc., toward higher levels of chemical accuracy.

Basis sets and pseudopotential

There are different approaches for solving the Kohn-Sham equations numerically. Typically one chooses a basis set to expand the orbitals. Depending on the nature of the system, plane wave basis, Gaussian basis, and Slater-type orbital basis are frequently used. As the solutions to the single-electron equation in a constant potential, plane waves make a general basis that is easy to reach convergence, and therefore together with grid methods and fast Fourier transforms are naturally used in electronic structure studies. The other types of basis capture some atomic features for molecules, and are widely used in chemistry.

Another noteworthy concept is the pseudopotential, which together with the plane-wave method is heavily used in materials simulations. The essence of pseudopotentials is to use an effective ionic potential to replace the Coulomb potential of the nucleus and the effects of inner-shell electrons on the valence electrons. Therefore, the use of pseudopotentials can greatly simplify the calculation by reducing the size of the basis, which otherwise must be large to describe the non-smooth electronic states near the core. In studies at extremely high pressures, one usually has to use "hard pseudopotentials"[6], in order to avoid the overlapping of the core states of nearby atoms.

[6]Pseudopotentials that have small core radii.

Self-consistent iteration

Numerically solving the Kohn-Sham equation involves an initial guess of the density, and an iteration over $n^{\text{in}} \to V^{\text{in}} \to n^{\text{out}}$. In the Kohn-Sham energy functional $E_{\text{KS}} = T_s[n] + E_{\text{pot}}[n]$, the kinetic energy can be expressed as

$$\begin{aligned} T_s[n] &= E_s - \sum_\sigma \int \mathrm{d}\boldsymbol{r} V^{\sigma,\text{in}}(\boldsymbol{r}) n^{\text{out}}(\boldsymbol{r},\sigma) \\ &= \sum_\sigma \sum_{i=1}^{N^\sigma} \varepsilon_i^\sigma - \sum_\sigma \int \mathrm{d}\boldsymbol{r} V^{\sigma,\text{in}}(\boldsymbol{r}) n^{\text{out}}(\boldsymbol{r},\sigma) \\ &\approx E_s[V_{n^{\text{in}}}] - \sum_\sigma \int \mathrm{d}\boldsymbol{r} V^\sigma_{n^{\text{in}}}(\boldsymbol{r}) n^{\text{in}}(\boldsymbol{r},\sigma), \end{aligned} \tag{2.19}$$

and the potential energy

$$E_{\text{pot}}[n] = \int \mathrm{d}\boldsymbol{r} V_{\text{ext}}(\boldsymbol{r}) n(\boldsymbol{r}) + E_{\text{Hartree}}[n] + E_{II} + E_{xc}[n] \approx E_{\text{pot}}[n^{\text{in}}]. \tag{2.20}$$

These allow accurate approximation of the true Kohn-Sham energy with

$$E_{\text{KS}} \approx E_s[V_{n^{\text{in}}}] - \sum_\sigma \int \mathrm{d}\boldsymbol{r} V^\sigma_{n^{\text{in}}}(\boldsymbol{r}) n^{\text{in}}(\boldsymbol{r},\sigma) + E_{\text{pot}}[n^{\text{in}}], \tag{2.21}$$

for densities near the correct solution. Equation 2.21 is now standard at each step of the self-consistent iteration in solving Kohn-Sham equations (see Chapter 9.2 of [31]).

2.3 Finite-temperature methods

At stellar and planet interiors, high pressure is usually accompanied by high temperature, therefore entropy must also be evaluated when considering the Gibbs free energy. Low to intermediate temperatures can be taken as perturbation to the ground state (see some discussion in Section 3.1 of [31]), so lattice dynamics within the quasi-harmonic approximation (QHA) and first-principles molecular dynamics (FPMD) are the usual options. QHA works when anharmonic effects are not significant (below a few thousands Kelvin), and it fails for phases that are stable only at high temperatures; FPMD naturally accounts the anharmonicity of lattice dynamics and works at up to $\sim 10^6$ K (or 100 eV). At high temperatures, inner-shell electrons are excited, necessitating the use of small-core pseudopotentials or the all-electron model in the simulation; the computational costs also become unaffordable because of the great number of orbitals that has to be considered, which increases the dimension of the Kohn-Sham equation and lowers the computational efficiency. For calculating the equation of state of materials at even higher temperatures, such as warm dense plasmas, one has to resort to DFT methods that avoid the difficulty of orbitals, or other solutions, such as path integral Monte Carlo (PIMC).

Quasi-harmonic approximation

Lattice dynamic methods based on QHA starts from lattice vibrations $\{\omega_{\boldsymbol{q},i}\}$ (phonon spectra) that can be obtained via either a small-displacement method [37] or density-functional perturbation theory [38]. Thermodynamic properties can then be determined in the canonical ensemble, including the partition function

$$\begin{aligned} Z_{\text{vib}} &= \sum_s e^{-E_s/k_{\text{B}}T} = \sum_{\{n_{\boldsymbol{q},i}\}} e^{-\sum_{\boldsymbol{q},i}(n_{\boldsymbol{q},i}+\frac{1}{2})\hbar\omega_{\boldsymbol{q},i}/k_{\text{B}}T} \\ &= \prod_{\boldsymbol{q},i} \frac{e^{-\hbar\omega_{\boldsymbol{q},i}/2k_{\text{B}}T}}{1-e^{-\hbar\omega_{\boldsymbol{q},i}/k_{\text{B}}T}} = \prod_{\boldsymbol{q},i} \frac{1}{2\sinh\left(\hbar\omega_{\boldsymbol{q},i}/2k_{\text{B}}T\right)}, \end{aligned} \tag{2.22}$$

vibrational entropy

$$\begin{aligned} S_{\text{vib}} &= k_{\text{B}} \ln Z_{\text{vib}} \\ &= -\frac{1}{T}\sum_{\boldsymbol{q},i} \left[\hbar\omega_{\boldsymbol{q},i}/2 + k_{\text{B}}T \ln\left(1-e^{-\hbar\omega_{\boldsymbol{q},i}/k_{\text{B}}T}\right)\right] \\ &= -k_{\text{B}} \sum_{\boldsymbol{q},i} \ln\left[2\sinh\left(\hbar\omega_{\boldsymbol{q},i}/2k_{\text{B}}T\right)\right] \end{aligned} \tag{2.23}$$

Helmholtz free energy

$$\begin{aligned} F_{\text{vib}} &= U_0 - TS_{\text{vib}} \\ &= U_0 + \frac{1}{2}\sum_{\boldsymbol{q},i} \hbar\omega_{\boldsymbol{q},i} + k_{\text{B}}T \sum_{\boldsymbol{q},i} \ln\left(1-e^{-\hbar\omega_{\boldsymbol{q},i}/k_{\text{B}}T}\right), \\ &= U_0 + k_{\text{B}}T \sum_{\boldsymbol{q},i} \ln\left[2\sinh\left(\hbar\omega_{\boldsymbol{q},i}/2k_{\text{B}}T\right)\right], \end{aligned} \tag{2.24}$$

and pressure, specific heat capacity, Grüneissen parameter, etc. [39]

First-principles molecular dynamics

Pioneered by the Car-Parrinello approach [40], developments in quantum molecular dynamics based on efficient self-consistent density functional theory methods provide a practical way of simulating molecular, liquid, and solid systems at finite temperature. These FPMD methods treat the nuclei as classical particles whose motion are governed by the Newton's equation

$$M_I \ddot{\boldsymbol{R}}_I = -\frac{\partial E}{\partial \boldsymbol{R}_I} = \boldsymbol{F}_I[\{\boldsymbol{R}_J\}], \tag{2.25}$$

where E as a function of nuclei positions $\{\boldsymbol{R}_J\}$ and temperature is the electronic free energy, obtained by considering the electronic orbital occupancy with Fermi-Dirac distribution and minimizing the Mermin functional [41] in the Kohn-Sham formalism [42], $\boldsymbol{F}_I$ is the force acting on nucleus I, and M_I is the mass of this nucleus.

Path integral Monte Carlo

Based on the imaginary time path integral theory of Feynman [43], PIMC is an efficient first-principles method for simulations at finite temperatures. In PIMC, nuclei and electrons are treated as quantum paths that are cyclic in the imaginary time $0 \leq t \leq \beta = 1/k_{\mathrm{B}}T$, and all correlations effects are included. The thermal density matrix can be obtained by an integration of the path, which is weighted by the action that is a function of the path and the potential of the system [44]. In fermionic systems, the integrand can be positive or negative due to permutation and the antisymmetry of the electronic wavefunction, leading to the so-called sign problem. This problem is typically avoided by using the fixed node approximation [45], which constrains the path to be within a positive region where no sign change occurs. To this end, the free-particle nodal structure is commonly used, with which the results are exact in the limit of high temperature [46]. It has been demonstrated to work well down to ∼1 million Kelvin for a series of systems including C, H_2O, N, O, and Ne [47, 48, 49, 50]. Recent developments have also implemented a localized nodal surface and successfully obtained the equation of state of silicon [51]. In Chapter 5 of this dissertation we perform the first PIMC simulation of warm dense sodium.

2.4 Discussion

With the great advances in computer technology in the past decade there have been many efforts in the development and application of advanced first-principles methods in the study of Earth and planetary materials. Examples include diffusion Monte Carlo [52, 53] for benchmarking DFT results on energy relations between phases, dynamic mean field theory [54] for electrical conductivity calculations, determination of Gibbs free energy using thermodynamic integration [55, 56, 57, 58, 11] or exploration of free-energy surfaces assisted by order parameters [59], structure searching techniques for exploring unknown high-pressure phases [60, 61, 62, 63], etc. These have greatly contributed to the improved knowledge of chemistry and physics of materials under extreme conditions, and composition and dynamics of the interiors of the Earth and other planets.

Chapter 3

Thermoelasticity of Iron- and Aluminum-bearing $MgSiO_3$ in the Earth's Lower-mantle Conditions

The Earth has music for those who listen.

3.1 Introduction

Fe-bearing perovskite (Pv, a.k.a. bridgmanite) and post-perovskite (pPv) are the most abundant minerals in the Earth's lower mantle. A good knowledge of their elastic properties under relevant high-pressure (P) and temperature (T) conditions is of fundamental importance for understanding the structure and dynamics of the Earth's interior. Experiments have suggested that Pv hosts ∼10 mol.% iron and a slightly lower amount of Al in the pyrolitic model composition (Table 3.1), expected from the top to, at least, the mid-lower mantle [64]. It has also been known that the amount of Fe in different ionic states can be controlled by oxidation, charge disproportionation and the existence of Al [65]. Despite this, it is still debated how much iron remains in Pv, how it is distributed between Pv and pPv, and whether Fe^{2+} disproportionates to form Fe^{3+} + Fe^0 metal, or partitions into magnesiowstite or melt, in the lowermost mantle (e.g., [66, 64]). Currently, there is scarce experimental data available on the elastic properties of these systems [67], and the uncertainty could be high (e.g., 3% for shear velocity of $MgSiO_3$ perovskite at 2700 K, according to Figure 7 of [68]), due to the interplay between the above factors and technical issues relating to the extreme conditions. This necessitates theoretical methods, which are not limited by the same constraints as experiments and have been proven to be a powerful tool in determining the elastic properties of minerals at lower mantle conditions.

There have been several reports on the elastic properties of these Pv and pPv systems using first-principle calculations. However, these have mainly focused on pure $MgSiO_3$ for high-T conditions [71, 72, 73, 74, 75, 68], or Fe/Al-bearing systems at 0 K [76, 77, 78, 79,

Table 3.1: Major cation contents and key parameters in an average pyrolite from Table 5-2, column 8 of [69]. The numbers in parenthesis denote the error of the corresponding values. Data adapted from Table 1, column 3 of [70].

Element	Amount per 12 O
Mg	4.094 (0.235)
Si	3.251 (0.084)
Fe	0.474 (0.101)
Al	0.391 (0.073)
Ca	0.239 (0.065)
Parameter	Value
Mg#=Mg/(Mg+Fe)	0.90 (0.05)
Mg/Si	1.27 (0.06)

80, 81], because of the high computational cost and the complex structural and electronic properties of Fe/Al-bearing systems at high P and T.

Examples on this complexity include the pressure-induced high-spin (HS) to low-spin (LS) transition in iron [82] and challenges arising from the large number of mechanisms that iron can enter the Pv and pPv structures. Ferrous iron (Fe^{2+}) substitutes for Mg in the pseudo-dodecahedral A (Mg) site, but for ferric iron (Fe^{3+}) charge balance requires the coupled substitution of Fe-Al or Fe-Fe pairs [83], with one cation in the A site and the other in the octahedral B (Si) site. Incorporation of ferric iron via the oxygen vacancy mechanism is not expected in Pv and pPv at lower mantle conditions [84].

Ferrous iron, in the A site, is expected to remain in the HS state, in Pv and pPv, at all mantle conditions [85, 86]. In contrast, ferric iron undergoes a spin transition at lower-mantle pressures, as the crystal field splitting surpasses the spin pairing energy, which breaks Hund's rules that predict all five d electrons in Fe^{3+} have the same spin (HS state) and stabilizes the LS state (3 electrons spin up, 2 down). The spin transition of ferric iron is expected to start at about 75 GPa for the A site, and at much lower pressures for the B site [87, 88, 89, 90].

In recent years, there have been several studies on the effects of ferrous and ferric iron on the thermoelastic properties of Pv and pPv [91, 92, 93]. To date, agreement with seismological models of the lower mantle has not been reached. One potential reason is that the influence of Al^{3+} has not yet been included, and another could be related to the possible inadequacy of using the quasi-harmonic approximation (QHA) in computing thermoelasticity at high-P and T. There has been one study that used density functional molecular dynamics (DFT-MD) to calculate the properties of Pv and pPv enriched with ferrous iron [94], but this only reported values at one pressure.

We apply DFT-MD to determine the elastic properties of ferrous and ferric iron-bearing Pv and pPv over a wide range of pressure and temperature conditions relevant to the Earth's lower mantle. In the case of ferric iron, Fe-Al and Fe-Fe substitution are considered. DFT-

MD naturally accounts for the anharmonicity of lattice dynamics, which is important for describing the elastic behavior of minerals at high T (above the Debye temperature) and has been used in several previous studies [74, 68]. In the case of ferrous iron only the HS state is considered, whereas for ferric iron different Fe-Fe or Fe-Al compositions in various possible spin states are considered. The atomic structures can be found in the supplementary material of [95]. We obtain lattice parameters at finite temperatures by performing DFT-MD simulations at constant pressures (NPT ensemble), which is followed by fixed-cell (NVT) calculations on strained structures to calculate the elastic coefficients and other elastic properties. Based on these calculations, we derive the seismic properties of a mineral assemblage to compare with a 1D seismological model, with the aim of constraining the mineral composition of the lower mantle. We further exemplify shear wave anisotropic properties resulting from deformation within a deep subducting slab and discuss the implications for seismic observations of shear wave anisotropy.

3.2 Theory

Computational methods

Our calculations are performed using the Vienna ab initio simulation package (VASP) [96]. Projector augmented wave (PAW) pseudopotentials [97] and the local density approximation (LDA)-based [35] exchange-correlation functional are used. It has been shown that in some cases, standard DFT functionals can fail to predict the correct electronic properties of iron-bearing minerals, and inclusion of a Hubbard U term leads to improved predictions of their electronic, structural and elastic properties [98]. However, a recent study suggests that provided standard DFT functionals produce the correct insulating ground states and correct orbital occupancy, the electron density is also correct, therefore the structural and elastic properties predicted with them should be similar to those with a U term [85]. We confirmed this conclusion by comparing the results of calculations with and without a U term, for a select number of iron-bearing Pv structures (Table 3.9), and performed the remainder without a U term.

The supercell sizes 2×2×1 (80-atom) for Pv, and 3×1×1 (60-atom) or 4×1×1 (80-atom) for pPv are used. We employ pseudopotentials with core radii equaling 2.2, 1.9, 2.0, 1.9, and 1.52 Bohr for Fe, Al, Mg, Si, and O, respectively. In static calculations, the plane wave energy cutoff is set to 800 eV, and Monkhorst-Pack k-mesh [99] of 2×2×4 (for Pv supercell) or 6×6×6 (for pPv supercell) are chosen for Brillouin zone sampling. The enthalpy is evaluated based on structures that are all relaxed until all forces are smaller than 10^{-4} eV/Å. In MD simulations, we follow previous studies [75, 68] and use time step of 1 fs, energy cutoff of 500 eV and only the Γ point to sample the Brillouin zone. Tests show that using these settings the elastic properties are converged to within statistical error. We use the Nosé thermostat to control the temperature [100]. The lattice constants are obtained by averaging over NPT trajectories. These are then used in the NVT simulations. For calculating the elastic

constants from linear stress-strain relations, three axial and one triclinic strain are applied to the cell. During NPT simulations, we fix the cell to be orthorhombic to avoid unnecessary fluctuations. The same averaging scheme is applied to NVT trajectories to retrieve stress components and energies. The NPT and NVT trajectories are typically over 3 ps and 5 ps, respectively. The convergence is shown in Fig. 3.10.

For ferrous iron we include four Fe^{2+} in 80-atom unit cells of Pv and pPv to construct $(Mg_{1-x}Fe_x)SiO_3$ structures with an atomic percent x equal to 25%. For ferric iron we include one or two Fe^{3+}-M^{3+} (M representing Fe or Al) pairs in $MgSiO_3$ by charge-coupled substitution Fe_{Mg}+M_{Si} in order to construct $(Mg_{1-x}Fe_x)(Si_{1-x}M_x)O_3$ structures with atomic percent x equal to 6.25% or 12.5% for Pv, and 8.33% or 16.7% for pPv. Such iron or aluminum compositions are relevant to the lower mantle [64]. For Fe^{2+} in these models, we consider only the HS (spin momentum $\mathcal{S}$=4/2) ferromagnetic state, whereas for Fe^{3+} we consider both the HS ($\mathcal{S}$=5/2) and LS ($\mathcal{S}$=1/2) states. Intermediate-spin states are not considered because they have been found to be energetically disfavored in previous studies [89]. For systems with multiple ferric iron cations, we take into account all possible spin configurations, including pure HS, pure LS, or HS-LS mixtures in the ferromagnetic (FM) or antiferromagnetic (AFM) states. Our results confirm conclusions reached in several previous DFT calculations on the site-dependence and values of the transition pressure, i.e., Fe^{3+} has higher transition pressure in the A-site than the B-site. This enables us to disregard unlikely configurations, for example, B-site Fe^{3+} in HS at 100 GPa. In spite of this, there are still an ample number of configurations to consider.

For ferric iron-bearing structures, we first perform a structural relaxation at 0 K by fixing the spin state of each iron in the system. For the different compositions, we compare the enthalpies of the different spin states at each pressure, in order to determine the most stable configurations. The magnetic entropy is the same for Fe^{3+} in either A or B sites whether it is HS or LS[1]. If we assume the vibrational entropy of the different spin configurations to be similar[2], then the enthalpies provide a good approximation for the most stable spin states at high temperature without having to calculate the Gibbs free energy. We limit our studies of high-temperature elasticity mainly to the most stable configurations at 0 K. In spite of this,

[1]The Gibbs free energy of a system with fixed configuration consists of an enthalpy term H and an entropy term TS, where S is a sum of vibrational and magnetic contribution. For each iron, the magnetic entropy $S_{\rm mag} = k_{\rm B}\ln[m(2\mathcal{S}+1)]$, where m is the degeneracy and $\mathcal{S}$ is the spin momentum number. For ferric iron, $\mathcal{S}(\rm HS) = 5/2$ and $\mathcal{S}(\rm LS) = 1/2$; the orbit degeneracy $m(\rm HS) = 1$ and $m(\rm LS) = 3$, regardless of A (dodecahedral) or B (octahedral) site. Therefore, the magnetic entropy $S_{\rm mag}(\rm HS) = k_{\rm B}\ln[1\times(2\times5/2+1)] = k_{\rm B}\ln 6$; $S_{\rm mag}(\rm LS) = k_{\rm B}\ln[3\times(2\times1/2+1)] = k_{\rm B}\ln 6$, i.e., in both A- and B-sites of the Pv and pPv structures, $S_{\rm mag} = k_{\rm B}\ln 6$ regardless of HS or LS. Therefore, we don't consider the difference in magnetic entropy between different magnetic configurations.

[2]It is shown in Fig. 2 of [101] for $(Fe,Mg)SiO_3$ bridgmanite that the vibration-mode differences between Fe^{2+} in HS and LS decrease with Mg content. Almost reconciling vibrational density of states between HS and LS states of Fe^{3+} in B sites of $(Mg,Fe)(Si,Fe)O_3$ bridgmanite can also be observed in Fig. 4 of [102]. A similar approximation has also been made in [81] for (Fe,Mg)O ferropericlase. Therefore, it is reasonable to assume the vibrational entropy of Pv or pPv systems with Fe^{3+} in different spin configurations are the same, at low iron concentrations ($x < 17\%$) considered in this study. However, this should be examined more carefully in future research.

because there does not exist a perfect way of describing the correlation effects of $3d$ electrons of iron, and temperature could potentially stabilize the HS state, at high temperature we selectively carry out additional calculations on configurations other than the most stable ones at 0 K, in order to get a more complete picture of the effect of different magnetic states on the elastic properties.

Calculation of elastic, seismic, and thermodynamic properties

The elastic constants are determined assuming the linear stress-strain relation $\sigma_\alpha = C_{\alpha\beta}\epsilon_\beta$, although higher-order terms become more significant for larger strains. In our calculations, we choose an optimized strain of magnitude $\epsilon = \pm 0.5\%$ [103]. The orthorhombic symmetry of Pv and pPv requires us to obtain the nine independent elastic constants by applying three axial strains and one triclinic strain [75]. The polycrystalline bulk and shear moduli, K and G, are determined consequently using the Voigt averaging scheme. A comparison with the Voigt-Reuss-Hill (VRH) scheme is shown in Appendix Table 3.10.

The direction-dependence of the phase velocities is governed by the Christoffel equation

$$[\rho v^2 \delta_{ik} - C_{ijkl} n_j n_l][u_k] = 0, \tag{3.1}$$

where C_{ijkl} is the elastic tensor where the indexes ij and kl correspond to the above α and β via the Voigt notation: 11; 22; 33; 23; 13; 12→1; 2; 3; 4; 5; 6, δ_{ik} is the Kronecker delta and n_j denotes the wave propagation direction. The solution to the Christoffel equation yields three eigenvalues that are the phase velocities of the three wave modes, P, SV and SH, that can exist in an anisotropic solid. Because of the high velocity, the transmission of seismic waves in the lower mantle is primarily an adiabatic process rather than an isothermal one. Therefore, we add an adiabatic correction according to [104]

$$C^S_{\alpha\beta} = C^T_{\alpha\beta} + \frac{TV}{C_\eta} b_\alpha b_\beta, \tag{3.2}$$

where $b_\alpha = (\partial\sigma_\alpha/\partial T)_\eta$, C_η is fixed-configuration heat capacity approximated by $C_V = (\partial E/\partial T)_V$, which can be obtained by two additional simulations for each structure with fixed volume and temperatures changed by ±100 K.

In order to compare the results with experimental data, one has to apply a pressure correction, because of the well-known fact that LDA underestimates lattice constants and thus the pressure. One simple way is to calculate at experimentally determined ambient-pressure volume in the static condition, and then apply the pressure difference as a constant shift [71] ΔP to all computed pressures regardless of P, T, Fe/Al compositions and the mineral phases. It is worthwhile to note that this is by no means a perfect solution, but works reasonably well [75, 103, 68]. With a careful estimation on the ambient-pressure volume in the static condition (see the Appendix Section 3.6), we determined $\Delta P = 4.0 \pm 0.8$ GPa.

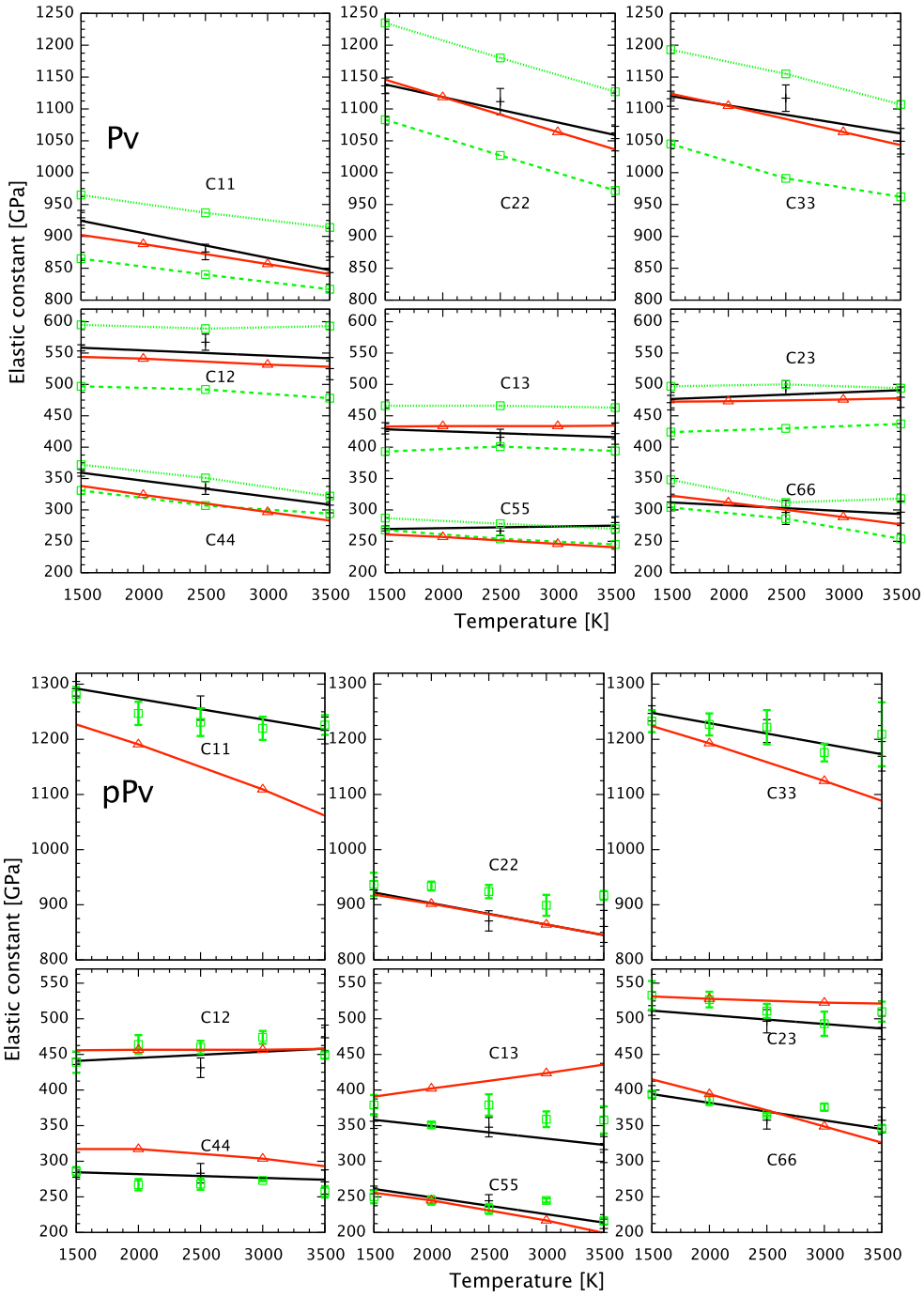

Figure 3.1: The elastic constants of $MgSiO_3$ Pv (top) and pPv (bottom) at 129 GPa as functions of temperature. Our data are represented with points and fitted with lines in black. Previously DFT-MD studies by [68] on Pv at 108 GPa and 137 GPa, shown in green dashed and dotted line squares respectively, and [75] on pPv at 125 GPa, shown in green squares, and QHA study by [73] on Pv and pPv at 125 GPa, shown in red line triangles, are displayed for comparison.

Table 3.2: The stable spin configurations, denoted by the spin state of Fe^{3+} in the A site (or A site - B site), of Fe^{3+}-Fe^{3+} and Fe^{3+}-Al^{3+} bearing Pv and pPv at T=0 K and different pressures. No pressure correction is applied.

P[GPa]	Iron spin state			
	$(Mg_{1-x}Fe_x)(Si_{1-x}Fe_x)O_3$		$(Mg_{1-x}Fe_x)(Si_{1-x}Al_x)O_3$	
Pv	x=6.25%	x=12.5%	x=6.25%	x=12.5%
25	HS-LS, fm	HS-LS, fm	HS	[a]HS-HS, afm
50	LS-LS, afm	HS-LS, fm	HS	[a]HS-HS, afm
75	LS-LS, afm	LS-LS, afm	LS	[b]HS-LS, fm
100	LS-LS, afm	LS-LS, afm	LS	[b]LS-LS, afm
125	LS-LS, afm	LS-LS, afm	LS	[b]LS-LS, afm
pPv	x=8.3%	x=16.7 %	x=8.3%	x=16.7%
100	LS-LS, fm	LS-LS, fm	LS	[b]HS-LS, fm
125	LS-LS, fm	LS-LS, fm	LS	[b]HS-LS, fm
150	LS-LS, fm	LS-LS, fm	LS	[b]HS-LS, fm

[a] two Fe-Al pairs, spin configuration denoted by Fe^{3+} at pair1-pair2

[b] one Fe-Fe and one Al-Al pair

3.3 Results and discussion

Phase relations

The most stable spin configurations at 0 K for the ferric iron systems are summarized in Table 3.2. In $(Mg_{1-x}Fe_x)(Si_{1-x}Fe_x)O_3$ Pv, Fe^{3+} in the A-site undergoes a spin transition below 50 GPa; with Al^{3+} in the B-site, the transition pressure $P_{\rm tr}$ increases to over 50 GPa. In both cases $P_{\rm tr}$ of A-site Fe^{3+} increases with x. B-site Fe^{3+} is always LS. The dependence of $P_{\rm tr}$ on x reflects the importance of the Fe-M (M=Fe or Al) interactions. In pPv, Fe^{3+} in the A-site is always LS above 100 GPa, except for $(Mg_{1-x}Fe_x)(Si_{1-x}Al_x)$ with x=17%, where two pairs of A-B sites are occupied by one Fe^{3+}-Fe^{3+} and one Al^{3+}-Al^{3+} pair, where the Fe^{3+} in the A-site is always HS. B-site Fe^{3+} is always LS, as found for Pv.

Comparing with previous studies [86, 87, 88, 89, 90, 105, 106, 107], the transition pressures found here are generally lower. This can be understood from the following aspects: 1) LDA typically underestimate the lattice constants and thus the pressure; 2) on-site Coulomb repulsion (Hubbard U) increases the transition pressure for both A and B sites; 3) the configurations (structures files can be found in the supplementary material of [95]) may vary in different calculations; 4) the distortions of crystallographic sites are different between one-site and two-site substitution by Fe^{3+} or Al^{3+}.

We also note that predicting spin states is complicated and involves many issues that are not understood. For example, it is debated whether Fe^{3+} can occupy both A- and B-sites or

Table 3.3: Comparison on density, adiabatic bulk modulus K^S, shear modulus G, and bulk, shear, and compressional velocities V_ϕ, V_s, and V_p at different spin states. The notation for spin states is the same as in Table 3.2. Numbers in parenthesis denote the error of the corresponding values.

	ρ[kg/m^3]	K^S[GPa]	G[GPa]	V$_\phi$[km/s]	V$_s$[km/s]	V$_p$[km/s]
Pv, $(Mg_{1-x}Fe_x)(Si_{1-x}Fe_x)O_3$	x=12.5%, 75 GPa, 1500 K					
HS-LS	5279	513.22(3.82)	225.13(2.76)	9.86(0.04)	6.53(0.04)	12.41(0.04)
LS-LS	5301	514.38(8.23)	228.55(5.24)	9.85(0.08)	6.57(0.08)	12.43(0.08)
Pv, $(Mg_{1-x}Fe_x)(Si_{1-x}Al_x)O_3$	x=12.5%, 125 GPa, 1500 K					
[a]HS-HS	5607	674.69(4.46)	294.55(3.78)	10.97(0.04)	7.25(0.05)	13.80(0.04)
[b]LS-LS	5614	681.87(4.25)	294.10(3.48)	11.02(0.03)	7.24(0.04)	13.83(0.04)
pPv, $(Mg_{1-x}Fe_x)(Si_{1-x}Fe_x)O_3$	x=8.33%, 100 GPa, 1500 K					
HS-LS	5512	600.21(4.40)	293.77(3.76)	10.43(0.04)	7.30(0.05)	13.41(0.05)
LS-LS	5519	587.15(5.60)	299.88(6.07)	10.31(0.05)	7.37(0.07)	13.37(0.07)
pPv, $(Mg_{1-x}Fe_x)(Si_{1-x}Fe_x)O_3$	x=16.67%, 150 GPa, 2500 K					
[b]HS-HS	5879	745.25(8.77)	335.59(7.93)	11.26(0.07)	7.56(0.09)	14.24(0.08)
[b]HS-LS	5881	758.91(7.62)	340.14(7.53)	11.36(0.06)	7.61(0.08)	14.36(0.07)
[b]LS-LS	5889	761.04(8.07)	336.40(8.56)	11.37(0.06)	7.56(0.10)	14.33(0.08)

[a] two Fe-Al pairs, spin configuration denoted by Fe^{3+} at pair1-pair2
[b] one Fe-Fe and one Al-Al pair

exclusively the A-site, and if there is exchange from the A- to the B-site. However, because spin state has only a minor effect on elastic properties ([80, 88] and Table 3.3), this will have little influence on our calculated seismic properties. For example, for all compositions tested (Table 3.3), the difference between the seismic properties of the high- and low-spin states is on average 0.5%, with a maximum of 1%.

By comparing enthalpies, we determine the Pv→pPv transition pressure (Table 3.3). For pure $MgSiO_3$, our finding is in agreement with previous DFT-LDA calculations (83.7-100 GPa, according to [108] and [109]) as well as experiments (91-116 GPa, extrapolated to T=0 K based on Fig. 4 in [110]). The transition pressure decreases with Fe^{2+} or Fe^{3+}-Fe^{3+} content (less so in the former case), while it slightly increases and then decreases with the amount of Fe^{3+}-Al^{3+}. This implies that the existence of Al^{3+} increases the Fe^{3+}-bearing Pv→pPv transition pressure, which is consistent with the previously assumed role of Al^{3+} in $MgSiO_3$ [83].

Table 3.4: The Pv→pPv phase transition pressure at $T = 0$ K for pure and Fe^{2+}, Fe^{3+}-Fe^{3+} or Fe^{3+}-Al^{3+} bearing $MgSiO_3$. The LDA pressure correction ΔP= 4.0 has been applied.

$MgSiO_3$	$(Mg_{0.75}Fe_{0.25})SiO_3$	$(Mg_{1-x}Fe_x)(Si_{1-x}Fe_x)O_3$		$(Mg_{1-x}Fe_x)(Si_{1-x}Al_x)O_3$	
		x=8%	x=12.5%	x=8%	x=12.5%
94.9	78.8	84.6	71.0	97.2	87.4

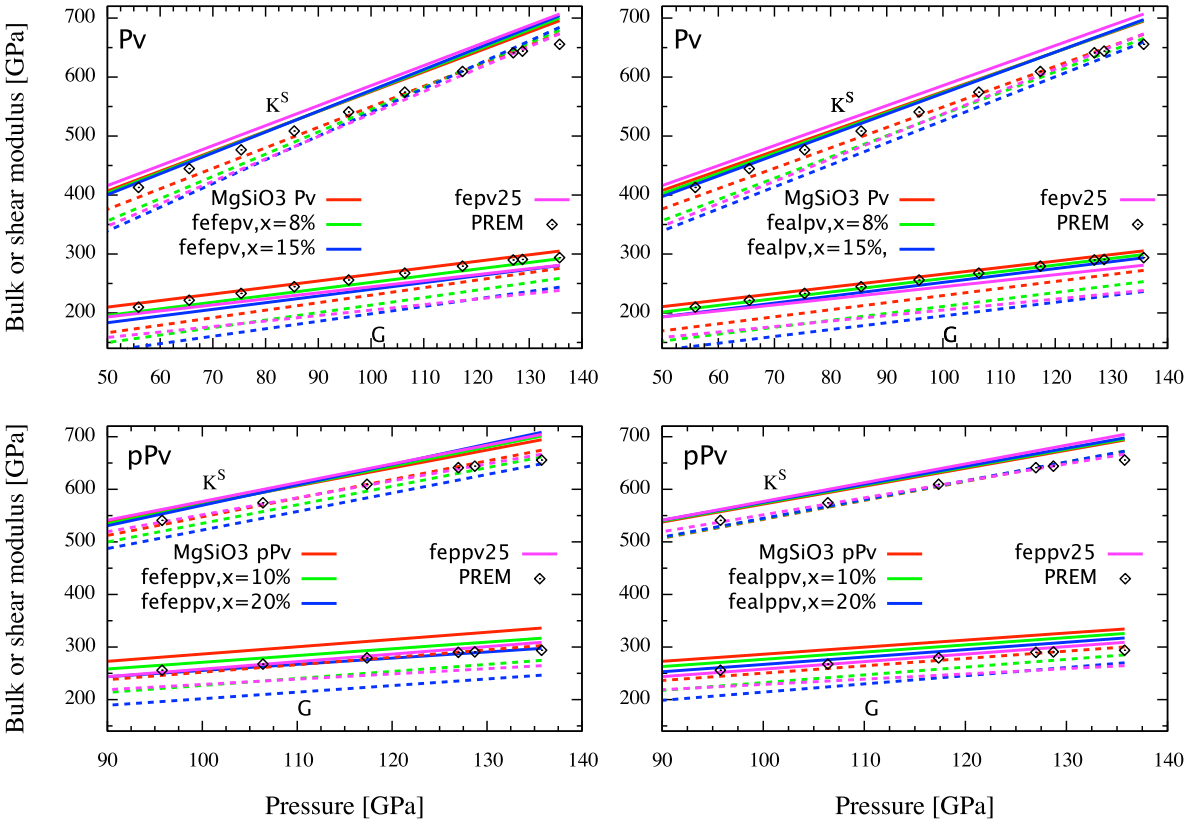

Figure 3.2: Bulk and shear moduli (K^S and G) of pure and Fe^{3+}- Fe^{3+} (fefe, left) or Fe^{3+}-Al^{3+} (feal, right) bearing $MgSiO_3$ Pv and pPv at 2000 K (solid lines) and 4000 K (dashed lines), in comparison with that of $Mg_{0.75}Fe_{0.25}SiO_3$ (fepv25 and feppv25) and PREM as functions of pressure. Red, green, and blue lines correspond to x=0, 8%, and 15% for Pv and 0, 10%, and 20% for pPv, respectively. In each panel, the top lines correspond to K^S, the lower ones correspond to G.

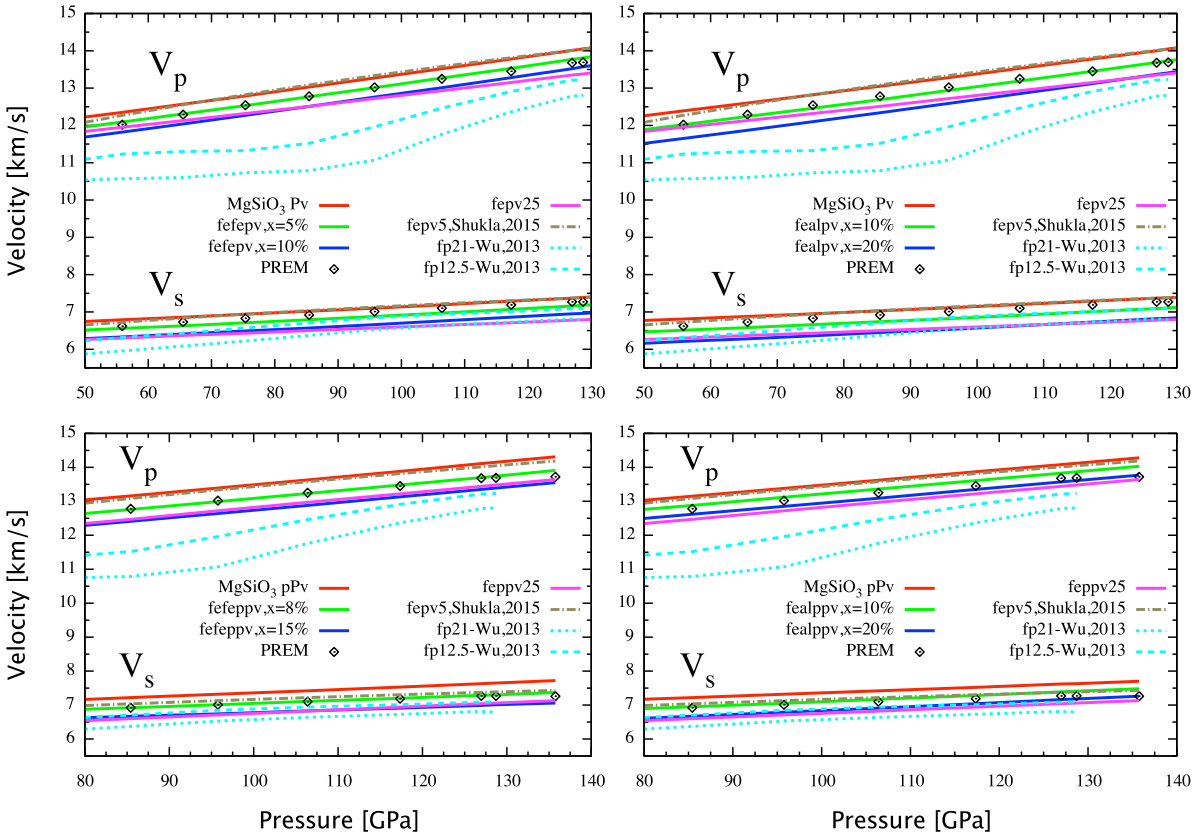

Figure 3.3: The sound velocities of pure and Fe^{3+}- Fe^{3+} (fefe, left) or Fe^{3+}-Al^{3+} (feal, right) bearing $MgSiO_3$ in the Pv (top) and pPv (bottom) phases in comparison with that of $Mg_{0.75}Fe_{0.25}SiO_3$ (fepv25 and feppv25), $Mg_{0.95}Fe_{0.05}SiO_3$ (fepv5, from [93]), ferropericlase (fp21 and fp12.5, from [111]), and the PREM along the geotherm by [112].

Temperature and pressure dependence of elastic properties

We first compare the elastic constants C_{ij} of $MgSiO_3$ Pv and pPv from this work with previous calculations (Fig. 3.1). Our results reconfirm the overall consistency between DFT-MD and QHA and the disagreement at high temperatures, especially for C_{11}, C_{13}, and C_{33} in pPv, as was noted previously [75]. More benchmarking comparisons, as well as complete lists on the elastic and seismic properties are given in the Appendix Section 3.6.

In order to quantify the effect of T, P, and x on elastic properties, we use the following equation to fit the computed elastic constants and the sound velocities

$$Q(T,P,x) = A_0(x)TP + A_1(x)T + A_2(x)P + A_3(x), \tag{3.3}$$

where Q is the property being fit, and each parameters $A_i(x)$ is linearly fit to x by $k_i x + b_i$.

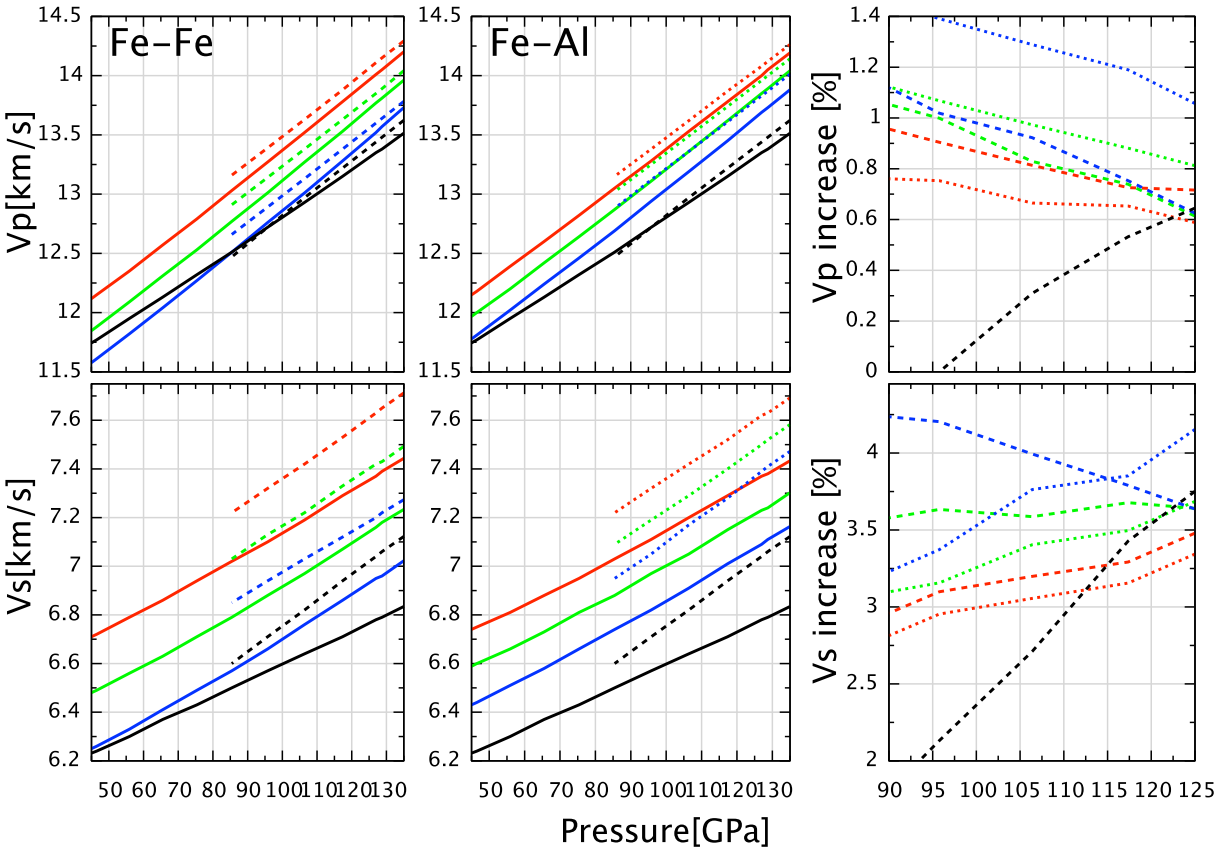

Figure 3.4: The sound velocities of Fe^{3+}- Fe^{3+} (Fe-Fe, left) or Fe^{3+}-Al^{3+} (Fe-Al, center) bearing $MgSiO_3$ Pv (solid curves) and pPv (dashed or dotted curves) with x=0.0 (red), x=5% (green) and x=10% (blue). The corresponding velocities increases from Pv to pPv phases are shown in the right panel. Corresponding results for $Mg_{0.75}Fe_{0.25}SiO_3$ are also plotted (black curves) for comparison.

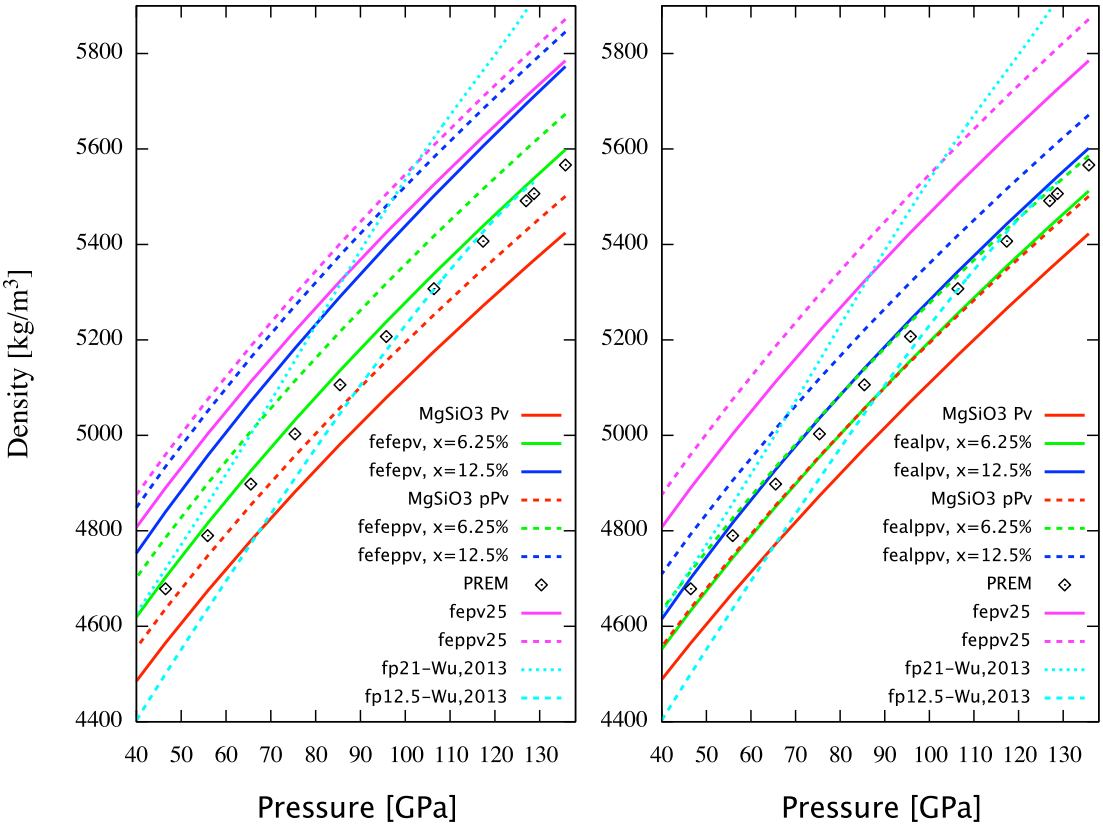

Figure 3.5: The density profile of pure and Fe^{3+}- Fe^{3+} (fefe, left) or Fe^{3+}-Al^{3+} (feal, right) bearing $MgSiO_3$ in the Pv and pPv phases, in comparison with that of $Mg_{0.75}Fe_{0.25}SiO_3$ (fepv25 and feppv25), ferropericlase (fp21 or fp12.5, from [111]) and PREM along the geotherm [112].

Data for Pv at 25 GPa are not included to improve the quality of the fitting. Complete lists of the fit parameters can be found in Table 3.12 in the Appendix.

Our results show that the elastic constants increase with pressure and mostly decrease with temperature, on the order of 1 for dC_{ij}/dP compared to about 10^{-2} GPa/K for dC_{ij}/dT. C_{12}, C_{13}, and C_{66} remain approximately constant when Fe or Al contents increases in Pv, while the other six values decrease. In contrast, for pPv, C_{22}, C_{12} and C_{13} increase with the Fe or Al contents. The effect of Fe is akin to that of Al and is usually accompanied by slightly higher C_{ij} for Pv but lower C_{ij} for pPv. The magnitude of the compositional derivatives depends on the specific P, T condition.

Analysis of the adiabatic bulk and shear moduli (K^S and G) as a function of P and T, using elastic constants fitted by Eq. 3.3, shows that G uniformly decreases with x for both

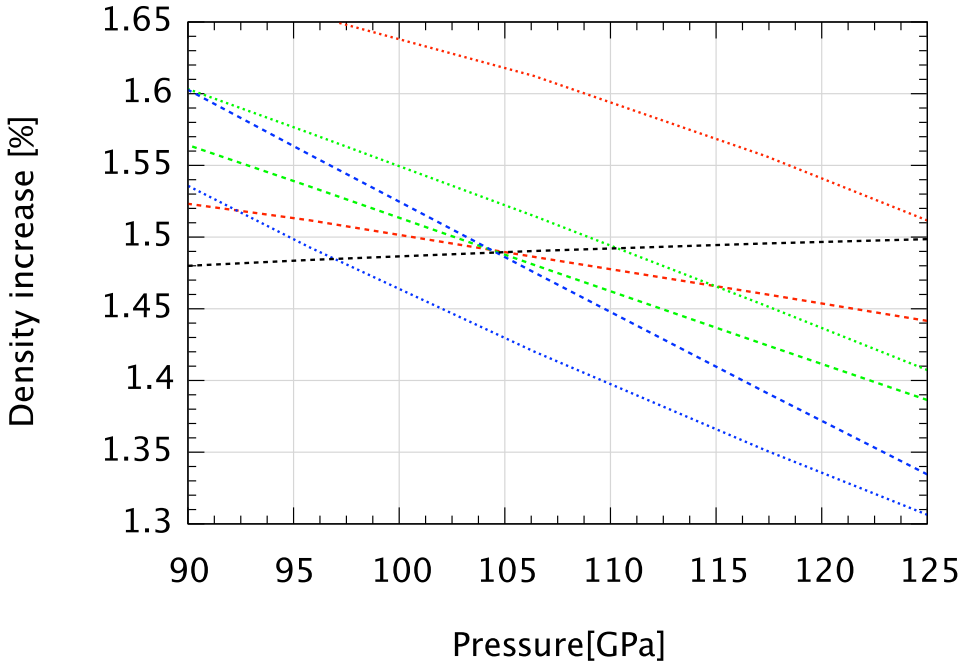

Figure 3.6: The density increase from Pv to pPv phases for Fe^{3+}- Fe^{3+} (dashed curves) or Fe^{3+}-Al^{3+} (dotted curves) bearing $MgSiO_3$ with x=0.0 (red), x=6.25% (green) and x=12.5% (blue). Corresponding results for $Mg_{0.75}Fe_{0.25}SiO_3$ are also plotted (dash black) for comparison.

Pv and pPv, but K^S does not follow the same trend (Fig. 3.2). The pressure derivatives of the moduli and C_{ij} are generally less dependent on x at lower T, especially for Pv. The trend for ferrous iron is relatively simple—both moduli decrease with temperature, and the pressure derivatives are relatively more stable than the ferric iron bearing systems. This is understandable considering its more simple substitution mechanism and spin state, and fewer data at varied P and T.

Temperature, pressure, and composition dependence of sound velocities and density

The compressional (V_p) and shear (V_s) wave velocities are fitted as functions of P, T and x using Eq. 3.3. The parameters are summarized in Table 3.5. In this way we can study how the velocities depend on the Fe or Al content x. As is shown in Figs. 3.3-3.4, the sound velocities steadily decrease with Fe or Al content, while the effect of Fe is larger, for both Pv and pPv. The pPv phase has higher velocities than Pv. At 110 GPa, the differences in V_p and V_s are 0.7% and 3.2%, respectively; the values further increase to 0.95% and 3.5% when x=5%, and to 1.25% and 3.8% when x=10%, for $MgSiO_3$ with Fe^{3+}-Al^{3+} pairs; with

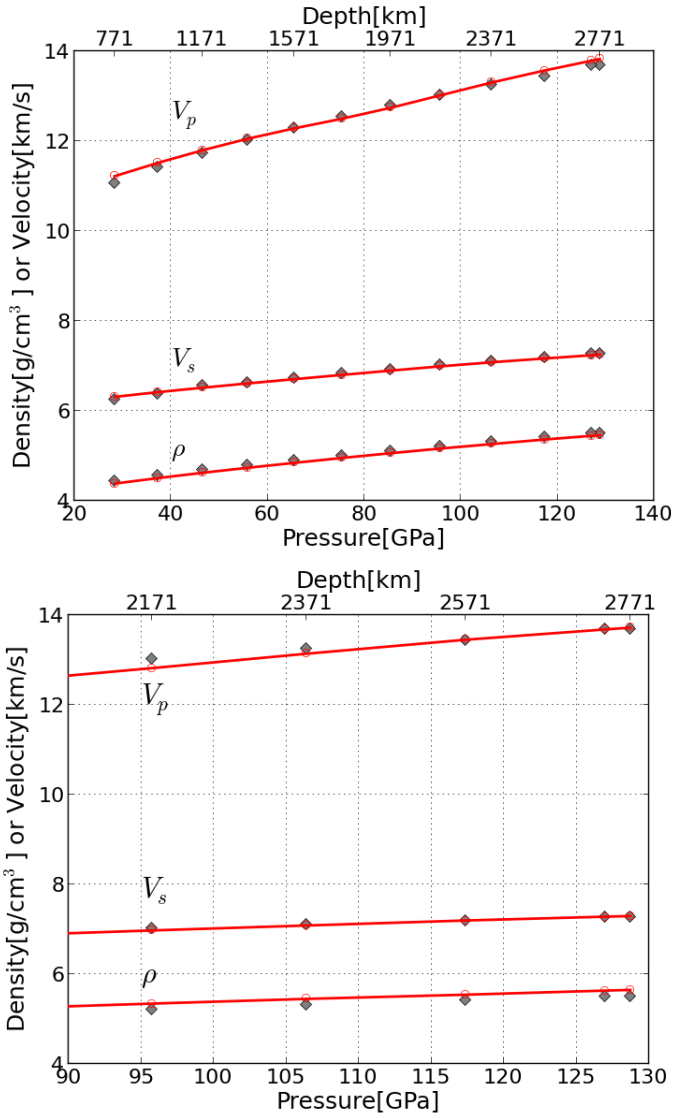

Figure 3.7: Comparing density and velocities of mineral assemblages with that of PREM (black diamond points) assuming the geotherm by [112]. Left, the assemblage consists of 34 vol.% $Mg_{0.95}Fe_{0.05}SiO_3$, 10 vol.% $Mg_{0.95}Fe_{0.05}Si_{0.95}Fe_{0.05}O_3$, and 43 vol.% $Mg_{0.94}Fe_{0.06}Si_{0.94}Al_{0.06}O_3$ in the Pv phase and 13 vol.% $Fe_{0.125}Mg_{0.875}O$; right: it consists of 26 vol.% $Mg_{0.95}Fe_{0.05}SiO_3$, 10 vol.% $Mg_{0.9}Fe_{0.1}Si_{0.9}Fe_{0.1}O_3$, and 53 vol.% $Mg_{0.85}Fe_{0.15}Si_{0.85}Al_{0.15}O_3$ in the pPv phase and 11 vol.% $Fe_{0.21}Mg_{0.79}O$. $Mg_{0.95}Fe_{0.05}SiO_3$ data are estimated with the BurnMan code [113] by applying the thermodynamic model of [114] on the calculation by [93]. For the pPv phase of $Mg_{0.95}Fe_{0.05}SiO_3$, K^S is estimated to be the same as that of the Pv phase, G and ρ are estimated to be 5% and 1.5% larger than that of the Pv phase, respectively. Ferropericlase data are from [111].

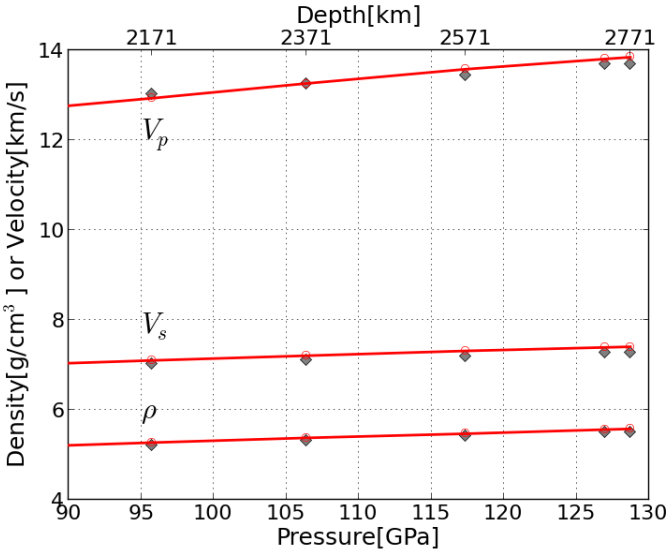

Figure 3.8: The velocities and density of an assemblage consisting of 34 vol.% $Mg_{0.95}Fe_{0.05}SiO_3$, 10 vol.% $Mg_{0.95}Fe_{0.05}Si_{0.95}Fe_{0.05}O_3$, and 43 vol.% $Mg_{0.94}Fe_{0.06}Si_{0.94}Al_{0.06}O_3$ in the pPv phase and 13 vol.% $Fe_{0.21}Mg_{0.79}O$ in comparison with that of PREM (black diamond points) assuming the geotherm by [112]. $Mg_{0.95}Fe_{0.05}SiO_3$ and ferropericlase data are obtained in the same way as that in Fig. 3.7.

Fe^{3+}-Fe^{3+} pairs, the change in V_p is insensitive to x, but the change in V_s is larger than that corresponding to Fe^{3+}-Al^{3+} pairs by ~0.2%. The replacement of 25% Mg by ferrous iron significantly lowers the sound velocities. At 110 GPa, the velocities of the pPv phase becomes higher than that of the Pv phase by 0.4% and 3.0% for V_p and V_s, respectively.

We investigate the relation between density and P, T and x by starting from the Vinet equation of state (EOS). The EOS has three ambient parameters, ρ_0, K_0, and K_0', and is an isothermal equation that has been widely used for minerals at Earth-interior conditions. Here, we assume linear dependence of ρ_0 and K_0, and independence of K_0', on T, and fit P as a function of ρ and T for each iron or aluminum content x. Finally, we fit the density at each P, T condition linearly to x, for systems with Fe^{2+}, Fe^{3+}-Fe^{3+}, and Fe^{3+}-Al^{3+}, respectively. We plot density along a geotherm [112] and compare with ferropericlase and the preliminary reference Earth model (PREM) [115], as shown in Fig. 3.5. Our results show that (Fig. 3.6), at 110 GPa, the density of the pPv phase is higher than that of Pv by about 1.5% when Fe or Al presents, similar to that in pure $MgSiO_3$. The density difference between Pv and pPv decreases with the Fe^{3+}-Al^{3+} concentration, opposite to the trends in velocities differences; whereas it is less sensitive to Fe^{3+}-Fe^{3+} than to Fe^{3+}-Al^{3+}, similar to that in velocities.

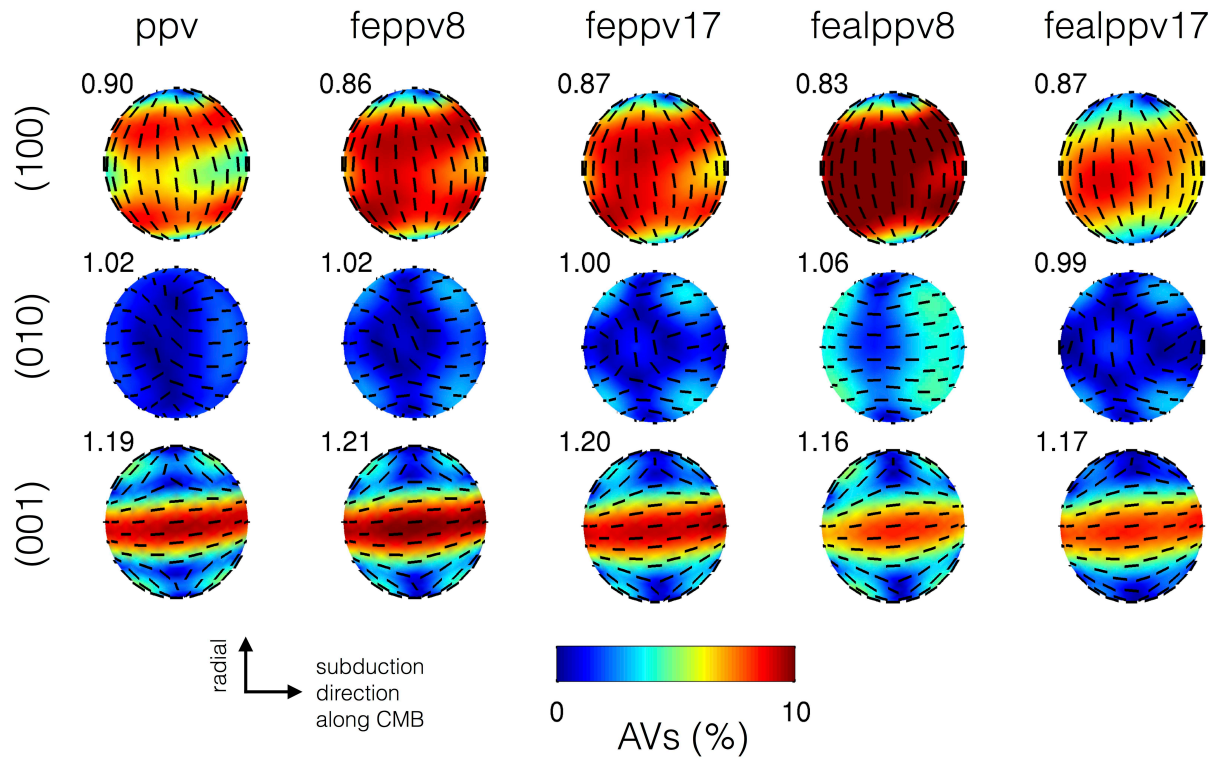

Figure 3.9: Shear wave splitting strength (AV_s, in color) and fast axis direction (black bar) shown as a function of seismic wave propagation direction on a sphere for the five different compositional model and three different sets of slips systems. The horizontal plane is parallel to the CMB with the direction of subduction to the right. The value for transverse isotropy, $\xi = V_{SH}^2/V_{SV}^2$, is given in the upper left corner of each subplot. Figure is made with Matlab Seismic Anisotropy Toolkit (Walker and Wookey, 2012) ppv: pure $MgSiO_3$ pPv; feppv8 or feppv17: Fe^{3+}-Fe^{3+} bearing $MgSiO_3$ with x=8% or 17%; fealppv8 or fealppv17: Fe^{3+}-Al^{3+} bearing $MgSiO_3$ with x=8% or 17%.

Table 3.5: Fit parameters for the sound velocities of ferric iron bearing Pv and pPv. V_p, V_s, and V_ϕ denote the compressional, shear, and bulk velocities, respectively. k and b are in units of km/(GPa·K·s), km/(K·s), km/(GPa·s), and km/s for A_0, A_1, A_2, and A_3, respectively.

	$A_0 - k$	b	$A_1 - k$	b	$A_2 - k$	b	$A_3 - k$	b
$(Mg_{1-x}Fe_x)(Si_{1-x}Fe_x)O_3$ Pv								
V_p	9.02E-06	1.99E-06	-1.43E-03	-3.58E-04	-1.02E-02	1.96E-02	-2.785	11.869
V_s	2.81E-07	2.01E-06	-4.80E-04	-3.81E-04	6.50E-03	4.60E-03	-3.963	7.132
V_ϕ	1.27E-05	6.76E-07	-1.57E-03	-1.07E-04	-2.44E-02	2.09E-02	0.551	8.630
$(Mg_{1-x}Fe_x)(Si_{1-x}Al_x)O_3$ Pv								
V_p	4.67E-06	1.58E-06	-1.64E-03	-3.26E-04	1.79E-03	2.01E-02	-0.833	11.857
V_s	-3.66E-06	1.56E-06	-6.59E-04	-3.44E-04	1.67E-02	5.24E-03	-2.130	7.091
V_ϕ	7.05E-06	5.55E-07	-1.30E-03	-1.01E-04	-1.03E-02	2.09E-02	0.578	8.647
$(Mg_{1-x}Fe_x)(Si_{1-x}Fe_x)O_3$ pPv								
V_p	-4.31E-06	1.13E-06	-4.54E-04	-2.67E-04	1.29E-02	2.07E-02	-4.225	11.867
V_s	5.03E-06	4.49E-07	-1.28E-03	-2.11E-04	-2.23E-02	9.53E-03	0.097	6.833
V_ϕ	-8.47E-06	8.94E-07	2.84E-04	-1.25E-04	3.09E-02	1.80E-02	-4.531	8.835
$(Mg_{1-x}Fe_x)(Si_{1-x}Al_x)O_3$ pPv								
V_p	1.62E-06	1.25E-06	-6.04E-04	-2.89E-04	2.88E-04	2.02E-02	-1.634	11.928
V_s	5.28E-06	5.39E-07	-1.18E-03	-2.20E-04	7.98E-04	8.93E-03	-1.132	6.891
V_ϕ	-3.70E-06	1.10E-06	3.70E-04	-1.61E-04	1.84E-03	1.76E-02	-1.168	8.892

Elastic anisotropy

The shear wave anisotropy $AV_S = |(V_{S1} - V_{S2})/((V_{S1} + V_{S2})/2)|$ of Fe/Al-bearing Pv and pPv are studied as functions of P and T [116] for waves traveling along the three axes. As expected from the structural differences between Pv and pPv, we found much higher AV_S in pPv than Pv (∼10-30% vs. ∼10%). In Pv, shear waves travelling along [001] are slightly more anisotropic than those along [100] and [010], while in pPv it is the opposite. The dependence of anisotropy on P and T is weak in general, potentially explained by the stability of the structures with compression or heating in lower-mantle conditions. Our results (Figs. 3.16 and 3.17 in the Appendix) also suggest that the inclusion of Fe or Al increases the anisotropy of $MgSiO_3$ pPv but this is not the case for Pv.

3.4 Geophysical implications

Mineralogical composition of the lower mantle

The above calculations enable us to consider mineral assemblages and evaluate their density and sound velocities. By comparing these results with a seismic velocity model, such as the PREM [115], one can propose a mineralogical composition for the lower mantle, which is

important for understanding the formation and evolution of the Earth and other planets, but impossible to directly determine.

To achieve this, we first examine a mixture of $Mg_{0.95}Fe_{0.05}SiO_3$:$(Mg_{1-x}Fe_x)(Si_{1-x}Fe_x)O_3$:$(Mg_{1-x}Fe_x)(Si_{1-x}Al_x)O_3$:$Fe_{0.125}Mg_{0.875}O$=34:10:43:13 (volume ratio), which corresponds to a mole ratio perovskite:ferropericlase=75:25, close to the pyrolitic composition that was proposed for the upper mantle [69], but is also widely assumed for the lower mantle. Here, the moduli and density values for $Mg_{0.95}Fe_{0.05}SiO_3$ and $Fe_{0.125}Mg_{0.875}O$ are based on [93] and [111], respectively. We find that, when choosing x=0.06 in $(Mg_{1-x}Fe_x)(Si_{1-x}Al_x)O_3$ and x=0.05 in $(Mg_{1-x}Fe_x)(Si_{1-x}Fe_x)O_3$, the velocities match PREM very well from 50 GPa to the top of the D″ (Fig. 3.7, top), and the agreement in density is also good (difference <1.2%).

In such an assemblage, the number of cations per 12 O is Mg: 4.48, Si: 3.45, Fe: 0.37, Al: 0.11, with Mg/Si=1.29 and Mg#=Mg/(Mg+Fe)=0.92, which are remarkably consistent with that in pyrolite (Mg/Si=1.27±0.06, Mg#=0.90±0.05, see Table 3.1). Therefore, neglecting minor phases such as $CaSiO_3$, we can conclude that the major part of the Earth's mantle resembles the pyrolitic model. This is in contrast to the silicon-rich model for the Earth's lower mantle and implies that the extra silicon relative to the CI chondrite may reside in the D″ region or the core [117].

At higher pressures when Pv can be less stable than pPv, we find that, with higher Al concentration in the pPv phase and less ferropericlase but with higher iron content, the velocities of the assemblage fit PREM values well in the high-pressure region (>105 GPa) (Fig. 3.7, bottom), although the density ρ is slightly higher (by 2.6%). If such an assemblage exists, the per 12 O cation numbers (Mg: 4.06, Si: 3.28, Fe: 0.68, Al: 0.33) indicate lower Mg/Si ratio (1.23) and Mg# (0.86), which still agree with that in pyrolite, but more Fe (Fe^{2+} and Fe^{3+} totals) and Al^{3+} than the major part of the mantle above. The increase in ferric iron ($Fe^{3+}/\Sigma Fe$ from 0.39 to 0.60) can only be partially explained by the $Fe^{2+}\rightarrow Fe^{3+}$ transformation driven by charge disproportionation, considering the low oxygen fugacity of the lower mantle [65]; the remaining must be related to the existence of Al^{3+} in the silicates. However, there are shortcomings to this approach in the D″. First, the Brown and Shankland geotherm that we are using here neglects the steep thermal gradient expected near the core-mantle boundary (CMB). In the lowermost few hundred kilometers, the temperature could be underestimated by a few hundred to 1500 K, which in turn means that the velocities and the density of the mineral assemblage are overestimated (by about 1% for V_p, 2% for V_s, and 1% for ρ). Including the temperature effects could support an assemblage with the same composition throughout the lower mantle (Fig. 3.8), which currently overestimates V_p, V_s, and ρ by 1.0%, 1.7%, and 1.3%, respectively, in the pPv region. Second, the Voigt averaging scheme for pPv is also associated by an uncertainty of ∼1% for V_p and V_s (see Table 3.10 in the Appendix). Lastly, both velocity (e.g. [118]) and density variations (e.g. [119, 120]) are significant in the lowermost mantle and could reflect significant thermal and compositional variations (e.g. [121]).

Seismic anisotropy

While the lower mantle is thought to be mostly isotropic, seismic anisotropy is observed in D″. The main characteristic is that horizontally polarized waves travel faster than vertically polarized ones (or $\xi = V_{SH}^2/V_{SV}^2 > 1$) in regions beneath subducting slabs in regional studies as well as in global models. Observations of seismic anisotropy in D″ are often explained by crystal preferred orientation in post-perovskite [122], but these studies have so far ignored major element composition. Based on the elastic constants in this study, we forward model the resulting texture and seismic anisotropy in perovskite and post-perovskite using the Viscoplastic Self-Consistent (VPSC) method [123] and deformation information from a typical tracer within a subducting slab [122]. While many slip systems are active within the model, we denote different experiments by the slip plane of their most active slip system. For perovskite this is (001), while for post-perovskite this is either (100), (010) or (001) [122]. For the perovskite model with dominant (001) slip we see an incompatible signature of $\xi < 1$ across all compositions, pressures and temperatures, and we do not show these results here.

The resulting shear wave splitting and ξ values for post-perovskite are shown in Fig. 3.9 at 100 GPa and 2500 K. Overall, we see that the transverse isotropy scales with the strength and orientation of splitting in the horizontal plane. The (100) and (001) cases show consistent signs in ξ with major element composition: (100) produces a signature opposite from the one seen in seismology, while (001) is consistent with seismology. The resulting ξ for the (010) case on the other hand is close to 1 and varies in amplitude; ξ increases for $x = 8\%$ compared to $x = 0\%$, but loses all amplitude when x=17%. Regardless of this trend, the amplitudes of ξ for the (010) case are too weak to explain seismic observations. Generally, seismic observations will underestimate the actual amplitudes at depth, while our modeling will overestimate the amplitudes due to assuming pure dislocation creep as the deformation mechanism and by excluding the presence of periclase. This leaves the (001) case as the only compatible mechanism for seismic transverse isotropy, insensitive to the amount of Fe or Al included. None of the models predict strong azimuthal anisotropy, i.e. splitting through the vertical axis.

3.5 Summary

The thermoelasticity of pure, as well as Fe- and Al-bearing $MgSiO_3$ bridgmanite and post-perovskite have been calculated at a variety of P, T conditions and Fe or Al compositions. Our results show that the presence of Fe, especially Fe^{3+}, and Al results in complicated characteristics in the elastic and seismic properties of these minerals, depending on the their content and distribution, the phase of the mineral, and the P, T conditions. Our results, when combined with values previously calculated for (Fe,Mg)O, allow us to calculate the seismic properties of mineral assemblages and thus explore the probable composition of the lower mantle. We show that the average lower mantle seismic velocities and density can be fit with a pyrolitic composition. We also study the transverse anisotropy of these minerals in

Table 3.6: Elastic and seismic properties of $MgSiO_3$ pPv at 125 GPa and 3500 K calculated with different supercell sizes. The values in parenthesis are the error on the last digit of the corresponding values.

supercell	K^S[GPa]	G[GPa]	V_ϕ[km/s]	V_s[km/s]	V_p[km/s]
$3\times1\times1^a$	645(8)	298(7)	10.95(7)	7.45(8)	13.92(8)
$4\times1\times1^b$	644(9)	301(8)	10.94(8)	7.48(10)	13.94(10)
$4\times2\times2^c$	644(4)	291(4)	10.95(4)	7.36(5)	13.86(5)

[a] c/a=2.459, b/a=3.244, ρ=5373 kg/m^3
[b] c/a=2.471, b/a=3.261, ρ=5378 kg/m^3
[c] c/a=2.477, b/a=3.268, ρ=5365 kg/m^3

a subducting slab near the CMB, and confirm that the pPv phase with predominant (001) slip plane matches the seismic anisotropy in the D″ region independent of the amount of Fe or Al. These results provide a useful resource that can be used to investigate the effect of impurities on the properties of mineral assemblages in the deep mantle.

3.6 Appendix

Dependence on supercell size

Both the 2×2×1 supercell for Pv and 3×1×1 supercell for pPv have been used in a number of previous studies. To confirm that finite-size effects are not an issue for supercells of this size we computed, we computed elastic and seismic properties using three different pPv supercells. The results are listed in Table 3.6, and show excellent agreement.

Dependence on k-mesh

To test convergence with respect to k-point sampling we compare the elastic and seismic properties of $MgSiO_3$ pPv calculated using four different Monkhorst-Pack k-meshes [99] in the NVT stage (Table 3.7). A separate test using a denser k-mesh at the NPT and Γ-point at the NVT stage is compared with the Γ-only calculations for pPv at 125 GPa and 2500 K (Table 3.8).

DFT+U for better accounting the correlation effects

We performed DFT+U calculations for a Fe^{3+}-bearing Pv structure (fepv6) with one Fe-Fe pair taking an A (HS) and a B (LS) site, respectively, in the unit cell, at 125 GPa and 2500 K. The results (Table 3.9) show remarkable consistency with standard LDA calculations on sound velocities and seismic properties.

Table 3.7: Elastic and seismic properties of $MgSiO_3$ pPv at 125 GPa and 3500 K calculated with the 3×1×1 supercell and different k-meshes during NVT. The values in parenthesis are the error on the last digit of the corresponding values.

k-mesh	K^S[GPa]	G[GPa]	V_ϕ[km/s]	V_s[km/s]	V_p[km/s]
Γ-only	645(8)	298(7)	10.95(7)	7.45(8)	13.92(8)
2×2×2	667(10)	284(8)	11.14(9)	7.27(10)	13.95(10)
3×3×3	626(12)	292(9)	10.79(11)	7.37(11)	13.74(12)
4×4×4	641(14)	292(11)	10.92(12)	7.37(14)	13.84(13)

Table 3.8: Elastic and seismic properties of $MgSiO_3$ pPv at 125 GPa and 2500 K calculated with the 3×1×1 supercell and different k-meshes during NPT and Γ-only during NVT. The values in parenthesis are the error on the last digit of the corresponding values.

k-mesh	K^S[GPa]	G[GPa]	V_ϕ[km/s]	V_s[km/s]	V_p[km/s]
Γ-only[a]	655(7)	315(5)	10.97(6)	7.61(6)	14.05(6)
2×2×2[b]	668(7)	318(5)	11.09(6)	7.65(6)	14.17(7)

[a] c/a=2.463, b/a=3.246, ρ=5444 kg/m^3
[b] c/a=2.464, b/a=3.247, ρ=5438 kg/m^3

Simulation length and stress-strain linearity

The statistical average of the 6 stress components and their convergence with the length of the NVT-MD simulations are illustrated in Fig. 3.10. Good convergence is typically reached in 5 ps.

The elastic constants derived from different stress-strain relations are compared in Fig. 3.11. The consistence shows the reliability of the calculated elastic constants based on our choice of strain $\epsilon = \pm 0.5\%$ and good linearity at such small strains.

Pressure correction

We start from the ambient-condition volume of $MgSiO_3$ perovskite from the experiments of [124] and [125] and estimate[3] the true unit cell volume at T=0 K to be 161.8∼162.8 Å^3. LDA calculations with the volume of the $MgSiO_3$ perovskite cell fixed at these values return pressures $P^{\rm LDA} = -3.5 \sim -5.0$ GPa. Therefore, we choose ΔP=+4.0 GPa as a rigid shift to the calculated pressures to reconcile the methodological underestimation, and assume it is independent of mineral phases in this study. This choice is consistent with the inadequate

[3] $\int_{V_0}^{V_{\rm RT}} d\ln V = \int_0^{300} (\partial \ln V/\partial T)\, dT = \int_0^{300} \alpha(T) dT$, assuming $\alpha(T) = AT$ with A being a constant and $\alpha(T = 300\,{\rm K}) = 2 \times 10^{-5}\,{\rm K}^{-1}$ [53], we get $V_0 = V_{\rm RT}/\exp\left[300 \times \frac{\alpha(T=300\,{\rm K})}{2}\right] = 0.997 V_{\rm RT}$.

Table 3.9: Comparison on elastic constants, bulk and shear moduli, sound velocities, and transverse isotropy at different slip planes of $(Mg_{1-x}Fe_x)(Si_{1-x}Fe_x)O_3$, x=6.25% (fepv6) at 100 GPa and 2500 K calculated by LDA and four different types of LDA+U: NVT only, both NPT and NVT (relax), same U for Fe at A and B sites, different U for Fe at A and B sites. The values in parenthesis are the error on the last digit of the corresponding values.

Fepv6,HS-LS	LDA[a]	LDA+U#1[b]	LDA+U#2[c]	LDA+U#3[d]	LDA+U#4[e]
ρ [kg/m^3]	5300	5300	5300	5300	5296
C_{11}[GPa]	752(29)	732(38)	729(38)	689(31)	749(34)
C_{22}[GPa]	958(37)	957(33)	955(31)	901(30)	1040(29)
C_{33}[GPa]	894(22)	895(27)	895(27)	922(31)	842(38)
C_{12}[GPa]	482(11)	485(11)	480(11)	507(11)	492(10)
C_{13}[GPa]	361(10)	364(11)	363(11)	358(10)	350(11)
C_{23}[GPa]	362(10)	366(10)	370(10)	407(10)	352(10)
C_{44}[GPa]	268(19)	270(20)	271(19)	277(17)	282(21)
C_{55}[GPa]	226(17)	220(13)	220(13)	221(23)	209(14)
C_{66}[GPa]	289(24)	293(26)	287(28)	244(30)	258(24)
K[GPa]	558(10)	557(11)	557(11)	562(10)	558(11)
G[GPa]	250(8)	248(9)	247(9)	231(10)	246(9)
V_ϕ[km/s]	10.26(9)	10.26(10)	10.25(10)	10.30(10)	10.27(10)
V_s[km/s]	6.87(11)	6.84(12)	6.82(12)	6.61(14)	6.81(12)
V_p [km/s]	12.97(11)	12.95(11)	12.93(11)	12.82(12)	12.93(11)
$\xi(001)$	0.96(8)	0.96(8)	0.95(8)	0.78(8)	0.93(8)
$\xi(100)$	1.07(8)	1.07(7)	1.08(8)	1.14(11)	1.23(9)
$\xi(010)$	0.82(6)	0.79(7)	0.80(7)	0.85(7)	0.80(7)

[a] $2c/3a$=0.968, b/a=1.055
[b] U=6
[c] $U1$=6, $U2$=4.8
[d] U=6, including structural relaxation; ; $2c/3a$=0.968, b/a=1.055
[e] $U1$=6, $U2$=4.8, , including structural relaxation; $2c/3a$=0.968, b/a=1.054

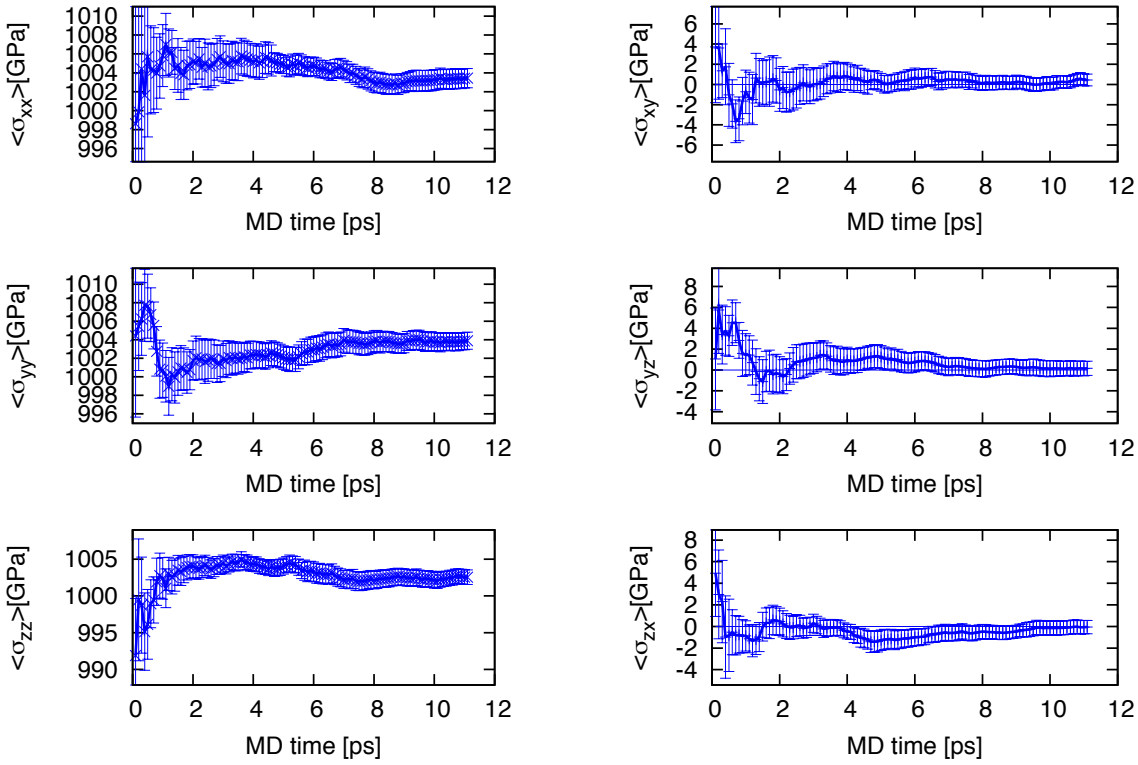

Figure 3.10: The statistical average of the six stress components calculated as functions of the length of the molecular-dynamic simulations.

value (1.9 GPa) suggested in [68] and similar to the finding in recent quantum Monte Carlo calculations [53].

Averaging schemes

We used the Voigt scheme for estimating the polycrystal bulk and shear moduli K and G from C_{ij}'s, for each mineral. However, it is worth noting that, the difference using the Voigt-Reuss-Hill (VRH) scheme is negligible for Pv; but the difference on G, V_s, and V_p are evident for pPv, as shown in Table 3.10. We also find that the differences increase with pressure, but are barely dependent on temperature.

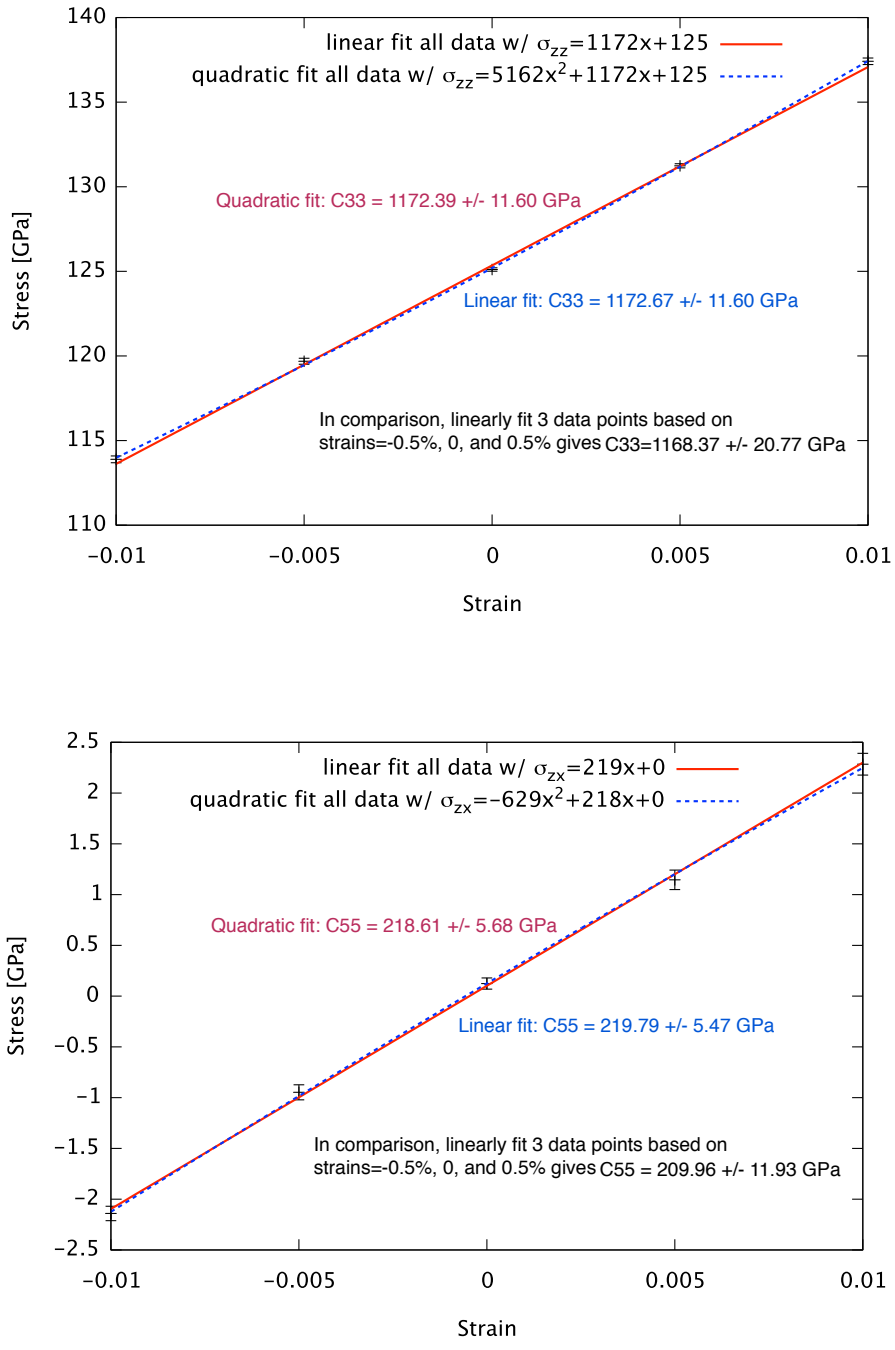

Figure 3.11: Comparison on elastic constants of $(Mg_{0.92}Fe_{0.08})(Si_{0.92}Al_{0.08})O_3$ at 125 GPa and 2500 K (C_{33} on the left and C_{55} on the right) calculated by assuming linear or quadratic stress-strain relations. Using the small strains chosen here (0.5%), the linearity is evident.

Table 3.10: Comparison between the elastic and seismic properties of different minerals calculated using the Voigt (V) and the Voigt-Reuss-Hill (VRH) scheme at 125 GPa and 2500 K. $\Delta K^S = K^S_{\rm V} - K^S_{\rm VRH}, \Delta G = G_{\rm V} - G_{\rm VRH}, \Delta V_\phi = V_{\phi,{\rm V}}$-$V_{\phi,{\rm VRH}}, \Delta V_s = V_{s,{\rm V}}$-$V_{s,{\rm VRH}}, \Delta V_p = V_{p,{\rm V}} - V_{p,{\rm VRH}}$, Density, moduli, and velocities are in units of kg/m^3, GPa, and km/s, respectively.

ρ	K^S_V	ΔK^S	G_V	ΔG	$V_{\phi,V}$	ΔV_ϕ	$V_{s,V}$	ΔV_s	$V_{p,V}$	ΔV_p
Pv										
$MgSiO_3$										
5367	673(6)	6	288(5)	5	11.20(5)	0.05	7.32(7)	0.06	14.03(6)	0.08
$(Mg_{1-x}Fe_x)(Si_{1-x}Al_x)O_3$	x=6.25%									
5451	655(7)	5	270(6)	2	10.96(6)	0.04	7.04(7)	0.03	13.65(7)	0.06
$(Mg_{1-x}Fe_x)(Si_{1-x}Fe_x)O_3$	x=6.25%									
5541	664(7)	4	285(6)	4	10.95(6)	0.04	7.17(7)	0.05	13.72(7)	0.06
$(Mg_{1-x}Fe_x)(Si_{1-x}Al_x)O_3$	x=12.5%									
5544	658(7)	3	263(5)	6	10.89(6)	0.02	6.89(7)	0.07	13.49(7)	0.07
$(Mg_{1-x}Fe_x)(Si_{1-x}Fe_x)O_3$	x=12.5%									
5713	678(8)	6	266(7)	5	10.89(6)	0.04	6.82(10)	0.07	13.44(8)	0.08
pPv										
$MgSiO_3$										
5444	655(7)	5	315(5)	9	10.97(6)	0.04	7.61(6)	0.11	14.05(6)	0.11
$(Mg_{1-x}Fe_x)(Si_{1-x}Al_x)O_3$	x=8.3%									
5558	665(7)	1	289(6)	11	10.94(6)	0.01	7.21(8)	0.14	13.75(7)	0.11
$(Mg_{1-x}Fe_x)(Si_{1-x}Fe_x)O_3$	x=8.3%									
5674	668(7)	2	299(5)	11	10.85(6)	0.02	7.26(6)	0.13	13.71(6)	0.11
$(Mg_{1-x}Fe_x)(Si_{1-x}Al_x)O_3$	x=16.7%									
5670	676(7)	1	308(5)	10	10.92(5)	0.01	7.37(6)	0.12	13.84(6)	0.09
$(Mg_{1-x}Fe_x)(Si_{1-x}Fe_x)O_3$	x=16.7%									
5902	657(8)	3	268(6)	10	10.55(6)	0.02	6.75(8)	0.14	13.12(7)	0.11

Equation of state

Two formalisms of EOS are often used in describing the pressure-volume relation of materials: 1) Birch-Murnaghan EOS [126]

$$P(f) = 3K_0 f(1+2f)^{\frac{5}{2}}\left[1 + \frac{3}{2}(K_0' - 4)f + \cdots\right], \tag{3.4}$$

where $f = \left[(V/V_0)^{-2/3} - 1\right]/2$ is the Eulerian strain; and 2) Vinet EOS [127]

$$P(x) = 3K_0(1-x)x^{-2}\exp\left[3(K_0' - 1)(1-x)/2\right], \tag{3.5}$$

where $x = (V/V_0)^{1/3}$.

Quantities such as the bulk modulus K can be determined from the EOS. For example, based on the widely used 3$^{\text{rd}}$-order Birch-Murnaghan equation (Eq. 3.4 neglecting the ellipsis), and denoting $\delta = -3(K_0' - 4)/4$, we have

$$K = -\frac{\partial P}{\partial \ln V} = K_0(1+2f)^{\frac{5}{2}}\left[1 + 7f - 2\delta f(2+9f)\right]. \tag{3.6}$$

Benchmarking structures and bulk moduli

We have compared the structure of pure $MgSiO_3$ Pv and pPv with previous reports, including both experiments and theory. The calculated compression behavior for Pv and pPv are shown in Fig. 3.12. Comparing with experiments, the agreement is good for both Pv and pPv. We also fit the pressure-density data to Vinet and to 3rd-order Birch Murnaghan EOS, and obtain consistent values for ambient density and bulk modulus for Pv. For pPv, the agreement is fair for lacking of data at low pressures because we are focusing on the high-pressure region that is geophysically interesting.

In order to gain a better understanding of our calculation results, we look deeper into the structures from our DFT-MD simulations in the NPT ensemble by comparing the axial ratio with more previous works. The results for both Pv and pPv have been summarized in Fig. 3.13. As we can see, the agreement in lattice constants is not always good. Specifically, the axial ratios at 0 K are higher than that extrapolated from high-temperature simulations by $\sim$0.65% for pPv and a smaller amount for Pv; for pPv, the calculated b/a and c/a are 0.6% smaller than the experiment by [128] at high temperature; for Pv, the calculated b/a is larger at high temperature by 1% than that from [128], and $2c/3a$ smaller by 0.5% at ambient temperature. On the other hand, our calculation is in good agreement with previous calculations by [68] on Pv and [109] and [80] on pPv, as well as some high-T experiments by [129] on Pv and low-T measurements by [128]. Looking into the discontinuity at 0 K, we found that it is mainly induced by the denser k mesh implemented in the static calculations. If using Γ-point only, the axial ratios become smooth functions of temperature. This indicates that the pPv structures that we obtained from Γ-point only MD simulations intrinsically embrace some amount of strain ($< 1\%$), which could result in changes in the elastic coefficients and moduli by about 10 GPa. This, however, is of the same order of magnitude as the uncertainty of these quantities from our calculation, and is the best we can do for now, considering the prone-to-instability NPT simulations and general expensiveness of MD calculations.

We further benchmark the bulk modulus of iron-bearing $MgSiO_3$. Fig. 3.14 compares on our calculation with experimental values (from [130]) at two pressures (80 and 125 GPa). Note that both theoretical and experimental data have high (generally over 10 GPa) uncertainty. The overall consistency at 300 K is good, although the confidence level of our results at 300 K is lower than at high temperatures (1500-3500 K), at which the current thermoelasticity study has been carried out. For Fe^{3+}-Fe^{3+} bearing Pv at 80 GPa, the only available experimental data point does not agree with our calculation, future experimental measurements are required to resolve this.

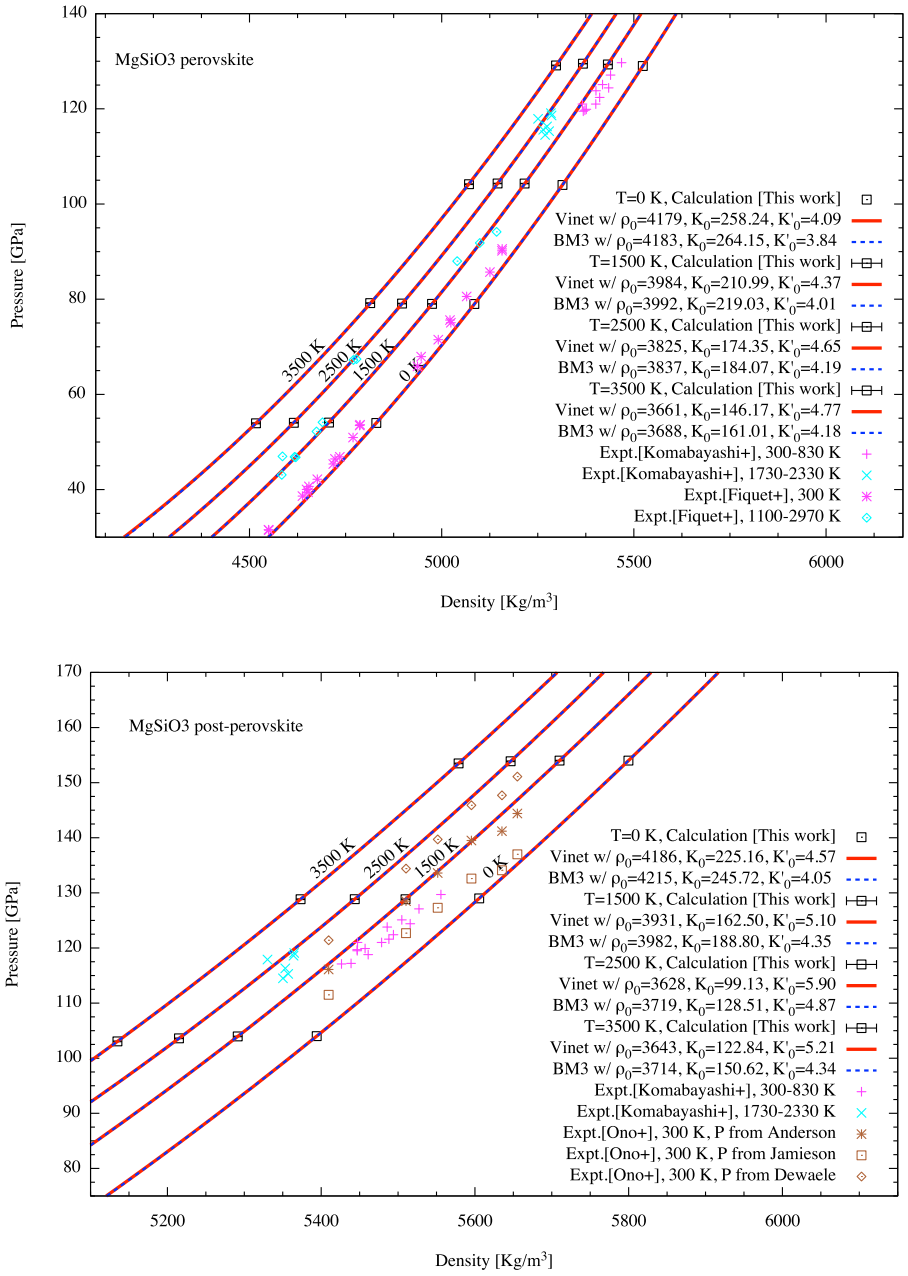

Figure 3.12: The pressure-density relation of Pv and pPv from current calculation (dark squares) and EOS fits (red solid line for Vinet, blue dashed line for 3rd-order Birch-Murnaghan) along four different isotherms 0, 1500, 2500, and 3500K, in comparison with experimental measurements. The theoretical pressures have been uniformly uplifted by ΔP=4.0 GPa to account for the deficiency of LDA in underestimating the pressure. The EOS parameters are from fitting the original data (without pressure shift), in order to avoid error accumulation.

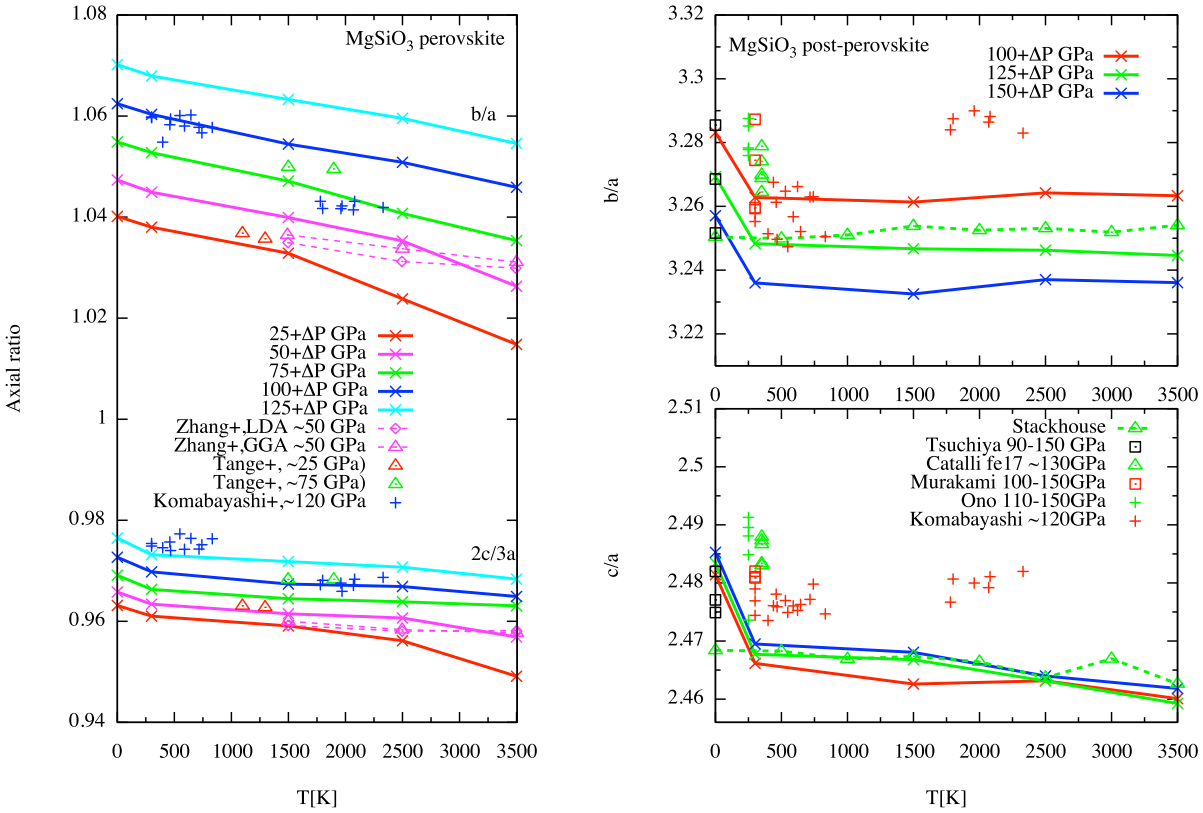

Figure 3.13: The axial ratios of $MgSiO_3$ Pv and pPv as a function of temperature, in comparison with previous theoretical and experimental reports. ΔP denotes the pressure correction on our LDA calculations.

Summary of all elasticity data

Fig. 3.15 shows the calculated elastic constants as functions of pressure for pure $MgSiO_3$ Pv and pPv. The agreement with a recent calculation on Pv reconfirms the reliability of present calculations. The temperature derivatives of elastic constants of pPv at 125 GPa are summarized in Table 3.11, comparing with previous studies and that of Pv. The fit parameters (using Eq. 3.3 in the main context) for C_{ij} are summarized in Table 3.12. Detailed lists of the density, elasticity, and seismic properties for ferrous iron bearing Pv and pPv can be found in Table 3.13; the data for ferric iron bearing Pv and pPv are listed in Table 3.14.

The shear wave anisotropy of pure and Fe/Al-bearing Pv and pPv as functions of pressure and temperature are summarized in Figs. 3.16 and 3.17. The transverse isotropy $\xi = V_{SH}^2/V_{SV}^2$ for different Pv and pPv phases as functions of pressure is shown in Fig. 3.18. The

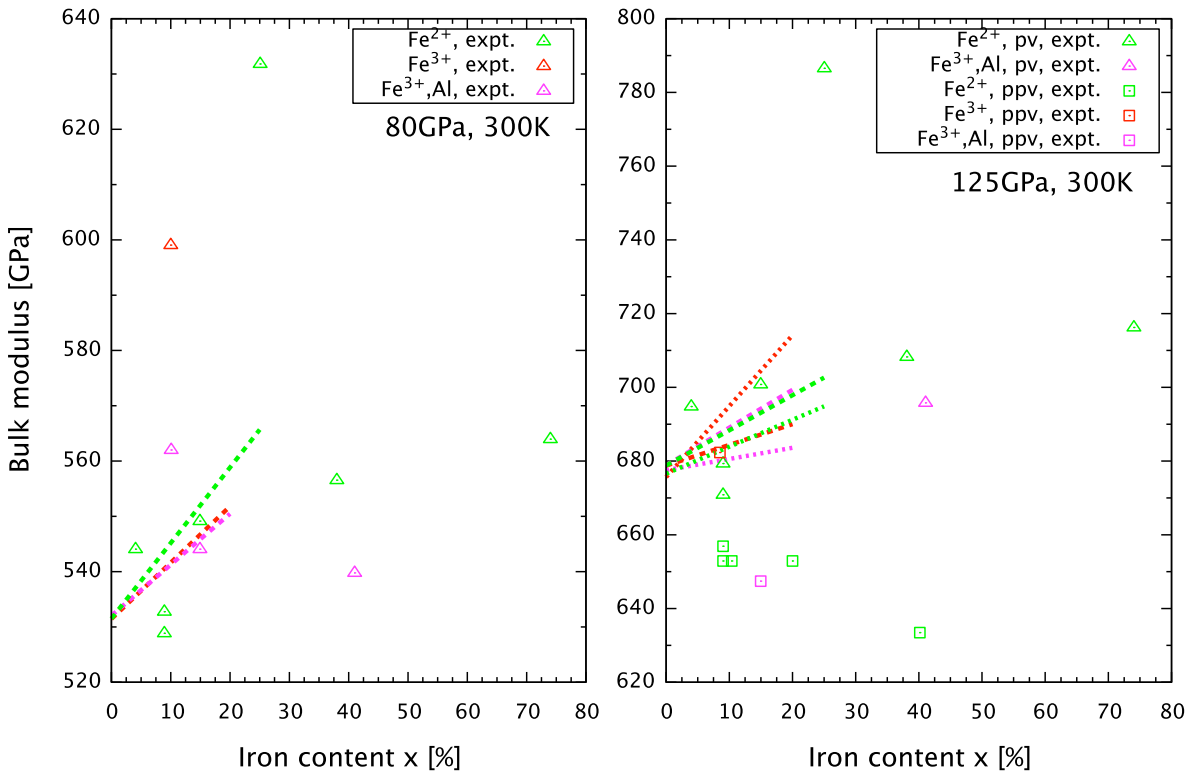

Figure 3.14: The bulk modulus of iron-bearing $MgSiO_3$ Pv and pPv as a function of iron content. Green, red, and pink represent Fe^{2+}, Fe^{3+}-Fe^{3+}, and Fe^{3+}-Al^{3+} bearing systems, respectively. Our data extrapolated to 300 K for Pv (dashed lines) and pPv (dotted lines) are compared with experimental results (shown in the legend, data are from Figures 2 and 4 in [130]). Uncertainties are generally over 10 GPa and are not shown for clarity.

Table 3.11: Temperature derivative of adiabatic elastic constants (in units of GPa/K) of pure and Fe/Al-bearing pPv and Pv at 125 GPa. The numbers in parenthesis are the uncertainties on the last digit of the value. SB07 and RW06 denote previous calculations by Refs. [75] and [73], respectively.

dC_{11}/dT	dC_{22}/dT	dC_{33}/dT	dC_{12}/dT	dC_{13}/dT	dC_{23}/dT	dC_{44}/dT	dC_{55}/dT	dC_{66}/dT
pPv $MgSiO_3$								
-0.037(13)	-0.039(15)	-0.038(14)	0.009(9)	-0.018(9)	-0.013(8)	-0.005(8)	-0.024(6)	-0.025(9)
$(Mg_{1-x}Fe_x)(Si_{1-x}Fe_x)O_3$ x=8.3%								
-0.045(16)	-0.033(14)	-0.067(15)	-0.005(10)	0.010(10)	-0.006(10)	0.015(13)	-0.011(7)	-0.042(10)
$(Mg_{1-x}Fe_x)(Si_{1-x}Fe_x)O_3$ x=16.7%								
-0.052(18)	-0.039(12)	-0.067(13)	-0.030(10)	-0.011(10)	-0.014(10)	-0.003(14)	-0.027(6)	-0.037(9)
$(Mg_{1-x}Fe_x)(Si_{1-x}Al_x)O_3$ x=8.3%								
-0.027(12)	-0.009(16)	-0.056(15)	0.012(9)	0.012(10)	-0.011(11)	-0.013(10)	-0.026(9)	-0.038(11)
$(Mg_{1-x}Fe_x)(Si_{1-x}Al_x)O_3$ x=16.7%								
-0.034(14)	-0.036(15)	-0.046(13)	-0.006(8)	-0.009(9)	-0.021(8)	0.009(9)	-0.027(6)	-0.026(10)
$MgSiO_3$, pPv SB07								
-0.046	-0.024	-0.046	-0.005	-0.003	-0.003	-0.012	-0.014	-0.029
$MgSiO_3$, pPv RW06								
-0.083	-0.037	-0.069	0.001	0.022	-0.005	-0.011	-0.028	-0.045
Pv $MgSiO_3$								
-0.039(11)	-0.040(11)	-0.029(11)	-0.008(9)	-0.006(9)	0.007(9)	-0.025(6)	0.003(4)	-0.009(9)
$(Mg_{1-x}Fe_x)(Si_{1-x}Fe_x)O_3$ x=6.25%								
-0.024(17)	-0.068(14)	-0.049(15)	0.001(10)	-0.003(10)	0.002(10)	-0.020(8)	0.000(6)	-0.017(9)
$(Mg_{1-x}Fe_x)(Si_{1-x}Fe_x)O_3$ x=12.5%								
-0.035(17)	-0.065(20)	-0.020(17)	0.003(12)	-0.013(12)	0.010(12)	-0.026(12)	0.012(9)	-0.036(12)
$(Mg_{1-x}Fe_x)(Si_{1-x}Al_x)O_3$ x=6.25%								
-0.029(12)	-0.057(15)	-0.050(14)	-0.004(9)	-0.010(9)	-0.005(10)	-0.035(6)	-0.019(5)	-0.033(9)
$(Mg_{1-x}Fe_x)(Si_{1-x}Al_x)O_3$ x=12.5%								
-0.060(11)	-0.053(13)	-0.035(13)	0.006(8)	-0.006(9)	-0.006(10)	-0.013(7)	-0.018(6)	-0.032(9)

transverse isotropy of single-crystal and textured pPv phases are compared as functions of pressure in Fig. 3.19.

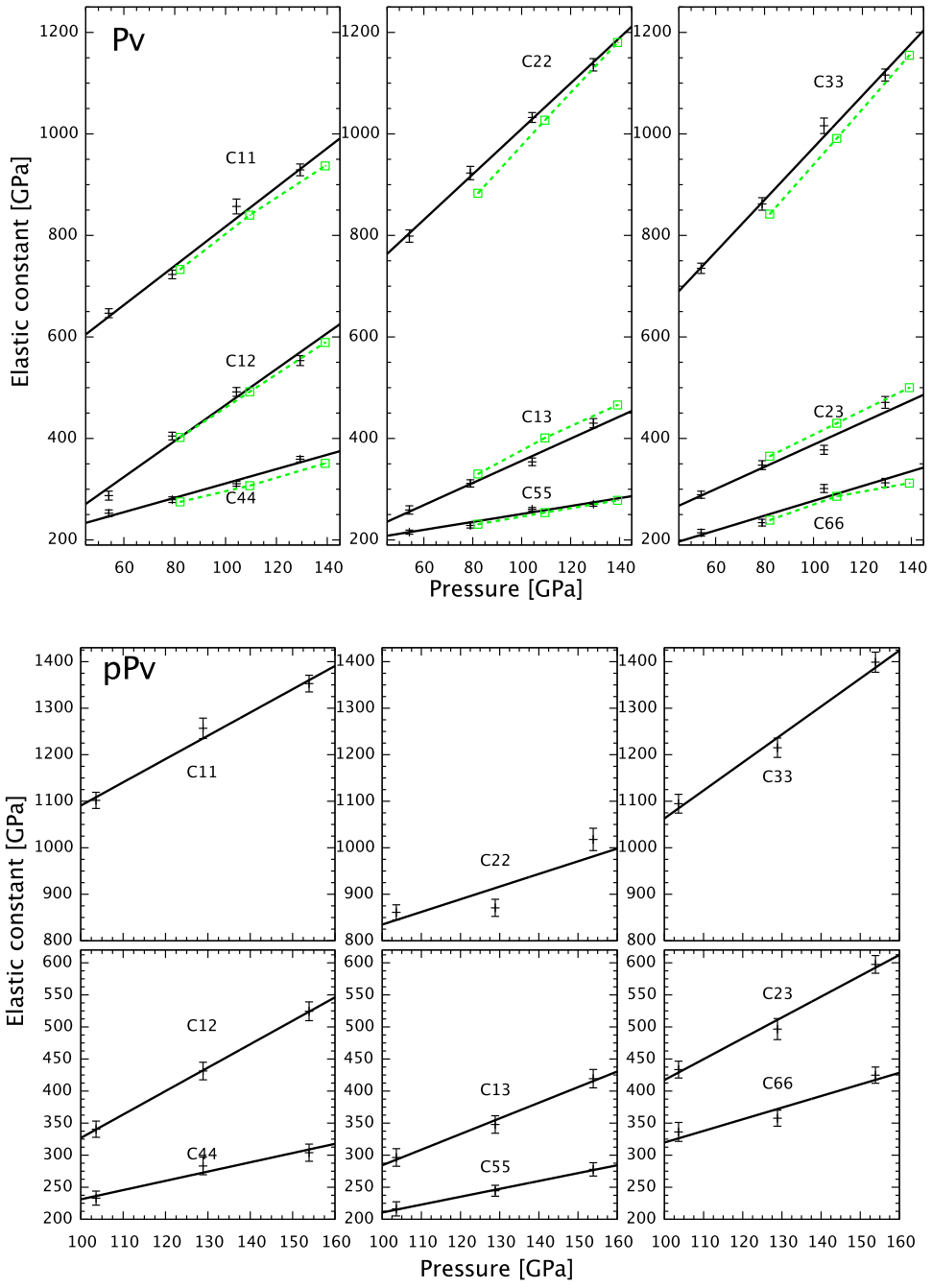

Figure 3.15: The pressure dependence of elastic constants of pure $MgSiO_3$ Pv (top) and pPv (pPv) at 2500 K. Previous calculations by [68] are shown in green dashed line points for comparison. A pressure correction of 4.0 GPa and 1.9 GPa has been applied to the data of ours and of Ref. [68], respectively.

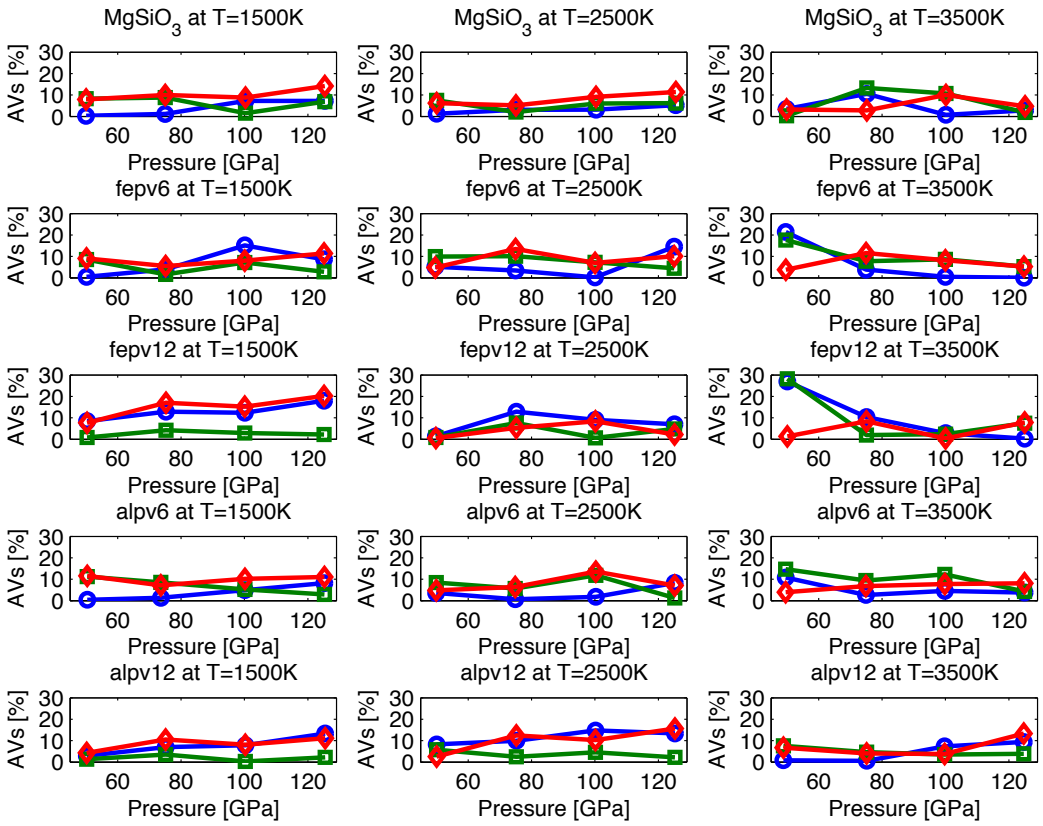

Figure 3.16: The shear anisotropy of pure and Fe/Al-bearing Pv as a function of pressure along three isotherms relevant to the Earth's lower mantle temperatures. Blue, green, and red lines correspond to shear waves propagating along the [100], [010], and [001] direction, respectively.

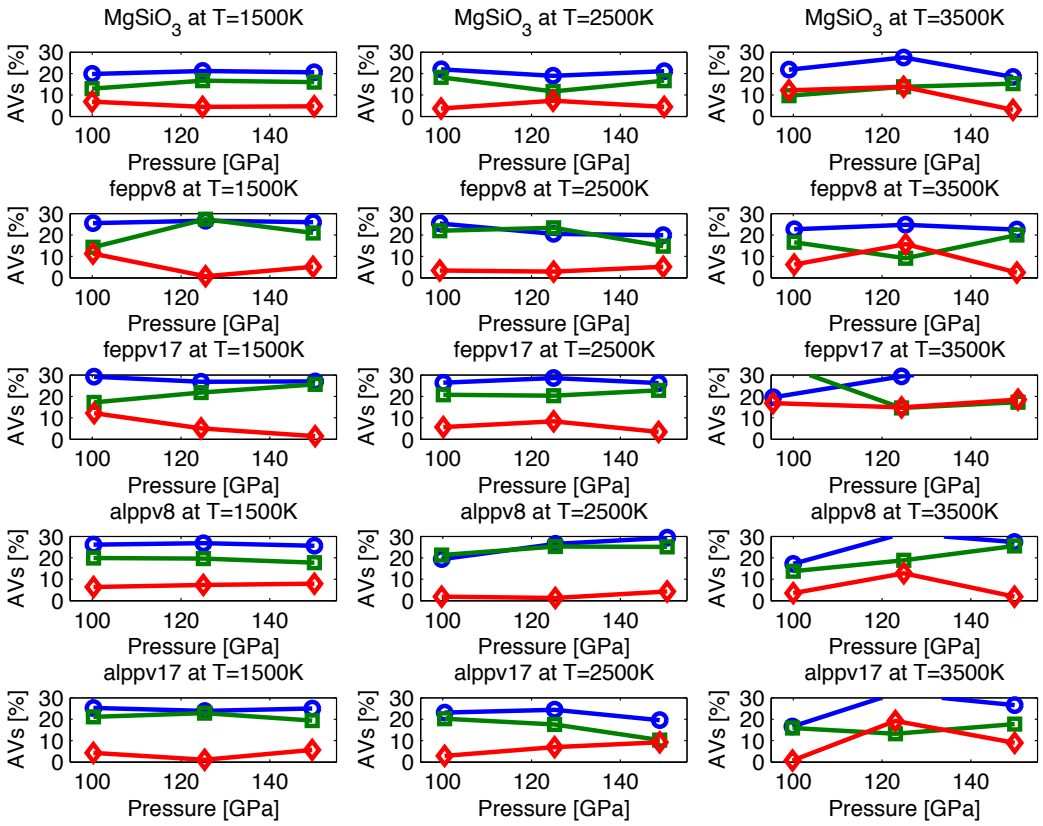

Figure 3.17: The shear anisotropy of pure and Fe/Al-bearing pPv as a function of pressure along three isotherms relevant to the Earth's lower mantle temperatures. Blue, green, and red lines correspond to shear waves propagating along the [100], [010], and [001] direction, respectively.

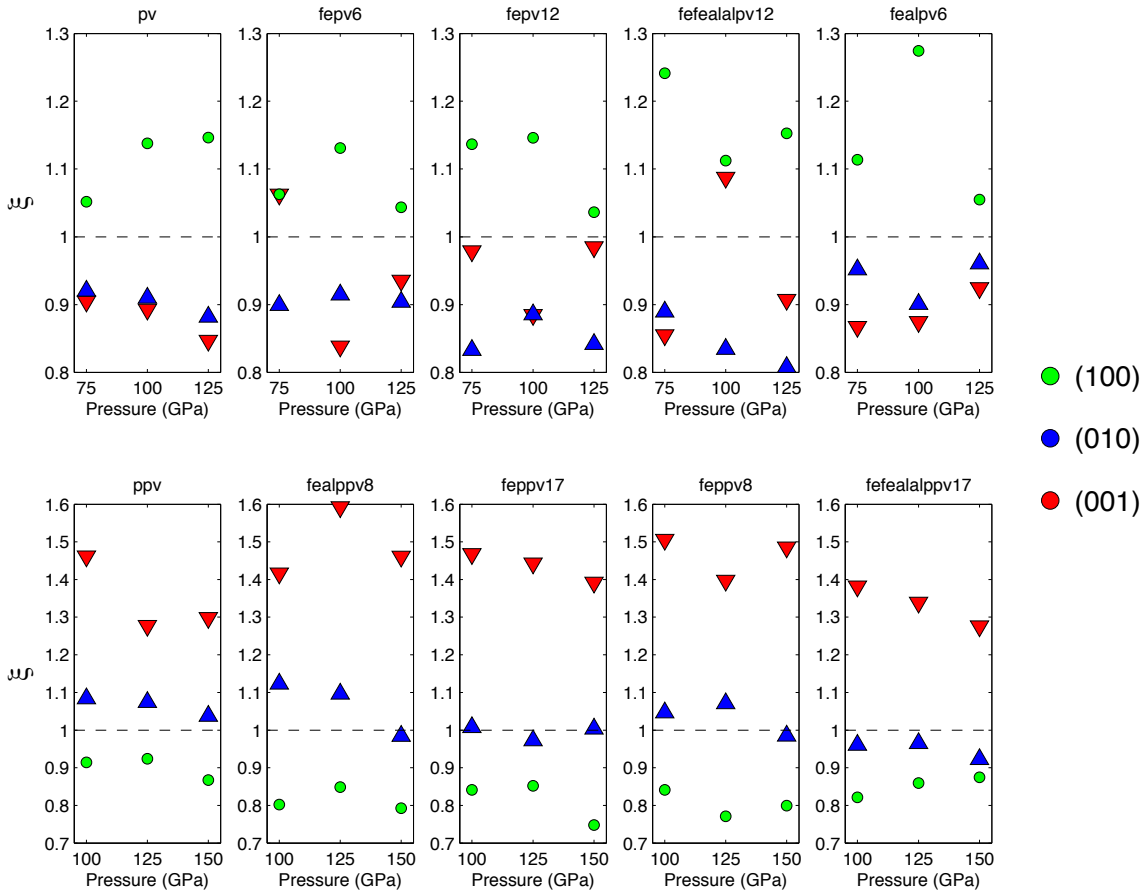

Figure 3.18: The transverse isotropy for different single-crystal Pv and pPv phases at T=2500 K. The errorbar is about 0.1. Red down triangles, blue up triangles, and green spheres denote split planes (001), (010), and (100), respectively.

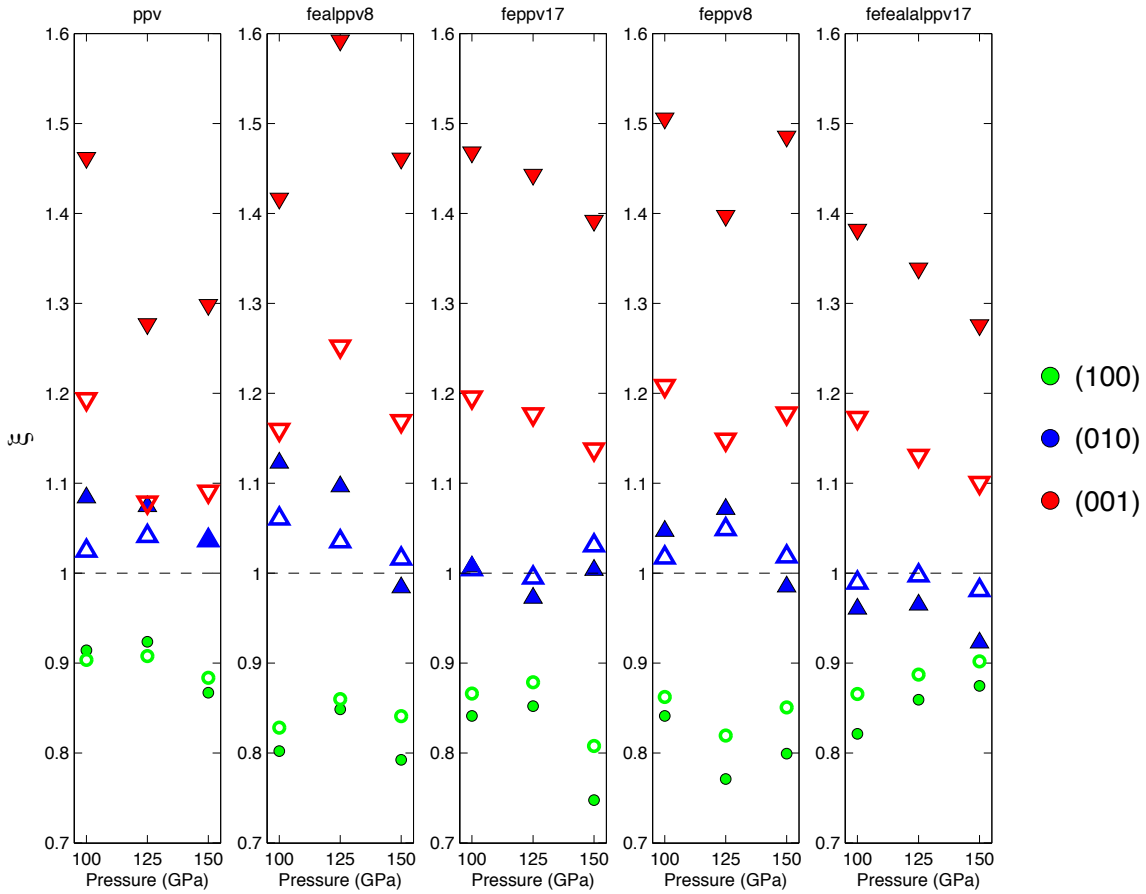

Figure 3.19: The transverse isotropy for single-crystal (filled symbol) and textured (open symbol) pPv phases at T=2500 K. Red down and blue up triangles, and green spheres denote (001), (010), and (100) split planes, respectively.

Table 3.12: Fitting parameters (corresponding to Eq. 3.3 in the main text) for the elastic constants of Fe/Al-bearing Pv and pPv. k and b are in units of 1/K, GPa/K, 1, and GPa for A_0, A_1, A_2, and A_3, respectively.

	A_0-k	b	A_1-k	b	A_2-k	b	A_3-k	b
$(Mg_{1-x}Fe_x)(Si_{1-x}Fe_x)O_3$ Pv								
C_{11}	5.44E-03	-2.12E-04	-5.39E-01	-1.25E-02	1.86E-02	6.27E+00	4.28E-01	5.64E+02
C_{12}	3.77E-03	-1.25E-04	-3.76E-01	9.70E-03	1.41E-02	4.72E+00	3.42E-01	4.26E+02
C_{44}	-1.90E-03	1.06E-04	1.08E-01	-2.75E-02	1.04E-02	3.90E+00	2.37E-01	3.57E+02
C_{22}	-5.40E-03	5.23E-04	3.96E-01	-9.40E-02	1.78E-02	6.72E+00	4.39E-01	6.20E+02
C_{13}	1.01E-03	-9.98E-05	-1.78E-01	1.25E-02	1.40E-02	4.50E+00	3.25E-01	4.08E+02
C_{55}	-9.69E-04	2.04E-04	1.50E-01	-2.56E-02	7.73E-03	2.78E+00	1.69E-01	2.45E+02
C_{33}	5.82E-03	8.35E-05	-5.36E-01	-5.95E-02	1.87E-02	6.16E+00	4.33E-01	5.84E+02
C_{23}	-2.02E-03	2.76E-04	1.72E-01	-2.06E-02	1.35E-02	4.69E+00	3.35E-01	4.21E+02
C_{66}	1.32E-03	-1.16E-05	-2.15E-01	-1.85E-02	1.29E-02	4.25E+00	3.02E-01	3.71E+02
$(Mg_{1-x}Fe_x)(Si_{1-x}Al_x)O_3$ Pv								
C_{11}	9.76E-04	-1.92E-04	-2.44E-01	-1.31E-02	1.83E-02	5.57E+00	4.21E-01	5.26E+02
C_{12}	3.77E-03	-3.09E-05	-4.08E-01	-5.51E-03	1.39E-02	4.22E+00	3.37E-01	3.95E+02
C_{44}	1.43E-03	2.34E-05	-1.98E-01	-2.33E-02	1.02E-02	3.47E+00	2.33E-01	3.32E+02
C_{22}	-3.59E-03	4.34E-04	1.37E-01	-8.49E-02	1.75E-02	5.58E+00	4.28E-01	5.17E+02
C_{13}	1.84E-03	-2.07E-04	-1.68E-01	2.28E-02	1.38E-02	4.01E+00	3.21E-01	3.72E+02
C_{55}	-1.88E-03	1.52E-04	7.30E-02	-2.09E-02	7.60E-03	2.48E+00	1.65E-01	2.42E+02
C_{33}	3.01E-03	1.41E-04	-3.74E-01	-6.29E-02	1.87E-02	5.61E+00	4.33E-01	5.24E+02
C_{23}	-3.81E-03	2.81E-04	3.18E-01	-1.82E-02	1.35E-02	4.35E+00	3.34E-01	3.85E+02
C_{66}	-7.65E-04	-5.80E-05	2.04E-02	-1.57E-02	1.27E-02	3.99E+00	2.98E-01	3.59E+02
$(Mg_{1-x}Fe_x)(Si_{1-x}Fe_x)O_3$ pPv								
C_{11}	9.31E-03	-7.98E-04	-1.28E+00	7.05E-02	4.35E-02	8.69E+00	7.61E-01	1.08E+03
C_{12}	-4.70E-03	2.67E-04	4.16E-01	-2.33E-02	3.29E-02	6.44E+00	5.73E-01	8.11E+02
C_{44}	4.34E-03	-3.71E-05	-5.63E-01	-7.15E-03	2.78E-02	7.24E+00	4.95E-01	9.03E+02
C_{22}	-4.70E-03	5.31E-04	5.06E-01	-9.89E-02	4.30E-02	7.34E+00	7.76E-01	9.09E+02
C_{13}	5.05E-03	-6.66E-04	-6.16E-01	7.50E-02	3.12E-02	6.02E+00	5.46E-01	7.50E+02
C_{55}	-4.16E-03	2.23E-04	4.94E-01	-4.51E-02	2.21E-02	3.90E+00	3.59E-01	4.87E+02
C_{33}	-4.64E-03	3.79E-04	3.43E-01	-7.71E-02	4.40E-02	7.05E+00	7.16E-01	8.94E+02
C_{23}	-5.86E-03	6.41E-04	6.95E-01	-8.29E-02	3.28E-02	5.61E+00	5.68E-01	6.90E+02
C_{66}	-1.47E-03	-6.14E-05	8.75E-02	-1.70E-02	2.99E-02	5.27E+00	4.96E-01	6.74E+02
$(Mg_{1-x}Fe_x)(Si_{1-x}Al_x)O_3$ pPv								
C_{11}	3.70E-03	-6.37E-04	-5.92E-01	5.05E-02	4.22E-02	7.12E+00	7.41E-01	9.10E+02
C_{12}	-5.42E-03	4.62E-04	6.28E-01	-5.18E-02	3.13E-02	5.31E+00	5.51E-01	6.59E+02
C_{44}	3.72E-04	-1.39E-04	-1.23E-02	1.60E-03	2.67E-02	4.65E+00	4.79E-01	5.89E+02
C_{22}	-3.69E-03	4.45E-04	4.03E-01	-8.90E-02	4.18E-02	7.98E+00	7.48E-01	1.00E+03
C_{13}	8.26E-03	-7.81E-04	-8.94E-01	8.64E-02	3.01E-02	4.90E+00	5.30E-01	6.25E+02
C_{55}	-8.33E-04	6.38E-05	1.01E-01	-2.46E-02	2.22E-02	3.94E+00	3.60E-01	5.09E+02
C_{33}	-2.40E-03	8.96E-04	1.79E-01	-1.46E-01	4.34E-02	7.64E+00	7.06E-01	9.64E+02
C_{23}	-2.12E-03	4.01E-04	2.99E-01	-4.93E-02	3.25E-02	5.97E+00	5.68E-01	7.41E+02
C_{66}	2.80E-03	-9.25E-06	-4.08E-01	-2.23E-02	2.95E-02	5.28E+00	4.95E-01	6.73E+02

Table 3.13: Density and adiabatic elastic and seismic properties for Fe^{2+}-bearing Pv and pPv at different P, T conditions. The values in parenthesis denote the error.

T[K]	2000	4000	2000	4000
P[GPa]	100	100	136	136
$(Mg_{0.75}Fe_{0.25})SiO_3$ Pv				
ρ [kg/m^3]	5532	5375	5857	5717
C_{11}[GPa]	822.44(5.24)	720.84(10.79)	940.29(9.03)	894.72(13.27)
C_{22}[GPa]	980.51(9.62)	849.01(15.85)	1151.59(7.65)	1020.73(14.10)
C_{33}[GPa]	941.25(9.94)	827.20(23.95)	1137.57(8.82)	1039.02(20.41)
C_{12}[GPa]	485.55(6.59)	451.07(13.69)	608.64(5.95)	618.63(10.31)
C_{13}[GPa]	399.96(7.71)	411.66(15.42)	489.99(6.78)	475.96(16.25)
C_{23}[GPa]	438.51(7.20)	425.31(11.32)	532.45(8.07)	531.07(9.76)
C_{44}[GPa]	291.27(3.62)	241.62(0.69)	327.59(3.34)	280.81(9.62)
C_{55}[GPa]	236.50(4.30)	213.65(3.93)	258.31(2.17)	241.40(5.85)
C_{66}[GPa]	241.19(8.20)	218.16(14.42)	307.84(9.06)	245.27(11.85)
K^S[GPa]	599.14(3.22)	552.57(6.24)	721.29(3.15)	689.53(5.72)
G[GPa]	248.47(2.37)	208.62(3.95)	285.31(2.35)	242.08(4.03)
V_ϕ[km/s]	10.41(0.03)	10.14(0.06)	11.10(0.02)	10.98(0.05)
V_s[km/s]	6.70(0.03)	6.23(0.06)	6.98(0.03)	6.51(0.05)
V_p[km/s]	12.97(0.03)	12.43(0.06)	13.71(0.03)	13.31(0.05)
$(Mg_{0.75}Fe_{0.25})SiO_3$ pPv				
ρ [kg/m^3]	5614	5454	5945	5800
C_{11}[GPa]	1071.27(4.81)	999.04(16.22)	1250.32(8.97)	1166.04(12.87)
C_{22}[GPa]	820.66(4.40)	765.46(11.81)	973.85(5.40)	874.94(12.25)
C_{33}[GPa]	1055.93(7.48)	946.37(13.96)	1276.18(11.76)	1135.09(20.23)
C_{12}[GPa]	398.56(6.17)	413.88(18.63)	529.23(7.49)	515.19(16.74)
C_{13}[GPa]	344.47(7.04)	339.45(17.38)	407.95(11.61)	417.84(14.29)
C_{23}[GPa]	443.23(6.29)	431.01(10.83)	550.59(5.01)	541.41(11.94)
C_{44}[GPa]	218.69(5.21)	197.70(18.36)	266.10(6.82)	238.97(9.00)
C_{55}[GPa]	212.15(3.64)	180.59(7.17)	249.92(3.38)	212.20(5.61)
C_{66}[GPa]	300.23(6.68)	276.82(11.35)	388.37(5.87)	325.26(9.51)
K^S[GPa]	591.15(2.74)	564.39(6.72)	719.54(3.70)	680.55(6.32)
G[GPa]	263.65(2.10)	232.79(5.17)	315.05(2.40)	268.73(3.76)
V_ϕ[km/s]	10.26(0.02)	10.17(0.06)	11.00(0.03)	10.83(0.05)
V_s[km/s]	6.85(0.03)	6.53(0.07)	7.28(0.03)	6.81(0.05)
V_p[km/s]	12.96(0.03)	12.66(0.07)	13.85(0.03)	13.38(0.05)

Table 3.14: Density and adiabatic elastic and seismic properties for pure and Fe^{3+}-bearing (including Fe^{3+}-Fe^{3+} and Fe^{3+}-Al^{3+} charge-coupled substitution) Pv and pPv at different P, T conditions. The values in parenthesis denote the error.

$MgSiO_3$ Pv				
T[K]	1500	1500	1500	1500
P[GPa]	50.08(0.03)	75.02(0.03)	100.30(0.04)	125.32(0.05)
ρ[kg/m^3]	4706.94	4974.97	5215.67	5432.38
C_{11}[GPa]	646.78(8.82)	723.06(8.48)	857.03(14.61)	929.18(11.61)
C_{22}[GPa]	798.75(12.16)	922.94(13.15)	1032.29(9.69)	1136.20(12.21)
C_{33}[GPa]	735.20(10.11)	862.04(12.31)	1016.04(15.32)	1115.94(11.82)
C_{12}[GPa]	283.45(13.66)	410.46(12.77)	481.72(14.83)	545.63(15.99)
C_{13}[GPa]	291.25(11.23)	398.89(8.16)	501.57(9.12)	561.21(11.34)
C_{23}[GPa]	273.36(13.15)	300.49(11.37)	341.05(8.08)	441.56(14.05)
C_{44}[GPa]	244.84(9.95)	322.43(8.65)	366.74(12.70)	418.55(11.26)
C_{55}[GPa]	291.45(9.54)	336.82(11.08)	381.93(11.01)	465.45(14.71)
C_{66}[GPa]	286.64(10.13)	357.96(13.69)	373.16(13.95)	476.55(18.04)
K^S[GPa]	427.97(3.70)	515.01(3.75)	594.61(4.14)	676.70(4.55)
G[GPa]	226.12(2.55)	244.69(2.57)	286.67(2.70)	303.55(2.83)
V_ϕ[km/s]	9.54(0.04)	10.17(0.04)	10.68(0.04)	11.16(0.04)
V_s[km/s]	6.93(0.04)	7.01(0.04)	7.41(0.03)	7.48(0.03)
V_p[km/s]	12.45(0.04)	13.00(0.04)	13.69(0.04)	14.11(0.04)
$(Mg_{0.9375}Fe_{0.0625})(Si_{0.9375}Fe_{0.0625})O_3$ Pv				
T[K]	1500	1500	1500	1500
P[GPa]	50.20(0.04)	75.14(0.04)	100.08(0.03)	125.11(0.04)
ρ[kg/m^3]	4851.87	5143.06	5389.24	5612.76
C_{11}[GPa]	632.79(14.00)	739.63(11.23)	815.08(13.95)	904.64(14.68)
C_{22}[GPa]	787.95(13.95)	918.06(10.94)	997.02(14.27)	1180.78(14.90)
C_{33}[GPa]	757.36(13.18)	862.35(14.85)	1003.68(13.00)	1106.79(15.76)
C_{12}[GPa]	308.59(16.01)	404.31(11.45)	433.09(14.00)	585.26(11.91)
C_{13}[GPa]	298.37(14.15)	401.21(11.67)	498.27(11.91)	559.41(13.09)
C_{23}[GPa]	274.46(13.40)	292.74(12.09)	401.63(12.58)	453.54(13.21)
C_{44}[GPa]	228.02(11.52)	322.27(11.01)	383.02(11.46)	443.23(12.21)
C_{55}[GPa]	274.32(14.19)	327.50(12.54)	423.78(13.57)	459.22(13.20)
C_{66}[GPa]	276.22(16.28)	346.56(9.07)	415.23(10.28)	474.37(17.19)
K^S[GPa]	426.45(4.71)	512.74(3.91)	596.76(4.28)	685.25(4.70)
G[GPa]	222.88(3.51)	238.58(3.17)	266.52(4.26)	297.63(3.37)
V_ϕ[km/s]	9.38(0.05)	9.98(0.04)	10.52(0.04)	11.05(0.04)
V_s[km/s]	6.78(0.05)	6.81(0.05)	7.03(0.06)	7.28(0.04)
V_p[km/s]	12.21(0.06)	12.71(0.04)	13.29(0.05)	13.88(0.04)
$(Mg_{0.9375}Fe_{0.0625})(Si_{0.9375}Al_{0.0625})O_3$ Pv				
T[K]	1500	1500	1500	1500
P[GPa]	50.39(0.02)	73.62(0.04)	100.16(0.04)	125.21(0.03)
ρ[kg/m^3]	4773.83	5030.29	5287.08	5519.89
C_{11}[GPa]	632.00(15.77)	735.47(10.95)	856.50(14.32)	915.74(12.87)
C_{22}[GPa]	772.50(12.03)	866.54(12.76)	1023.47(14.17)	1166.22(9.21)
C_{33}[GPa]	743.78(16.42)	897.78(12.74)	1014.95(14.06)	1107.89(15.78)

Table 3.14: ... continued

C_{12}[GPa]	300.82(12.22)	405.15(12.67)	450.27(16.45)	575.72(14.16)
C_{13}[GPa]	313.48(11.41)	403.38(15.73)	485.14(17.31)	555.85(13.70)
C_{23}[GPa]	265.76(11.52)	299.59(12.32)	391.25(10.98)	423.75(10.29)
C_{44}[GPa]	245.99(11.81)	322.43(12.92)	392.60(15.68)	428.18(15.50)
C_{55}[GPa]	273.30(18.31)	367.47(13.76)	429.21(14.26)	469.24(10.00)
C_{66}[GPa]	266.26(15.26)	315.35(12.06)	396.90(15.70)	460.61(17.59)
K^S[GPa]	423.77(4.69)	512.57(4.31)	604.48(4.96)	678.13(4.50)
G[GPa]	227.10(3.40)	247.28(3.44)	277.90(3.82)	308.29(2.92)
V_ϕ[km/s]	9.42(0.05)	10.09(0.04)	10.69(0.04)	11.08(0.04)
V_s[km/s]	6.90(0.05)	7.01(0.05)	7.25(0.05)	7.47(0.04)
V_p[km/s]	12.34(0.06)	12.94(0.05)	13.58(0.05)	14.05(0.04)
$(Mg_{0.875}Fe_{0.125})(Si_{0.875}Fe_{0.125})O_3$ Pv				
T[K]	1500	1500	1500	1500
P[GPa]	50.36(0.04)	75.24(0.16)	100.12(0.06)	125.13(0.07)
ρ[kg/m^3]	4996.67	5301.1	5540.05	5788.89
C_{11}[GPa]	628.31(15.04)	745.96(30.77)	806.10(13.54)	907.56(19.95)
C_{22}[GPa]	751.13(18.12)	834.29(24.96)	1030.82(13.73)	1150.46(20.46)
C_{33}[GPa]	718.23(17.42)	835.13(21.15)	980.87(12.61)	1120.00(11.92)
C_{12}[GPa]	314.94(15.38)	448.94(21.50)	515.07(13.44)	566.58(20.69)
C_{13}[GPa]	329.45(14.38)	373.00(24.12)	502.02(16.76)	559.05(15.30)
C_{23}[GPa]	284.91(14.64)	355.31(25.67)	379.73(13.43)	468.40(21.63)
C_{44}[GPa]	265.80(11.23)	328.20(26.74)	371.91(11.83)	446.50(19.61)
C_{55}[GPa]	286.64(14.38)	327.19(20.96)	394.73(13.83)	482.25(17.70)
C_{66}[GPa]	308.51(17.71)	381.41(24.79)	399.01(13.03)	434.23(17.05)
K^S[GPa]	431.99(5.17)	514.38(8.23)	597.81(4.55)	681.67(6.16)
G[GPa]	201.62(3.63)	228.55(5.24)	259.32(3.74)	285.89(5.44)
V_ϕ[km/s]	9.30(0.06)	9.85(0.08)	10.39(0.04)	10.85(0.05)
V_s[km/s]	6.35(0.06)	6.57(0.08)	6.84(0.05)	7.03(0.07)
V_p[km/s]	11.84(0.06)	12.43(0.08)	13.05(0.05)	13.55(0.06)
$(Mg_{0.875}Fe_{0.125})(Si_{0.875}Al_{0.125})O_3$ Pv				
T[K]	1500	1500	1500	1500
P[GPa]	50.26(0.04)	75.16(0.04)	100.26(0.04)	125.46(0.02)
ρ[kg/m^3]	4854	5142.8	5390.32	5614.15
C_{11}[GPa]	621.95(15.39)	742.58(15.52)	845.29(13.09)	922.05(10.78)
C_{22}[GPa]	749.58(13.04)	923.52(9.98)	1090.71(15.04)	1146.84(12.24)
C_{33}[GPa]	697.18(14.55)	887.18(13.49)	1004.63(14.81)	1108.16(11.66)
C_{12}[GPa]	311.39(12.85)	396.00(12.75)	495.39(12.48)	565.92(11.64)
C_{13}[GPa]	316.10(14.60)	387.98(15.02)	480.54(13.36)	547.25(12.07)
C_{23}[GPa]	280.90(12.35)	332.83(14.73)	341.62(14.65)	459.37(10.53)
C_{44}[GPa]	261.29(12.66)	294.61(10.72)	364.49(10.32)	433.79(12.31)
C_{55}[GPa]	279.79(13.69)	298.36(13.57)	388.43(13.53)	487.87(14.25)
C_{66}[GPa]	301.20(14.39)	333.05(11.67)	428.33(15.05)	465.56(17.80)
K^S[GPa]	424.38(4.59)	510.68(4.39)	604.38(4.56)	681.87(4.25)
G[GPa]	202.77(3.71)	243.25(4.01)	277.80(3.67)	294.10(3.48)
V_ϕ[km/s]	9.35(0.05)	9.96(0.04)	10.59(0.04)	11.02(0.03)
V_s[km/s]	6.46(0.06)	6.88(0.06)	7.18(0.05)	7.24(0.04)

Table 3.14: ... continued

V_p[km/s]	11.96(0.06)	12.74(0.05)	13.45(0.05)	13.83(0.04)
$MgSiO_3$ Pv				
T[K]	2500	2500	2500	2500
P[GPa]	50.04(0.06)	75.09(0.06)	100.32(0.05)	125.49(0.03)
ρ[kg/m^3]	4615.37	4896.87	5145.41	5367.44
C_{11}[GPa]	632.58(19.62)	720.33(13.87)	829.78(16.14)	875.53(12.19)
C_{22}[GPa]	703.30(12.91)	866.15(16.61)	1014.62(21.39)	1111.45(20.67)
C_{33}[GPa]	716.11(16.22)	820.97(16.78)	953.82(19.09)	1116.92(20.77)
C_{12}[GPa]	257.25(21.47)	408.69(18.05)	457.18(20.05)	590.25(20.07)
C_{13}[GPa]	280.73(16.21)	392.70(14.08)	496.14(16.25)	544.32(15.95)
C_{23}[GPa]	260.36(21.71)	306.15(16.66)	390.81(19.55)	388.61(17.34)
C_{44}[GPa]	244.99(20.09)	306.15(15.60)	342.09(16.70)	443.08(18.80)
C_{55}[GPa]	271.36(21.77)	328.80(15.26)	412.52(19.10)	518.29(14.12)
C_{66}[GPa]	262.52(15.99)	371.07(18.17)	417.77(18.37)	470.80(17.69)
K^S[GPa]	403.24(6.23)	502.33(5.40)	590.53(6.20)	673.25(5.91)
G[GPa]	208.35(3.89)	237.54(4.02)	264.35(4.03)	287.89(5.24)
V_ϕ[km/s]	9.35(0.07)	10.13(0.05)	10.71(0.06)	11.20(0.05)
V_s[km/s]	6.72(0.06)	6.96(0.06)	7.17(0.05)	7.32(0.07)
V_p[km/s]	12.15(0.07)	12.93(0.06)	13.54(0.06)	14.03(0.06)
$(Mg_{0.9375}Fe_{0.0625})(Si_{0.9375}Fe_{0.0625})O_3$ Pv				
T[K]	2500	2500	2500	2500
P[GPa]	49.68(0.08)	74.96(0.08)	100.06(0.06)	125.01(0.04)
ρ[kg/m^3]	4750.36	5049.97	5314.12	5541.16
C_{11}[GPa]	602.54(20.38)	649.82(20.68)	789.43(19.57)	888.09(25.05)
C_{22}[GPa]	711.20(20.23)	817.23(27.66)	946.30(24.19)	1104.82(17.70)
C_{33}[GPa]	650.80(21.71)	810.36(23.91)	915.89(18.70)	1082.86(20.24)
C_{12}[GPa]	283.16(18.94)	401.80(21.18)	493.15(17.38)	536.61(21.04)
C_{13}[GPa]	314.70(21.59)	391.74(27.61)	510.88(21.91)	559.35(17.58)
C_{23}[GPa]	262.85(22.69)	310.95(20.09)	395.72(23.97)	420.69(23.11)
C_{44}[GPa]	246.83(24.15)	330.92(16.02)	399.07(22.72)	437.03(19.79)
C_{55}[GPa]	273.89(14.78)	354.14(23.66)	463.49(24.35)	465.21(17.77)
C_{66}[GPa]	283.08(20.91)	369.10(20.73)	396.21(21.55)	482.43(18.39)
K^S[GPa]	403.23(6.92)	492.90(7.56)	590.02(7.24)	664.12(6.74)
G[GPa]	189.74(5.76)	204.48(5.58)	237.83(6.04)	284.70(5.91)
V_ϕ[km/s]	9.21(0.08)	9.88(0.08)	10.54(0.06)	10.95(0.06)
V_s[km/s]	6.32(0.10)	6.36(0.09)	6.69(0.09)	7.17(0.07)
V_p[km/s]	11.75(0.09)	12.31(0.09)	13.07(0.08)	13.72(0.07)
$(Mg_{0.9375}Fe_{0.0625})(Si_{0.9375}Al_{0.0625})O_3$ Pv				
T[K]	2500	2500	2500	2500
P[GPa]	49.97(0.04)	74.86(0.05)	100.24(0.05)	125.16(0.04)
ρ[kg/m^3]	4676.67	4961.48	5215.04	5451.29
C_{11}[GPa]	624.34(20.22)	714.98(19.27)	808.86(32.62)	873.84(18.86)
C_{22}[GPa]	688.27(12.85)	814.52(13.01)	1002.60(24.76)	1089.48(19.93)
C_{33}[GPa]	632.57(19.60)	843.17(21.77)	998.35(25.68)	1046.08(21.23)
C_{12}[GPa]	298.93(18.36)	345.56(20.39)	432.54(20.41)	537.41(21.93)

Table 3.14: ... continued

C_{13}[GPa]	293.58(13.21)	363.95(18.52)	452.47(24.49)	545.92(19.73)
C_{23}[GPa]	252.51(15.17)	326.72(22.74)	398.99(24.54)	404.28(21.15)
C_{44}[GPa]	274.98(18.58)	308.48(19.73)	395.63(34.08)	428.45(18.27)
C_{55}[GPa]	269.56(21.50)	366.32(15.84)	385.39(27.34)	467.13(26.14)
C_{66}[GPa]	288.78(13.58)	331.05(18.12)	416.29(21.79)	498.94(21.32)
K^S[GPa]	402.61(5.76)	490.53(6.34)	587.90(8.85)	654.61(7.02)
G[GPa]	200.00(4.16)	232.19(4.45)	257.74(6.66)	270.29(5.63)
V_ϕ[km/s]	9.28(0.07)	9.94(0.06)	10.62(0.08)	10.96(0.06)
V_s[km/s]	6.54(0.07)	6.84(0.07)	7.03(0.09)	7.04(0.07)
V_p[km/s]	11.96(0.07)	12.70(0.07)	13.37(0.09)	13.65(0.07)
$(Mg_{0.875}Fe_{0.125})(Si_{0.875}Fe_{0.125})O_3$ Pv				
T[K]	2500	2500	2500	2500
P[GPa]	49.82(0.04)	75.22(0.07)	100.13(0.08)	125.13(0.08)
ρ[kg/m^3]	4891.41	5209.39	5455.12	5712.86
C_{11}[GPa]	582.66(19.97)	698.21(20.97)	783.71(16.24)	839.91(22.91)
C_{22}[GPa]	677.29(26.16)	825.04(21.48)	971.64(20.57)	1099.77(30.52)
C_{33}[GPa]	619.79(19.59)	828.75(30.57)	940.39(22.98)	1123.08(28.49)
C_{12}[GPa]	272.55(18.20)	408.17(24.81)	534.65(20.86)	569.43(29.50)
C_{13}[GPa]	288.77(17.12)	418.54(21.34)	524.59(18.85)	595.27(16.93)
C_{23}[GPa]	270.75(19.63)	324.72(20.76)	353.10(17.86)	471.40(21.72)
C_{44}[GPa]	254.38(15.81)	366.97(29.92)	373.35(18.76)	445.63(17.40)
C_{55}[GPa]	306.04(24.47)	368.21(23.52)	395.13(24.34)	499.53(24.44)
C_{66}[GPa]	351.24(26.52)	350.98(23.80)	401.10(21.89)	458.13(17.37)
K^S[GPa]	402.61(7.05)	509.95(8.13)	586.41(6.80)	678.02(7.93)
G[GPa]	184.05(5.51)	207.18(6.03)	245.43(5.12)	265.65(7.49)
V_ϕ[km/s]	9.07(0.08)	9.89(0.08)	10.37(0.06)	10.89(0.06)
V_s[km/s]	6.13(0.09)	6.31(0.09)	6.71(0.07)	6.82(0.10)
V_p[km/s]	11.51(0.09)	12.28(0.09)	12.94(0.07)	13.44(0.08)
$(Mg_{0.875}Fe_{0.125})(Si_{0.875}Al_{0.125})O_3$ Pv				
T[K]	2500	2500	2500	2500
P[GPa]	50.09(0.08)	75.21(0.08)	100.14(0.06)	125.23(0.06)
ρ[kg/m^3]	4760.03	5059.39	5313.32	5543.83
C_{11}[GPa]	596.29(24.70)	678.04(28.16)	803.04(18.82)	865.70(20.10)
C_{22}[GPa]	696.45(22.59)	847.97(20.45)	982.63(18.89)	1058.37(23.43)
C_{33}[GPa]	679.16(22.73)	779.05(18.08)	940.23(20.07)	1034.42(27.68)
C_{12}[GPa]	297.10(23.76)	395.61(20.01)	443.25(17.91)	573.96(19.07)
C_{13}[GPa]	294.13(24.08)	342.70(24.97)	437.92(22.12)	580.67(16.54)
C_{23}[GPa]	235.57(22.00)	288.66(19.88)	376.50(16.96)	432.17(20.47)
C_{44}[GPa]	240.03(20.87)	321.39(19.50)	404.41(22.77)	469.83(25.90)
C_{55}[GPa]	263.89(23.44)	404.95(21.75)	400.47(19.32)	487.54(15.49)
C_{66}[GPa]	305.18(17.93)	348.92(15.80)	368.27(26.65)	414.98(26.21)
K^S[GPa]	400.87(7.51)	489.70(7.08)	572.97(6.86)	657.52(7.35)
G[GPa]	183.60(5.52)	217.51(5.75)	248.41(6.67)	263.44(5.49)
V_ϕ[km/s]	9.18(0.09)	9.84(0.07)	10.38(0.06)	10.89(0.06)
V_s[km/s]	6.21(0.09)	6.56(0.09)	6.84(0.09)	6.89(0.07)
V_p[km/s]	11.65(0.09)	12.41(0.08)	13.05(0.08)	13.49(0.07)

Table 3.14: ... continued

$MgSiO_3$ Pv				
T[K]	3500	3500	3500	3500
P[GPa]	49.92(0.09)	75.18(0.06)	100.17(0.07)	125.12(0.07)
ρ[kg/m^3]	4516.84	4813.98	5070.98	5297.55
C_{11}[GPa]	580.02(25.15)	664.27(29.34)	749.74(20.86)	867.87(24.69)
C_{22}[GPa]	682.47(20.55)	812.15(26.19)	1016.36(24.01)	1053.43(19.27)
C_{33}[GPa]	630.52(26.65)	756.52(23.35)	877.48(18.16)	1049.31(20.06)
C_{12}[GPa]	286.38(25.54)	386.13(24.33)	469.10(22.70)	508.01(30.41)
C_{13}[GPa]	302.10(24.57)	419.32(21.31)	482.75(20.93)	542.39(18.21)
C_{23}[GPa]	288.40(27.79)	282.01(28.75)	383.49(23.81)	436.23(23.87)
C_{44}[GPa]	284.64(23.35)	309.84(21.78)	383.37(21.83)	406.93(24.33)
C_{55}[GPa]	237.67(23.27)	319.89(25.80)	417.31(27.47)	462.96(19.50)
C_{66}[GPa]	308.18(26.72)	360.07(19.72)	400.76(18.76)	496.36(26.10)
K^S[GPa]	400.04(8.31)	478.91(8.24)	575.60(7.41)	647.05(7.75)
G[GPa]	179.64(5.97)	214.00(5.73)	245.36(4.87)	279.71(5.64)
V_ϕ[km/s]	9.41(0.10)	9.97(0.09)	10.65(0.07)	11.05(0.07)
V_s[km/s]	6.31(0.10)	6.67(0.09)	6.96(0.07)	7.27(0.07)
V_p[km/s]	11.90(0.11)	12.60(0.09)	13.34(0.07)	13.88(0.07)
$(Mg_{0.9375}Fe_{0.0625})(Si_{0.9375}Fe_{0.0625})O_3$ Pv				
T[K]	3500	3500	3500	3500
P[GPa]	49.68(0.10)	74.96(0.09)	100.00(0.07)	124.78(0.08)
ρ[kg/m^3]	4655.62	4971.69	5236.83	5468.84
C_{11}[GPa]	556.33(35.00)	676.60(28.53)	755.12(26.19)	851.33(37.72)
C_{22}[GPa]	633.47(23.76)	780.83(33.20)	963.07(25.70)	1051.27(28.67)
C_{33}[GPa]	613.34(29.09)	708.72(25.84)	866.38(32.14)	993.09(30.47)
C_{12}[GPa]	303.64(25.14)	393.13(21.50)	471.43(23.96)	594.82(30.38)
C_{13}[GPa]	300.74(32.75)	437.90(35.96)	533.71(22.98)	599.86(31.67)
C_{23}[GPa]	247.37(37.55)	333.30(25.28)	359.52(21.14)	445.12(35.26)
C_{44}[GPa]	200.71(32.99)	349.84(25.91)	373.86(24.23)	463.43(24.40)
C_{55}[GPa]	274.47(33.85)	368.27(29.89)	393.13(26.60)	471.54(31.48)
C_{66}[GPa]	268.71(27.84)	381.37(28.62)	391.18(22.22)	461.54(26.14)
K^S[GPa]	377.64(10.40)	492.22(9.53)	567.49(8.40)	659.11(10.31)
G[GPa]	162.15(9.34)	203.71(7.89)	225.79(7.04)	261.88(7.09)
V_ϕ[km/s]	9.01(0.12)	9.95(0.10)	10.41(0.08)	10.98(0.09)
V_s[km/s]	5.90(0.17)	6.40(0.12)	6.57(0.10)	6.92(0.09)
V_p[km/s]	11.29(0.15)	12.39(0.12)	12.88(0.09)	13.58(0.09)
$(Mg_{0.9375}Fe_{0.0625})(Si_{0.9375}Al_{0.0625})O_3$ Pv				
T[K]	3500	3500	3500	3500
P[GPa]	49.57(0.07)	74.91(0.07)	99.77(0.12)	124.95(0.07)
ρ[kg/m^3]	4572.98	4878.1	5135.58	5380.28
C_{11}[GPa]	546.94(27.00)	693.59(30.40)	723.35(38.01)	862.64(23.53)
C_{22}[GPa]	652.15(24.37)	740.53(20.48)	903.56(35.81)	1081.38(37.01)
C_{33}[GPa]	593.11(32.69)	761.17(23.18)	881.75(38.34)	1011.29(26.02)
C_{12}[GPa]	253.28(25.35)	343.84(28.04)	463.77(31.99)	542.44(21.33)
C_{13}[GPa]	185.94(32.99)	352.95(22.52)	460.52(36.88)	586.89(25.83)

Table 3.14: ... continued

C_{23}[GPa]	268.20(29.83)	369.16(31.55)	399.88(36.20)	421.64(26.49)
C_{44}[GPa]	343.81(27.17)	325.42(29.91)	426.85(28.95)	390.99(28.34)
C_{55}[GPa]	315.34(30.66)	434.05(28.22)	448.96(31.35)	427.38(32.13)
C_{66}[GPa]	314.64(24.54)	321.01(26.07)	508.82(33.89)	460.62(27.44)
K^S[GPa]	385.93(9.49)	482.41(8.99)	579.72(11.58)	642.81(9.30)
G[GPa]	167.54(7.50)	204.89(6.68)	216.64(7.77)	263.44(6.38)
V_ϕ[km/s]	9.19(0.11)	9.94(0.09)	10.62(0.11)	10.93(0.08)
V_s[km/s]	6.05(0.14)	6.48(0.11)	6.50(0.12)	7.00(0.08)
V_p[km/s]	11.54(0.13)	12.45(0.10)	13.00(0.12)	13.59(0.09)
$(Mg_{0.875}Fe_{0.125})(Si_{0.875}Fe_{0.125})O_3$ Pv				
T[K]	3500	3500	3500	3500
P[GPa]	50.10(0.11)	75.08(0.06)	100.03(0.11	125.00(0.10)
ρ[kg/m^3]	4787.9	5120.2	5375.36	5637.85
C_{11}[GPa]	479.60(27.73)	707.12(39.15)	749.24(32.54)	848.23(29.37)
C_{22}[GPa]	659.28(29.65)	784.03(26.87)	912.04(30.22)	1014.48(37.24)
C_{33}[GPa]	535.29(30.76)	776.28(37.01)	908.36(24.28)	1062.83(38.47)
C_{12}[GPa]	312.01(28.82)	368.37(27.14)	446.25(37.68)	488.60(33.88)
C_{13}[GPa]	279.72(31.80)	311.09(35.58)	482.93(36.80)	632.99(31.67)
C_{23}[GPa]	265.05(28.58)	289.79(38.65)	358.71(26.65)	417.27(30.11)
C_{44}[GPa]	229.23(33.74)	353.20(36.63)	366.91(26.47)	435.33(26.93)
C_{55}[GPa]	228.97(28.92)	404.19(38.68)	414.99(24.04)	510.29(35.71)
C_{66}[GPa]	303.34(31.10)	336.06(26.78)	393.02(31.58)	432.06(31.87)
K^S[GPa]	365.83(10.06)	481.13(11.48)	559.16(10.14)	649.12(11.00)
G[GPa]	152.30(7.99)	195.22(7.99)	213.49(8.01	248.00(8.31)
V_ϕ[km/s]	8.74(0.12)	9.69(0.12)	10.20(0.09)	10.73(0.09)
V_s[km/s]	5.64(0.15)	6.17(0.13)	6.30(0.12)	6.63(0.11)
V_p[km/s]	10.90(0.14)	12.03(0.13)	12.53(0.11)	13.18(0.11)
$(Mg_{0.875}Fe_{0.125})(Si_{0.875}Al_{0.125})O_3$ Pv				
T[K]	3500	3500	3500	3500
P[GPa]	48.90(0.08)	75.11(0.09)	99.72(0.10)	124.70(0.09)
ρ[kg/m^3]	4643.36	4971.34	5233.8	5468.79
C_{11}[GPa]	521.53(29.86)	626.22(39.05)	759.15(32.46)	801.48(21.71)
C_{22}[GPa]	627.32(27.53)	799.79(32.32)	894.89(28.82)	1055.96(25.54)
C_{33}[GPa]	565.33(26.77)	701.01(27.01)	882.18(27.67)	1051.88(26.03)
C_{12}[GPa]	251.58(25.93)	384.15(41.19)	459.62(32.02)	583.30(21.46)
C_{13}[GPa]	279.94(36.30)	381.99(36.98)	437.80(24.41)	537.24(24.48)
C_{23}[GPa]	264.44(29.46)	347.60(30.16)	362.76(28.57)	409.91(21.34)
C_{44}[GPa]	237.01(25.58)	305.78(37.40)	441.66(29.95)	448.91(28.53)
C_{55}[GPa]	229.83(28.14)	377.88(27.96)	405.52(26.48)	500.97(25.43)
C_{66}[GPa]	241.94(29.40)	392.62(23.81)	349.30(23.04)	441.06(25.55)
K^S[GPa]	357.66(9.64)	479.67(11.12)	554.76(9.44)	647.86(8.19)
G[GPa]	149.80(7.26)	197.68(9.03)	219.58(6.77)	253.19(5.99)
V_ϕ[km/s]	8.78(0.12)	9.82(0.11)	10.30(0.09)	10.88(0.07)
V_s[km/s]	5.68(0.14)	6.31(0.14)	6.48(0.10)	6.80(0.08)
V_p[km/s]	10.96(0.13)	12.23(0.13)	12.73(0.10)	13.42(0.08)

Table 3.14: ... continued

$MgSiO_3$ pPv			
T[K]	1500	1500	1500
P[GPa]	99.95(0.05)	124.85(0.04)	150.01(0.05)
ρ[kg/m^3]	5291.44	5509.75	5710.11
C_{11}[GPa]	1114.60(14.10)	1291.72(13.24)	1405.82(11.56)
C_{22}[GPa]	892.59(13.37)	927.26(16.25)	1034.97(13.53)
C_{33}[GPa]	1123.84(11.80)	1247.10(13.75)	1401.04(9.90)
C_{12}[GPa]	346.93(12.38)	434.42(12.78)	490.07(15.40)
C_{13}[GPa]	358.33(12.32)	454.44(11.51)	494.30(12.39)
C_{23}[GPa]	320.23(14.15)	361.05(16.34)	429.62(12.49)
C_{44}[GPa]	256.10(14.36)	351.29(11.81)	434.87(10.69)
C_{55}[GPa]	467.19(13.22)	532.23(8.38)	607.85(15.78)
C_{66}[GPa]	481.93(11.15)	491.11(10.78)	561.72(10.71)
K^S[GPa]	595.75(4.34)	676.74(4.33)	762.25(4.22)
G[GPa]	300.32(2.98)	331.81(3.13)	370.32(3.11)
V_ϕ[km/s]	10.61(0.04)	11.08(0.04)	11.55(0.03)
V_s[km/s]	7.53(0.04)	7.76(0.04)	8.05(0.03)
V_p[km/s]	13.72(0.04)	14.25(0.04)	14.83(0.03)
$(Mg_{0.917}Fe_{0.083})(Si_{0.917}Fe_{0.083})O_3$ pPv			
T[K]	1500	1500	1500
P[GPa]	100.15(0.07)	125.53(0.06)	149.73(0.03)
ρ[kg/m^3]	5519.15	5748.97	5942.42
C_{11}[GPa]	1087.38(15.43)	1260.12(18.43)	1380.68(11.08)
C_{22}[GPa]	860.66(21.20)	928.14(12.90)	1017.51(14.50)
C_{33}[GPa]	1081.02(14.75)	1250.49(15.01)	1379.75(16.68)
C_{12}[GPa]	434.76(18.14)	490.10(13.44)	571.95(14.37)
C_{13}[GPa]	369.20(16.24)	493.73(16.72)	555.00(11.90)
C_{23}[GPa]	282.37(11.31)	360.06(14.28)	444.36(17.13)
C_{44}[GPa]	300.39(19.69)	375.53(17.11)	408.88(16.01)
C_{55}[GPa]	419.10(16.12)	498.49(12.34)	584.05(13.68)
C_{66}[GPa]	449.43(16.25)	520.68(18.60)	595.59(14.72)
K^S[GPa]	587.15(5.60)	686.37(5.20)	770.86(4.86)
G[GPa]	299.88(6.07)	316.11(5.02)	360.03(4.27)
V_ϕ[km/s]	10.31(0.05)	10.93(0.04)	11.39(0.04)
V_s[km/s]	7.37(0.07)	7.42(0.06)	7.78(0.05)
V_p[km/s]	13.37(0.07)	13.88(0.05)	14.51(0.04)
$(Mg_{0.917}Fe_{0.083})(Si_{0.917}Al_{0.083})O_3$ pPv			
T[K]	1500	1500	1500
P[GPa]	100.30(0.04)	125.04(0.05)	150.04(0.05)
ρ[kg/m^3]	5405.27	5626.76	5816.8
C_{11}[GPa]	1119.59(12.30)	1244.65(14.12)	1359.86(14.28)
C_{22}[GPa]	829.25(13.01)	933.98(14.56)	1034.25(9.80)
C_{33}[GPa]	1129.87(11.99)	1243.07(13.16)	1356.31(14.13)
C_{12}[GPa]	398.87(10.65)	484.04(15.79)	550.94(16.96)
C_{13}[GPa]	388.23(13.34)	431.89(11.48)	535.58(13.41)
C_{23}[GPa]	318.83(16.85)	344.15(16.68)	409.22(13.26)

Table 3.14: ... continued

C_{44}[GPa]	294.30(13.12)	339.50(9.22)	386.29(15.07)
C_{55}[GPa]	420.34(13.88)	498.56(17.67)	574.88(17.91)
C_{66}[GPa]	408.08(15.39)	521.71(18.17)	566.59(15.89)
K^S[GPa]	589.71(4.50)	671.28(4.93)	752.66(4.90)
G[GPa]	292.68(4.83)	336.81(4.99)	356.07(4.52)
V_ϕ[km/s]	10.45(0.04)	10.92(0.04)	11.38(0.04)
V_s[km/s]	7.36(0.06)	7.74(0.06)	7.82(0.05)
V_p[km/s]	13.46(0.05)	14.11(0.05)	14.53(0.05)
$(Mg_{0.833}Fe_{0.167})(Si_{0.833}Fe_{0.167})O_3$ pPv			
T[K]	1500	1500	1500
P[GPa]	100.43(0.07)	124.53(0.06)	150.22(0.07)
ρ[kg/m^3]	5737.79	5965.37	6184.89
C_{11}[GPa]	1089.90(18.93)	1192.59(27.03)	1319.29(26.98)
C_{22}[GPa]	823.02(11.02)	905.14(15.67)	1049.14(17.12)
C_{33}[GPa]	1079.10(14.02)	1223.86(12.91)	1325.01(13.68)
C_{12}[GPa]	409.05(16.87)	504.85(15.18)	620.23(16.13)
C_{13}[GPa]	426.83(29.00)	522.51(23.98)	615.14(27.94)
C_{23}[GPa]	327.01(14.95)	409.70(9.74)	449.86(17.10)
C_{44}[GPa]	365.16(18.40)	428.41(21.35)	499.47(30.79)
C_{55}[GPa]	438.61(14.33)	513.02(12.50)	646.71(12.01)
C_{66}[GPa]	467.79(12.97)	548.43(18.24)	611.01(23.72)
K^S[GPa]	602.94(5.81)	694.28(6.07)	792.87(7.20)
G[GPa]	280.85(5.45)	303.25(5.97)	336.38(6.72)
V_ϕ[km/s]	10.25(0.05)	10.79(0.05)	11.32(0.05)
V_s[km/s]	7.00(0.07)	7.13(0.07)	7.37(0.07)
V_p[km/s]	13.05(0.06)	13.57(0.06)	14.17(0.07)
$(Mg_{0.833}Fe_{0.167})(Si_{0.833}Al_{0.167})O_3$ pPv			
T[K]	1500	1500	1500
P[GPa]	100.25(0.04)	125.33(0.03)	149.52(0.05)
ρ[kg/m^3]	5514.55	5740.97	5919.68
C_{11}[GPa]	1120.08(14.95)	1235.66(11.42)	1399.53(13.67)
C_{22}[GPa]	860.11(13.80)	929.53(12.31)	1040.90(20.15)
C_{33}[GPa]	1066.07(16.45)	1226.26(11.44)	1354.06(18.85)
C_{12}[GPa]	367.84(11.45)	483.16(11.62)	557.98(19.12)
C_{13}[GPa]	396.79(13.27)	479.11(11.42)	557.49(11.15)
C_{23}[GPa]	343.29(15.06)	382.19(12.06)	396.02(13.96)
C_{44}[GPa]	328.01(11.50)	383.17(10.56)	409.60(11.55)
C_{55}[GPa]	435.42(16.73)	510.94(12.53)	556.95(22.80)
C_{66}[GPa]	470.13(17.61)	548.12(11.27)	567.18(22.21)
K^S[GPa]	598.64(4.89)	686.46(3.88)	759.97(5.86)
G[GPa]	287.75(4.12)	318.62(3.21)	359.24(4.05)
V_ϕ[km/s]	10.42(0.04)	10.93(0.03)	11.33(0.04)
V_s[km/s]	7.22(0.05)	7.45(0.04)	7.79(0.04)
V_p[km/s]	13.35(0.05)	13.91(0.04)	14.47(0.05)
$MgSiO_3$ pPv			

Table 3.14: ... continued

T[K]	2500	2500	2500
P[GPa]	99.61(0.05)	124.86(0.04)	149.88(0.05)
ρ[kg/m^3]	5215.05	5443.67	5646.47
C_{11}[GPa]	1101.80(17.39)	1256.74(21.94)	1352.85(17.96)
C_{22}[GPa]	861.10(16.24)	870.78(18.40)	1017.88(24.03)
C_{33}[GPa]	1094.67(20.18)	1214.96(20.81)	1398.90(21.64)
C_{12}[GPa]	326.07(19.13)	406.43(22.39)	523.59(23.61)
C_{13}[GPa]	354.94(16.59)	456.09(15.90)	525.18(17.27)
C_{23}[GPa]	321.92(18.70)	361.88(21.87)	435.41(20.25)
C_{44}[GPa]	270.88(20.01)	333.79(16.21)	403.24(20.29)
C_{55}[GPa]	426.55(17.88)	498.65(22.50)	608.66(19.46)
C_{66}[GPa]	440.51(19.23)	494.59(23.85)	586.41(19.57)
K^S[GPa]	577.60(6.14)	654.88(6.87)	761.35(6.86)
G[GPa]	289.59(5.01)	314.86(5.01)	349.88(5.17)
V_ϕ[km/s]	10.52(0.06)	10.97(0.06)	11.61(0.05)
V_s[km/s]	7.45(0.06)	7.61(0.06)	7.87(0.06)
V_p[km/s]	13.59(0.06)	14.05(0.06)	14.75(0.06)
$(Mg_{0.917}Fe_{0.083})(Si_{0.917}Fe_{0.083})O_3$ pPv			
T[K]	2500	2500	2500
P[GPa]	99.34(0.04)	124.97(0.05)	149.67(0.09)
ρ[kg/m^3]	5434.89	5674.39	5877.31
C_{11}[GPa]	1087.97(16.77)	1223.00(19.56)	1396.51(24.22)
C_{22}[GPa]	777.70(22.32)	887.19(24.20)	1019.09(22.82)
C_{33}[GPa]	1048.00(22.31)	1142.46(22.42)	1349.05(31.49)
C_{12}[GPa]	390.90(19.00)	478.85(17.80)	518.42(23.09)
C_{13}[GPa]	365.07(18.81)	490.98(15.51)	526.41(23.89)
C_{23}[GPa]	273.36(16.63)	357.24(21.62)	374.97(29.58)
C_{44}[GPa]	304.68(18.85)	364.83(22.09)	397.36(20.67)
C_{55}[GPa]	427.78(21.19)	530.32(18.65)	571.23(29.39)
C_{66}[GPa]	450.71(21.91)	533.26(25.03)	606.37(33.03)
K^S[GPa]	569.57(6.62	667.57(6.99)	751.05(8.93)
G[GPa]	271.69(4.80	298.71(5.21)	350.88(7.73)
V_ϕ[km/s]	10.24(0.06)	10.85(0.06)	11.30(0.07)
V_s[km/s]	7.07(0.06)	7.26(0.06)	7.73(0.09)
V_p[km/s]	13.09(0.06)	13.71(0.06)	14.40(0.08)
$(Mg_{0.917}Fe_{0.083})(Si_{0.917}Al_{0.083})O_3$ pPv			
T[K]	2500	2500	2500
P[GPa]	99.73(0.06)	125.35(0.05)	150.55(0.06)
ρ[kg/m^3]	5323.41	5558.32	5768.73
C_{11}[GPa]	1088.04(22.43)	1226.89(19.16)	1344.49(15.84)
C_{22}[GPa]	756.07(18.49)	923.97(24.75)	1001.55(16.38)
C_{33}[GPa]	1043.76(24.10)	1170.67(20.81)	1344.30(14.85)
C_{12}[GPa]	355.68(22.14)	474.74(18.43)	532.04(15.44)
C_{13}[GPa]	367.39(22.82)	466.49(18.61)	573.93(21.24)
C_{23}[GPa]	344.46(16.09)	345.10(20.83)	460.57(20.41)
C_{44}[GPa]	278.22(21.48)	361.24(21.71)	401.83(17.33)

Table 3.14: ... continued

C_{55}[GPa]	446.82(30.08)	488.78(21.10)	608.28(22.92)
C_{66}[GPa]	471.23(15.13)	529.92(21.16)	603.33(20.60)
K^S[GPa]	572.41(7.28)	665.31(6.94)	763.37(6.18)
G[GPa]	268.61(6.62)	289.22(6.21)	334.92(4.66)
V_ϕ[km/s]	10.37(0.07)	10.94(0.06)	11.50(0.05)
V_s[km/s]	7.10(0.09)	7.21(0.08)	7.62(0.05)
V_p[km/s]	13.22(0.08)	13.75(0.07)	14.48(0.05)
$(Mg_{0.833}Fe_{0.167})(Si_{0.833}Fe_{0.167})O_3$ pPv			
T[K]	2500	2500	2500
P[GPa]	100.13(0.06)	124.99(0.08)	148.62(0.11)
ρ[kg/m^3]	5660.64	5901.82	6107.44
C_{11}[GPa]	1023.18(20.67)	1101.48(21.35)	1328.94(30.22)
C_{22}[GPa]	780.77(26.89)	840.10(23.90)	1005.59(24.20)
C_{33}[GPa]	999.17(19.27)	1136.07(28.21)	1206.58(28.97)
C_{12}[GPa]	407.02(25.32)	539.33(24.60)	650.11(28.54)
C_{13}[GPa]	390.27(22.35)	442.32(21.91)	600.69(37.28)
C_{23}[GPa]	347.86(19.09)	402.58(25.86)	447.11(25.40)
C_{44}[GPa]	283.19(28.42)	376.78(20.80)	450.16(24.82)
C_{55}[GPa]	471.29(25.34)	544.81(25.77)	563.52(32.52)
C_{66}[GPa]	468.36(20.24)	531.86(20.57)	630.52(31.05)
K^S[GPa]	574.57(7.77)	657.26(7.93)	764.80(9.83)
G[GPa]	254.93(4.79)	268.54(6.31)	316.49(8.37)
V_ϕ[km/s]	10.07(0.07)	10.55(0.06)	11.19(0.07)
V_s[km/s]	6.71(0.06)	6.75(0.08)	7.20(0.10)
V_p[km/s]	12.71(0.07)	13.12(0.07)	13.94(0.09)
$(Mg_{0.833}Fe_{0.167})(Si_{0.833}Al_{0.167})O_3$ pPv			
T[K]	2500	2500	2500
P[GPa]	100.40(0.08)	125.19(0.08)	148.85(0.07)
ρ[kg/m^3]	5437.94	5670.44	5879.37
C_{11}[GPa]	1042.68(18.75)	1196.67(18.55)	1319.04(21.65)
C_{22}[GPa]	781.39(21.85)	913.79(21.35)	991.70(27.93)
C_{33}[GPa]	980.48(23.03)	1172.71(24.28)	1290.15(30.37)
C_{12}[GPa]	407.97(18.48)	497.30(17.29)	582.61(28.58)
C_{13}[GPa]	436.07(25.54)	506.24(17.48)	543.65(26.67)
C_{23}[GPa]	332.05(22.63)	360.92(18.77)	363.85(28.35)
C_{44}[GPa]	391.88(24.18)	382.81(18.69)	418.11(24.38)
C_{55}[GPa]	452.95(24.54)	542.35(21.74)	664.78(23.65)
C_{66}[GPa]	429.74(22.91)	514.25(18.85)	533.32(23.86)
K^S[GPa]	583.91(7.52)	676.34(6.60)	745.25(8.77)
G[GPa]	259.84(4.90)	307.68(5.23)	335.59(7.93)
V_ϕ[km/s]	10.36(0.07)	10.92(0.05)	11.26(0.07)
V_s[km/s]	6.91(0.07)	7.37(0.06)	7.56(0.09)
V_p[km/s]	13.08(0.07)	13.84(0.06)	14.24(0.08)
$MgSiO_3$ pPv			
T[K]	3500	3500	3500

Table 3.14: ... continued

P[GPa]	99.05(0.06)	124.85(0.06)	149.50(0.05)
ρ[kg/m^3]	5134.98	5373.22	5578.79
C_{11}[GPa]	1095.42(24.37)	1216.12(24.23)	1294.00(24.39)
C_{22}[GPa]	782.48(23.35)	860.73(29.03)	998.04(22.61)
C_{33}[GPa]	1029.03(26.76)	1169.23(26.79)	1389.33(27.19)
C_{12}[GPa]	355.83(24.63)	467.50(26.31)	508.06(31.81)
C_{13}[GPa]	373.02(28.17)	479.20(23.92)	513.75(25.89)
C_{23}[GPa]	256.37(27.59)	291.86(27.85)	353.36(28.51)
C_{44}[GPa]	347.66(18.36)	341.01(23.48)	379.84(22.27)
C_{55}[GPa]	483.42(27.61)	438.76(21.15)	654.59(29.68)
C_{66}[GPa]	409.59(23.62)	536.28(24.78)	602.72(37.11)
K^S[GPa]	570.31(8.37)	644.52(8.46)	743.74(9.36)
G[GPa]	263.70(6.44)	298.03(6.71)	339.67(6.69)
V_ϕ[km/s]	10.54(0.08)	10.95(0.07)	11.55(0.07)
V_s[km/s]	7.17(0.09)	7.45(0.08)	7.80(0.08)
V_p[km/s]	13.40(0.09)	13.92(0.08)	14.65(0.08)
$(Mg_{0.917}Fe_{0.083})(Si_{0.917}Fe_{0.083})O_3$ pPv			
T[K]	3500	3500	3500
P[GPa]	100.19(0.05)	125.31(0.06)	150.36(0.07)
ρ[kg/m^3]	5363.48	5606.22	5820.82
C_{11}[GPa]	1022.82(28.87)	1165.49(29.05)	1331.42(40.40)
C_{22}[GPa]	824.68(31.16)	864.93(27.62)	937.87(31.74)
C_{33}[GPa]	1007.42(24.98)	1138.89(30.44)	1202.37(32.79)
C_{12}[GPa]	357.90(33.67)	427.67(29.10)	587.47(30.91)
C_{13}[GPa]	503.03(34.40)	540.94(28.41)	585.32(35.54)
C_{23}[GPa]	311.12(37.75)	395.28(27.29)	452.51(35.54)
C_{44}[GPa]	312.48(29.21)	393.27(23.14)	473.05(32.07)
C_{55}[GPa]	411.84(29.56)	462.12(30.38)	588.97(38.41)
C_{66}[GPa]	449.90(24.54)	509.64(23.15)	594.82(28.32)
K^S[GPa]	577.91(10.24)	655.36(9.25)	750.42(11.39)
G[GPa]	245.03(6.49)	277.07(7.54)	314.01(10.51)
V_ϕ[km/s]	10.38(0.09)	10.81(0.08)	11.35(0.09)
V_s[km/s]	6.76(0.09)	7.03(0.10)	7.34(0.12)
V_p[km/s]	12.99(0.10)	13.52(0.09)	14.17(0.11)
$(Mg_{0.917}Fe_{0.083})(Si_{0.917}Al_{0.083})O_3$ pPv			
T[K]	3500	3500	3500
P[GPa]	99.99(0.08)	124.89(0.07)	149.85(0.06)
ρ[kg/m^3]	5248.55	5483.8	5697.41
C_{11}[GPa]	1038.26(25.38)	1188.35(22.76)	1294.30(20.54)
C_{22}[GPa]	768.01(22.65)	916.14(31.33)	944.63(21.41)
C_{33}[GPa]	962.64(26.44)	1143.52(31.58)	1287.94(21.05)
C_{12}[GPa]	368.24(19.18)	508.98(25.12)	548.95(21.15)
C_{13}[GPa]	364.79(18.96)	455.42(25.17)	531.27(22.72)
C_{23}[GPa]	334.38(22.59)	359.64(29.90)	376.95(23.95)
C_{44}[GPa]	291.34(26.11)	370.76(26.25)	385.52(13.09)
C_{55}[GPa]	484.42(24.64)	502.41(30.58)	584.37(26.87)

Table 3.14: ... continued

C_{66}[GPa]	472.18(23.18)	465.43(29.65)	608.00(24.87)
K^S[GPa]	564.92(7.79)	656.74(9.40)	729.10(7.35)
G[GPa]	248.52(5.72)	296.53(7.29)	322.98(6.05)
V_ϕ[km/s]	10.37(0.07)	10.94(0.08)	11.31(0.06)
V_s[km/s]	6.88(0.08)	7.35(0.09)	7.53(0.07)
V_p[km/s]	13.07(0.08)	13.85(0.09)	14.27(0.07)
$(Mg_{0.833}Fe_{0.167})(Si_{0.833}Fe_{0.167})O_3$ pPv			
T[K]	3500	3500	3500
P[GPa]	95.43(0.10)	124.41(0.11)	150.61(0.13)
ρ[kg/m^3]	5529.49	5821.29	6060.41
C_{11}[GPa]	911.53(27.76)	1086.74(24.99)	1229.50(31.96)
C_{22}[GPa]	711.29(30.22)	830.00(20.55)	927.58(31.36)
C_{33}[GPa]	939.23(28.96)	1096.12(25.87)	1222.12(33.95)
C_{12}[GPa]	439.01(34.98)	454.51(23.71)	573.65(34.23)
C_{13}[GPa]	381.66(32.19)	452.01(21.72)	552.99(28.20)
C_{23}[GPa]	314.64(29.51)	393.28(27.59)	427.90(41.29)
C_{44}[GPa]	282.02(31.60)	410.04(18.71)	459.32(28.09)
C_{55}[GPa]	388.02(20.25)	489.25(25.69)	612.68(27.00)
C_{66}[GPa]	464.71(37.36)	498.52(28.97)	601.91(39.27)
K^S[GPa]	536.90(10.22)	634.50(8.14)	734.18(11.05)
G[GPa]	223.00(11.05)	263.75(6.51)	283.82(8.74)
V_ϕ[km/s]	9.85(0.09)	10.44(0.07)	11.01(0.08)
V_s[km/s]	6.35(0.16)	6.73(0.08)	6.84(0.11)
V_p[km/s]	12.28(0.13)	13.02(0.08)	13.55(0.10)
$(Mg_{0.833}Fe_{0.167})(Si_{0.833}Al_{0.167})O_3$ pPv			
T[K]	3500	3500	3500
P[GPa]	99.83(0.12)	123.02(0.10)	149.87(0.08)
ρ[kg/m^3]	5353.54	5587.93	5811.1
C_{11}[GPa]	997.00(22.29)	1172.84(30.16)	1252.29(24.19)
C_{22}[GPa]	768.79(40.51)	837.87(33.54)	932.27(27.59)
C_{33}[GPa]	963.44(25.82)	1138.46(26.04)	1273.96(28.48)
C_{12}[GPa]	400.70(19.20)	458.25(26.14)	528.91(27.80)
C_{13}[GPa]	426.90(33.33)	450.25(18.64)	526.96(29.83)
C_{23}[GPa]	333.29(17.79)	359.81(31.90)	492.94(25.29)
C_{44}[GPa]	333.19(27.43)	372.27(27.34)	468.74(20.48)
C_{55}[GPa]	439.32(32.74)	440.39(23.78)	613.86(29.18)
C_{66}[GPa]	481.09(23.58)	516.51(22.52)	612.64(22.31)
K^S[GPa]	571.52(9.28)	638.52(9.01)	744.73(8.77)
G[GPa]	225.81(9.37)	285.75(7.83)	308.32(6.61)
V_ϕ[km/s]	10.33(0.08)	10.69(0.08)	11.32(0.07)
V_s[km/s]	6.49(0.13)	7.15(0.10)	7.28(0.08)
V_p[km/s]	12.77(0.11)	13.51(0.09)	14.10(0.08)

Chapter 4

Novel Hydrogen-oxygen Compounds at Giant-planet Interior Pressures

They must also learn how to abandon their pet theories when the scientific evidence goes against them or they will only expose themselves to ridicule. - Francis Crick

4.1 Introduction

As one of the most abundant substances in the solar system, water ice at high pressure [131, 132] is of fundamental importance in planetary science [133]. Over the last two years, a significant effort has been devoted to finding the ground-state structures of ice at the multimegabar pressures corresponding to the cores of gas giant planets (15-20 Mbar for Saturn and 40-60 Mbar for Jupiter). Militzer and Wilson [134] demonstrated that the *Pbcm* phase [132] becomes unstable above 7.6 Mbar and predicted a new structure of *Pbca* symmetry. Wang *e*t al. [135] showed that, at 8.1 Mbar, water ice assumes another structure of $I\bar{4}2d$ symmetry instead of transforming into a *Cmcm* structure as proposed in Ref. [134]. Refs. [136, 137, 138] instead proposed a structure with $Pmc2_1$ symmetry to appear in the same pressure regime, but it has a higher enthalpy than the $I\bar{4}2d$ structure. Around 12 Mbar, a transition to a structure with $P2_1$ symmetry was consistently predicted in Refs. [135, 136, 137, 138]. Even higher pressure studies predict a $P2_1/c$ structure at 20 Mbar [137], and a metallic $C2/m$ structure at 60 Mbar [136, 138]. In nature, however, high-pressure water phases are rarely found in isolation, and, in gas giants, an icy core may be surrounded by a vast reservoir of hydrogen-rich fluid or exist in a mixture with the other planetary ices, such as ammonia and methane. Recent work has emphasized the fact that counterintuitive stoichiometries can occur in post-perovskite materials at extreme pressures [139]. This raises the question of whether H_2O is indeed the ground-state stoichiometry for water at high pressure in hydrogen-rich environments, or whether pressure effects are likely to result in the formation of novel ice-like phases with non-H_2O stoichiometry.

In this study, we apply *ab initio* random structure searching (AIRSS) methods [60] to

determine the ground-state structure of hydrogen-oxygen compounds at extreme pressures, and to explore whether the H_2O stoichiometry of water is maintained at high pressure. The AIRSS method relies on the generation of a large number of random geometries whose structures are then optimized using density functional theory. In the AIRSS process, randomly generated unit cells are filled with randomly positioned atoms, and the structures are geometrically relaxed to the targeted pressure. Structures with competitive enthalpy are picked out and re-evaluated with more accurate thermodynamic calculations, from which the most stable structure can be determined. Although the AIRSS method is not guaranteed to find the most stable phase, it has achieved remarkable success in discovering structures across a wide range of materials [140, 141, 142, 143].

4.2 Methodology

In our calculations, structural optimization is performed using the Vienna *ab initio* simulation package (VASP) [96, 144]. Projector augmented wave (PAW) pseudopotentials [145] and the Perdew-Burke-Ernzerhof [146] exchange-correlation functional are used. The pseudopotential cutoff radii equal to 0.8 and 1.1 Bohr for H and O, which are similar to those used in previous works [136, 138]. We have performed additional all-electron calculations, in order to verify the findings based on using these pseudopotentials. For efficiency of the AIRSS method, a cutoff energy of 900 eV is chosen for initial relaxation, which is then increased to 1700 eV for more precise calculations on favorable structures. Likewise, a relatively sparse Monkhorst-Pack grid [99, 147] ($6 \times 6 \times 6$) is used initially, which is later replaced by a $20 \times 20 \times 20$ grid. Tests at the largest energy cutoff and grid size show that the total system energies are converged to the order of 1 meV, while the energy difference is converged to 0.1 meV.

4.3 Results and discussion

As an initial step, we recomputed enthalpies of recently reported [134, 135, 136, 137] H_2O structures as a function of pressure, assembling all proposed structures for comparison. Figure 4.1 shows the transition sequence up to the highest reported pressure (70 Mbar) as follows: $X \rightarrow Pbcm \rightarrow Pbca \rightarrow I\bar{4}2d \rightarrow P2_1 \rightarrow P2_1/c \rightarrow C2/m$, consistent with previous reports. Note that the $Pmc2_1$ structure predicted in Refs. [136, 137, 138] is less stable than the $I\bar{4}2d$ structure reported by Wang *et* al. [135] at all pressures; as the $I\bar{4}2d$ structure has eight formula units (f.u.) per unit cell, it was less likely to be generated by random search algorithms.

With a quickly increasing number of known massive exoplanets, it is worthwhile to explore stable H_2O structures at even higher pressure. We use the AIRSS method to generate between 1000 and 3500 H_2O unit cells with 1-4 f.u. at pressures of 100, 150, 300, 400, and 500 Mbar. Additionally, we generate between 750 and 1150 structures with 5-8 f.u.

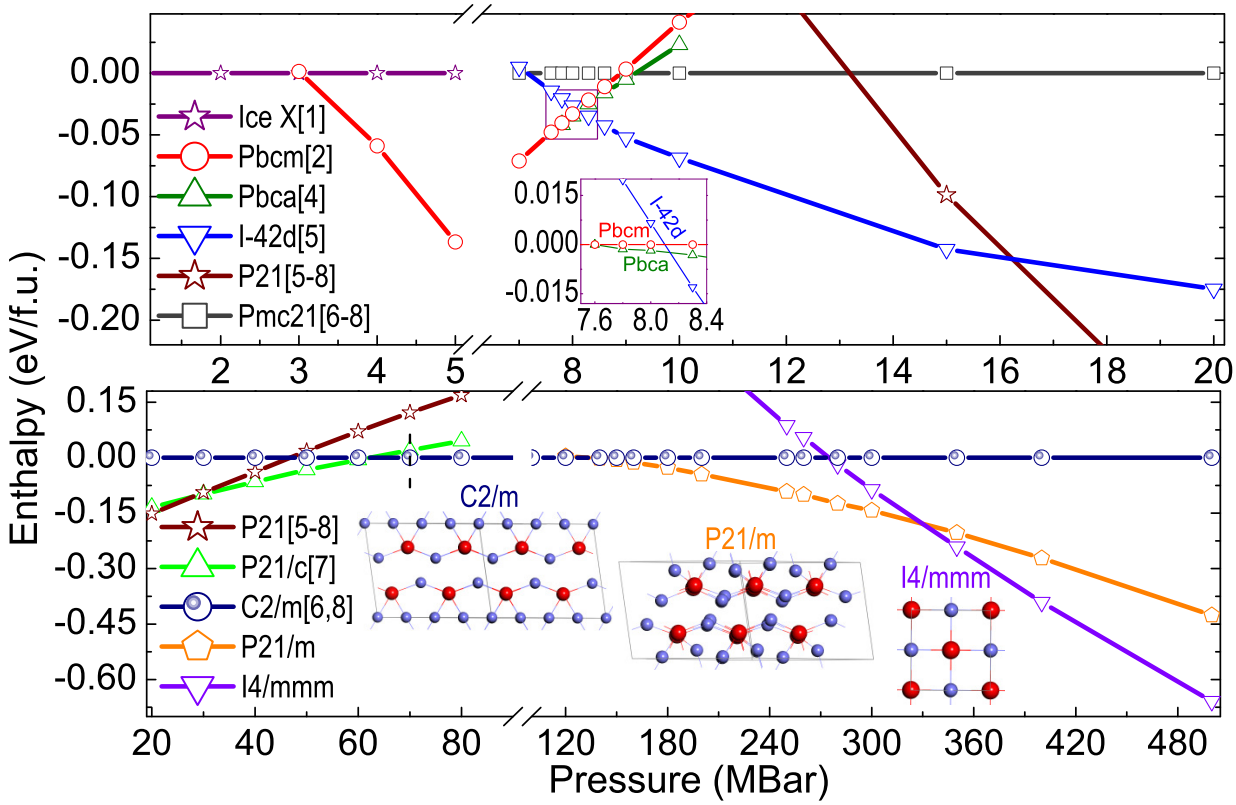

Figure 4.1: Enthalpy versus pressure of different water ice structures. The reference following the name of each phase is the corresponding earliest report. In the lower panel, structures are provided for $C2/m$, $P2_1/m$ and $I4/mmm$, where large red and small blue spheres represent O and H atoms, respectively. The dashed line at 70 Mbar indicates the highest pressure explored in previous work.

at pressures of 100 and 200 Mbar. Note that the number of structures generated here is comparable to recent reports on the AIRSS method [148, 149].

Figure 4.1 shows two new, stable phases with $P2_1/m$ and $I4/mmm$ symmetry that appear at high pressure. More stable than $C2/m$ above 135 Mbar, the $P2_1/m$ phase is also a monoclinic, layered structure that resembles the $C2/m$ phase except that O-H-O bonds are divided into two classes: one is shortened and straight, while the other is squeezed and distorted in different directions. At 330 Mbar, $P2_1/m$ is replaced by a tetragonal $I4/mmm$ phase, which has the same structure as the $L'2$ phase of ThH_2. $I4/mmm$ remains the most stable structure up to 500 Mbar. Similar to the $C2/m$ structure, an analysis of the electronic band structure shows that the $P2_1/m$ and $I4/mmm$ phases are metallic. Structural parameters of these two phases are listed in Table 4.1.

In addition to our initial studies on water ice, we used the AIRSS method to investigate hydrogen (results see Fig. 4.2). Below 50 Mbar we find the same progression of ground

Table 4.1: Structural parameters of selected H, H_2O, H_3O, and H_4O phases.

Structure name No. of atoms	Pressure (Mbar)	Lattice parameters a, b, c (Å) α, β, γ (°)	Atomic positions (Fractional)
H: $Cmcm$ 4	60	0.935, 1.459, 1.317 90, 90, 90	H: 1/2 0.1642 1/4
H: *hcp* ($P6_3/mmc$) 2	120	0.719, 0.719, 1.136 90, 90, 120	H: 2/3 1/3 3/4
H_2O: $P2_1/m$ 12	250	1.866, 1.398, 1.941 90, 103.884, 90	H1: 0.6459 3/4 0.9253 H2: 0.4006 3/4 0.6320 H3: 0.0188 1/4 0.2515 H4: 0.9084 1/4 0.6569 O1: 0.7537 1/4 0.9484 O2: 0.2662 1/4 0.5733
H_2O: $I4/mmm$ 6	400	1.378, 1.378, 1.032 90, 90, 90	H: 1/2 0 1/4 O: 0 0 1/2
H_3O: $Cmmm$ 24	80	2.295, 1.633, 3.797 90, 90, 90	H1: 0.2849 0 0.3184 H2: 0 0 1/2 H3: 1/2 0 0.9136 H4: 0.2351 0 0 O1: 0 0 0.1928 O2: 1/2 0 1/2
H_3O: $C2/m$ 32	100	5.275, 1.553, 3.595 90, 144.354, 90	H1: 0.0416 1/2 0.1392 H2: 0.3298 1/2 0.4729 H3: 0.8928 1/2 0.3238 H4: 0.9839 1/2 0.7340 H5: 0.4374 1/2 0.0613 H6: 0.1548 1/2 0.0616 O1: 0.7166 1/2 0.3090 O2: 0.6040 1/2 0.7693
H_3O: *bcc* ($Im\bar{3}m$) 8	140	1.542, 1.542, 1.542 90, 90, 90	H: 0 0 1/2 O: 0 0 0
H_4O: $Pnma$ 20	100	2.8035, 1.5630, 2.2135 90, 90, 90	H1: 0.8538 3/4 0.1977 H2: 0.6232 3/4 0.9150 H3: 0.0612 3/4 0.2068 H4: 0.5201 1/4 0.4692 O: 0.8202 3/4 0.6306

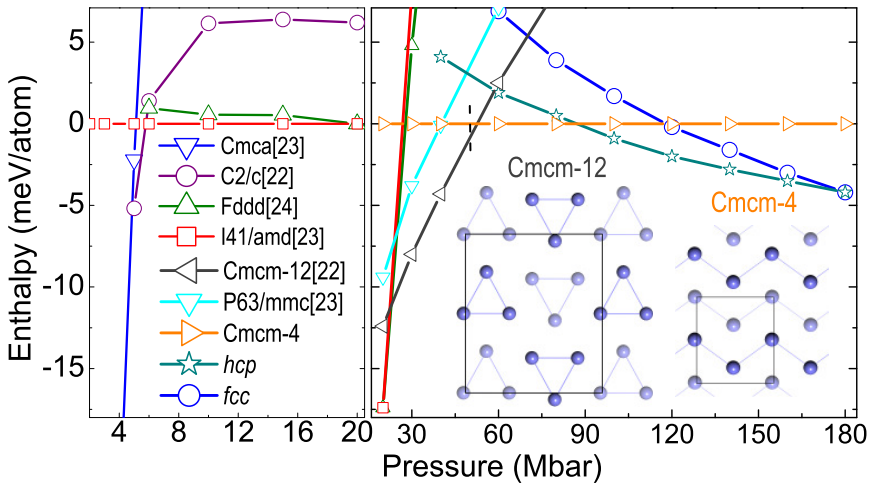

Figure 4.2: Enthalpy versus pressure of different structures of hydrogen relative to $I4_1/amd$ [151] in the left panel and the 4-atom $Cmcm$ phase on the right. The reference for each phase is given in the legend. In the right panel, structures of the 12-atom $Cmcm$ of Ref. [150] and our new 4-atom $Cmcm$ are compared. The dashed line at 50 Mbar indicates the highest pressure explored in previous work.

state structures, $Cmca \rightarrow C2/c \rightarrow I4_1/amd$ $(or\ Fddd) \rightarrow Cmcm$, as has been reported previously [150, 151, 152]. When pressure exceeds 54 Mbar, we find that the 12-atom per unit cell $Cmcm$ structure of Ref. [150], hereafter $Cmcm$-12, becomes less stable than a new $Cmcm$-4 structure, in which three groups of bonds (different in length) exist without forming in-plane H_3 clusters [150]. As pressure increases to 87 Mbar, the *hcp* structure (symmetry $P6_3/mmc$) becomes stable. Different from the $P6_3/mmc$ structure predicted in Ref. [151] ($c/a \approx 2$), our *hcp* lattice exhibits a smaller c/a ratio of 1.58. The *hcp* structure remains stable until being replaced by the fcc lattice at 180 Mbar.

Having computed the ground state structures of H and H_2O throughout a wide pressure range, we now explore novel hydrogen-oxygen stoichiometries, including hydrogen-enriched structures H_3O, H_4O, H_6O and H_8O and oxygen-rich structures HO, HO_2 and HO_4. Between 200 and 3000 random structures with up to 8 f.u. at pressures of 20-500 Mbar were generated, depending on the specific computational cost and searching efficiency. We have only considered crystalline compounds in this study. Any defects, stacking faults, or other non-stoichiometric arrangements of atoms have been neglected because this study is focused on the ground state.

Figure 4.3 compares the stability of structures with different stoichiometries using a convex hull diagram [153]. This diagram shows the enthalpy of formation (EOF) per atom, E_f, of the most stable H_mO_n compounds with respect to the elements. For each fractional concentration of oxygen, $x = n/(m+n)$, a compound H_mO_n is stable relative to separate A and B phases (A+B) of different concentrations if its EOF lies below the line joining those two phases. This approach is valid for determining structural stability at zero-temperature,

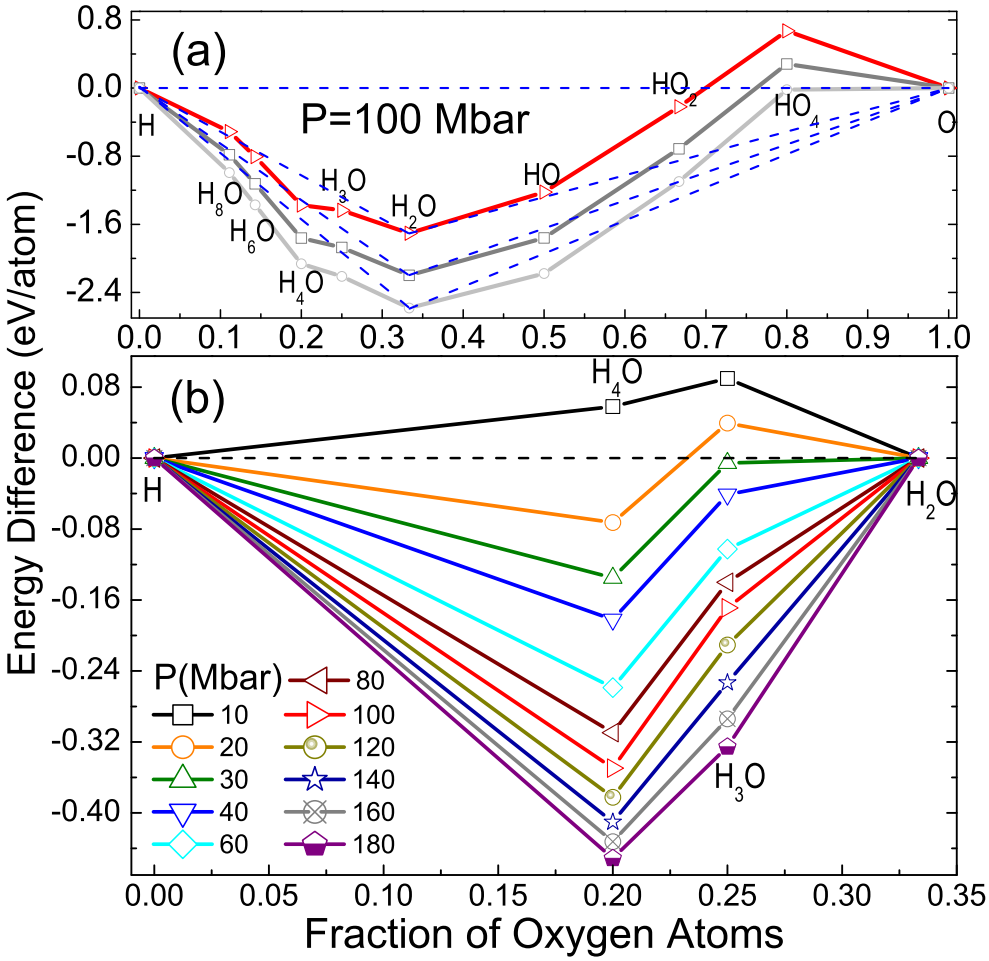

Figure 4.3: (a) Enthalpy of formation (EOF, in red) of different H-O compounds with respect to H and O at 100 Mbar. The gray lines underneath represent the corresponding differences in Gibbs free energy at two temperatures, 9000 K (dark gray) and 16000 K (light gray), by adding an entropy term to the enthalpy using the ideal binary solution model. (b) EOF of hydrogen-rich H-O compounds with respect to H and H_2O at several pressures.

when the Gibbs free energy is equivalent to the enthalpy, as in our case. In Fig. 4.3(a) we plot a convex hull diagram showing the EOF of possible H-O phases at a pressure of 100 Mbar. The H_4O structure emerges as the most stable on the hydrogen-enriched side of the diagram, implying that any H-O complex with an H:O concentration greater than 2:1 will preferentially form H_4O+H or H_4O+H_2O, in contrast to H_2O+H_2 we expect at ambient pressure. On the oxygen-rich side of the graph, the HO, HO_2 and HO_4 phases are unstable relative to H_2O+O.

In Fig. 4.3(b) we focus on the EOF of hydrogen-enriched compounds including the H_3O and H_4O phases, with respect to their end members H and H_2O. Based on our calculations

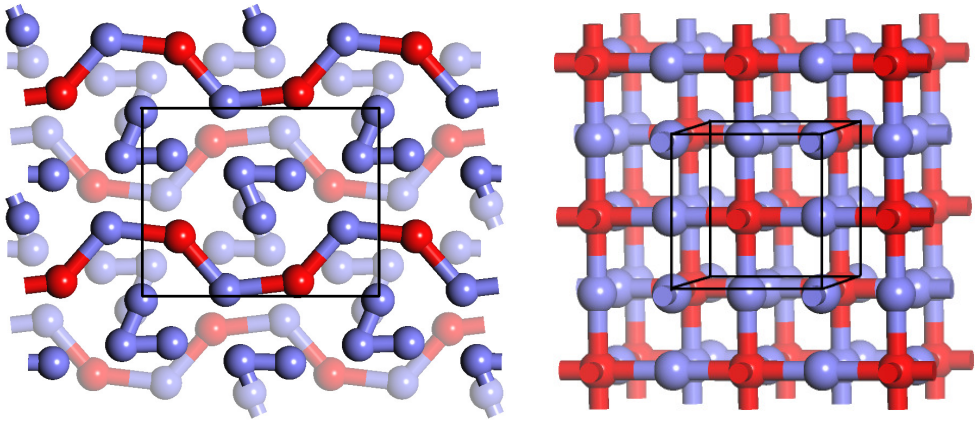

Figure 4.4: Structures of H_4O-*Pnma* (left) and H_3O-*bcc* (right). Red and blue spheres denote O and H atoms, respectively.

at 10 and 20 Mbar, we predict H_4O to become stable relative to $H+H_2O$ at 14 Mbar. Such a pressure is predicted at the core boundary of Saturn and far below that of Jupiter. For pressures above 140 Mbar, we find H_3O becoming stable relative to H_2O+H_4O. These results imply that at giant-planet core-boundary pressures, in the absence of temperature effects, hydrogen and oxygen exist in the form of the novel hydrogen-rich compound, H_4O, instead of separate water ice and hydrogen. On the other hand, no oxygen-rich compounds will form, which is in agreement with recent calculations at high temperatures [154].

The H_4O phase that we find here is a layered orthorhombic structure with *Pnma* symmetry. Each layer is characterized by -H-O-H-O- chains, of which each O is associated with one H_3 unit shown in Fig. 4.4. Our band structure analysis shows that the H_4O structure becomes metallic at 80 Mbar. For H_3O, we find a *bcc* ($Im\bar{3}m$) structure above 110 Mbar, a layered monoclinic $C2/m$ structure (see Fig. 4.5(left)) at 20-110 Mbar, and a slightly less stable orthorhombic *Cmmm* structure (see Fig. 4.5(right)) between 20 and 100 Mbar, whose enthalpy is very close (2-36 meV/f.u.) to that of the $C2/m$ structure.

To verify the applicability of the PAW pseudopotential under extreme pressures, we performed all-electron LAPW calculations using the ELK code [155]. The LAPW calculations for hydrogen at 80-180 Mbar reconfirm the $Cmcm \rightarrow hcp$ transition at 87 Mbar and increase the enthalpy of the fcc structure by 5 meV, precluding fcc to become stable until a pressure of about 200 Mbar is reached. We also recalculated the EOF of H_3O with respect to H and H_2O at 100 Mbar, and found that the difference between the two methods is only 4 meV/f.u.. We further replaced the VASP-PAW pseudopotential of oxygen with an all-electron PAW potential (cutoff radius equals to 0.95 Bohr), re-optimized two H_2O structures, $I4/mmm$ and $C2/m$, and compared their enthalpy. The enthalpy difference, between the $I4/mmm$ and the $C2/m$ structures, increases by 16 and 70 meV/f.u. at 180 and 400 Mbar, respectively. All these corrections are small and confirm our prediction of two new ice phases, although their transition pressures increase slightly (by $< 4\%$ for $P2_1/m$, $< 18\%$ for $I4/mmm$).

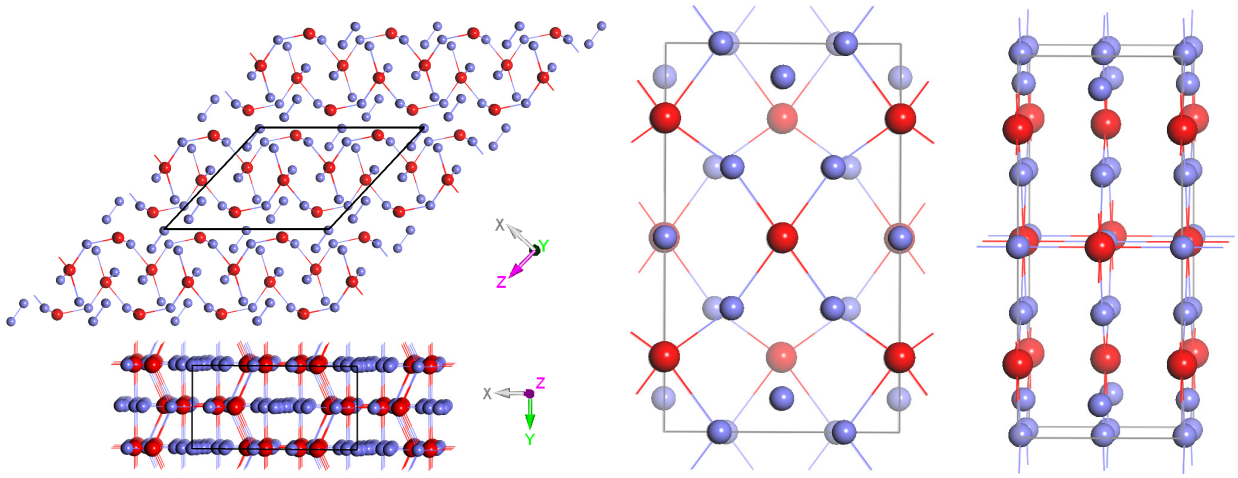

Figure 4.5: (left) Two views of the H_3O-$C2/m$ structure, characterized by atomic layers connected by H-O chains that are either straight or zigzag; (right) top and side views of H_3O-$Cmmm$ structure, consisting of H-O atomic planes that are connected by straight H-O chains. Red and blue spheres denote oxygen and hydrogen atoms, respectively. Different color depth corresponds to different atomic planes.

Table 4.2: Zero point energy (ZPE, in units of eV/f.u.) of H, H_2O, H_3O, and H_4O structures at 20 and 180 Mbar.

Structure	ZPE (20 Mbar)	ZPE (180 Mbar)
H-$I4_1/amd$	0.443	
H_2O-$P2_1$	1.268	
H_3O-$Cmmm$	1.725	
H_4O-$Pnma$	2.213	4.603
H-$fcc(Fm\bar{3}m)$		0.830
H_2O-$P2_1/m$		2.571
H_3O-$bcc(Im\bar{3}m)$		3.756

We also estimated the influence of zero-point motion (ZPM) by phonon calculations with $2 \times 2 \times 2$ supercells using the finite displacement method [37]. Including zero-point energy (see Table 4.2), the convex hull diagram in Fig. 4.3(b) shifts in the positive direction by 12 meV/atom for H_4O and 3 meV/atom for H_3O at 20 Mbar, and by 74 meV/atom for H_4O and 89 meV/atom for H_3O at 180 Mbar. By applying these changes to the linearly interpolated enthalpy, we estimate the ZPM increases the pressure at which H_4O and H_3O become more stable than their corresponding $H+H_2O$ by, at most, 1.3 Mbar. Relative to H_2O+H_4O, H_3O becomes less stable below 180 Mbar. We note that, based on the findings in Refs. [136, 138], the ZPM-induced changes in the enthalpy differences between H_2O structures are small and do not change the sequence of phase transition, although the transition pressures will be slightly affected. Further, the difference in the zero-point energy of different hydrogen structures is small ($<$ 80 meV/atom when below 50 Mbar), as indicated in Ref. [151], and will not change our conclusions on the stability of H_4O.

In order to understand how temperature affects the stability, we re-examined the energy relation in Fig. 4.3(a) by implementing an ideal mixing model to add an entropy term to the energy of formation. Two temperatures were considered, 9000 K and 16000 K. The results show that H_4O and H_3O become more stable than their corresponding $H+H_2O$, as temperature increases. Moreover, an oxygen-rich phase HO becomes more stable than $O+H_2O$ at these temperatures. Using similar estimations in Fig. 4.3(b) shows that, at T=9000 K, the pressures at which H_4O and H_3O become more stable than $H+H_2O$ are $\sim$10-Mbar lower than those at T=0 K. Despite favorableness of the formation of hydrogen-oxygen compounds with stoichiometries other than H_2O, it should be noted that exact phase relations of the hydrogen-oxygen compounds at giant-planet core temperatures are still uncertain, because of the over-simplification of the ideal mixing model and the difficulties in determining the precise Gibbs free energies. Treating pure hydrogen or hydrogen-bearing compounds requires careful considerations of nuclear quantum effects, anharmonic effects, van der Waals interactions, etc. [156], which are beyond the scope of the present study.

4.4 Summary

In this work we have replicated and extended the phase diagram of solid hydrogen to 180 Mbar and that of water ice to 500 Mbar. We also predict novel, hydrogen-enriched meta-ice structures to become more stable than separate hydrogen and water ice phases at high pressure. Our results imply that under conditions in excess of 14 Mbar at low temperature a hydrogen-rich H_4O phase exists instead of separate water ice and hydrogen phases. The 14 Mbar pressure in question is comparable to the core-boundary pressure of Saturn and far below the core pressure of Jupiter, and may potentially also be reached inside super-Neptune ice giants. This result stands in contrast to the tendency of methane to preferentially expel hydrogen from its own structure under pressure to form hydrocarbons and eventually diamond [157], and in ice mixtures methane could potentially provide the excess hydrogen to form H_4O. These results underline the fact that consideration of structures likely to form at

giant-planet core conditions requires looking beyond traditional ambient-pressure chemistry to explore unfamiliar stoichiometries and combinations of elements.

Chapter 5

Equation of State of Warm Dense Sodium

It may be that everything we do is determined by some grand unified theory. - Stephen Hawking

5.1 Introduction

High energy density physics and astrophysics require reliable equation of state (EOS) of warm dense matter. In the limit of high temperature (above 10^3 eV), materials transit into weakly-interacting plasmas because of strong thermal ionization. In these occasions, the uniform electron gas model (ideal Fermi gas theory) and the Debye-Hückel theory are good approximations. At low to intermediate temperatures (below 100 eV), standard density functional theory molecular dynamics (DFT-MD) are suitable options because of their accuracy. However, the dependence of these simulations on electronic orbitals limits their applicability to high temperatures, at which the number of occupied orbitals is too high for the Kohn-Sham equation to be solvable. Recent developments in path integral Monte Carlo (PIMC) with free-particle (FP) nodes have bridged the gap between DFT-MD and the high temperature limit for several heavy elements ($Z > 2$) and compounds [47, 48, 49, 50, 51].

In this study, we apply DFT-MD and PIMC with localized, Hartree-Fock (HF) nodal structure and enhanced permutation sampling to study warm dense sodium (Na)—an element that has been of wide interests among high-pressure physicists. This traditionally believed "simple metal" adopts a series of non-close-packed phases under high pressure [158], associated with changes in optical and electronic properties [159, 160] and melting behavior [161, 162]. It was also found that Na turns insulating at 200 GPa and re-metalizes at 15.5 TPa [163, 164, 165].

The EOS and shock-compression predictions from the present study are instructive for future work on Na at high-pressure, temperature conditions, characteristic of deep interiors of giant planets and stars, planetary impacts, or thermonuclear fusion, and help build more

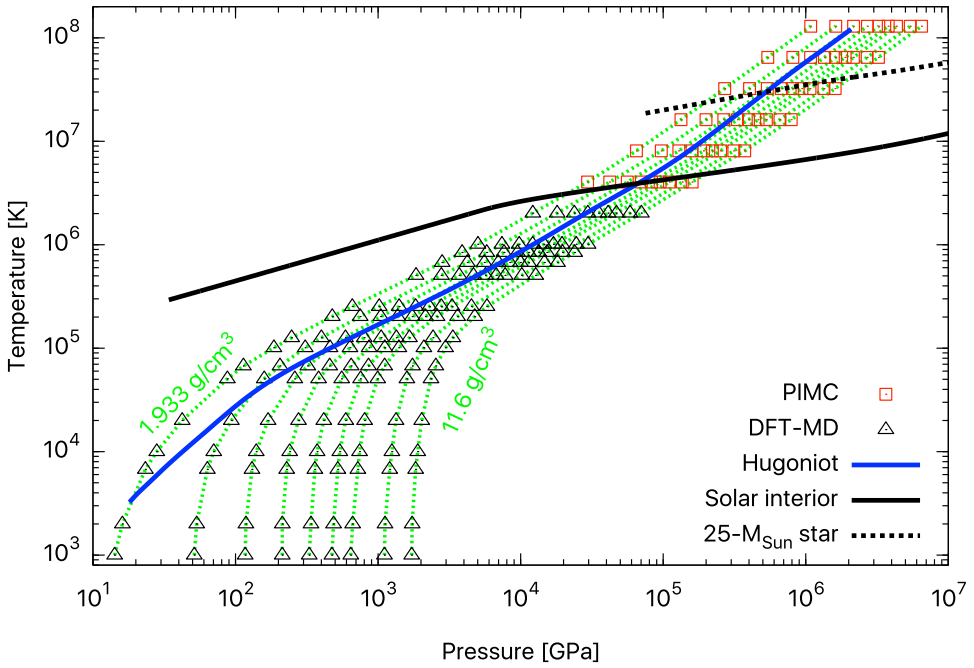

Figure 5.1: The nine isochores (green dotted lines, left to right corresponding to 2-12ρ_{ambient} respectively) computed in this work as shown in a pressure-temperature plot. The principle Hugoniot curve (blue solid line), along with the interior profiles of the Sun [166] and a star that is 25 times as massive as the Sun at the end of its helium burning time[1], are also plotted for comparison. Red squares and dark triangles represent the conditions of our path integral Monte Carlo (PIMC) and density functional theory-based molecular dynamics (DFT-MD) simulations, respectively.

accurate models for astrophysical applications.

5.2 Calculation methods

Our simulations are based on a cell with 8 atoms, except for some low-temperature cases of DFT-MD, for which a bigger cell with 54 atoms is computationally affordable. We consider nine isochores of 2-, 3-, 4-, 5-, 6-, 7-, 8-, 10-, and 12-times ambient density ρ_{ambient}, each of which is studied at a range of temperatures between 10^3 and 1.29×10^8 K, relevant to stellar science studies (see Fig. 5.1). DFT-MD makes use an exchange-correlation functional within the local density approximation (LDA) [34, 35] and PIMC simulations are within the fixed node approximation [45], similar to those implemented in Ref. [51]. In DFT-MD, we chose a projected augmented wave pseudopotential [97, 96] that treats $1s^2$ as core electrons

[1]Data courtesy of Cyril Georgy, University of Keele (United Kingdom).

and has a small core radius of 1.45 Bohr, plane wave basis with 4000 eV cutoff, Γ-point for sampling the Brillouin zone, and a time step of 0.2 fs. Typical length of the MD simulations exceeds 0.4 ps. In order to correct the difference in energy arising from the usage of a pseudopotential, we performed all-electron simulations on an isolated Na with the OPIUM code [167] to compare with a regular DFT-MD simulation on a Na contained in a box of 5×5×5 Bohr^3, and determined the value of -161.3386 Ha/atom to shift for all VASP internal energies.

5.3 Results

Comparison of PIMC methods

As introduced in Sec. 2.3, PIMC simulations on systems with more than two electrons suffer from the sign problem, which may be solved with the fixed node approximation [45] that restricts paths to positive regions of a trial density matrix, $\rho_T(\mathbf{R}, \mathbf{R}_t; t) > 0$. The restricted path integral reads,

$$\rho_F(\mathbf{R}, \mathbf{R}'; \beta) = \frac{1}{N!} \sum_{\mathcal{P}} (-1)^{\mathcal{P}} \int_{\mathbf{R} \to \mathcal{P}\mathbf{R}',\, \rho_T > 0} d\mathbf{R}_t e^{-S[\mathbf{R}_t]}, \tag{5.1}$$

where $\mathcal{P}$ denotes permutations of identical particles, and S is the action that weights every path. The most common approximation to the trial density matrix is a Slater determinant of single-particle density matrices,

$$\rho_T(\mathbf{R}, \mathbf{R}'; \beta) = \left|\left| \rho^{[1]}(\boldsymbol{r}_i, \boldsymbol{r}'_j; \beta) \right|\right|_{ij}, \tag{5.2}$$

in combination with the free-particle density matrix,

$$\rho_0^{[1]}(\boldsymbol{r}, \boldsymbol{r}'; \beta) = \sum_{\boldsymbol{k}} e^{-\beta E_{\boldsymbol{k}}} \Psi_{\boldsymbol{k}}(\boldsymbol{r}) \Psi^*_{\boldsymbol{k}}(\boldsymbol{r}'), \tag{5.3}$$

where $\Psi_{\boldsymbol{k}}(\boldsymbol{r})$ denotes plane waves.

PIMC with FP nodes gives exact results in the limit of high temperature [46]. In Ref. [51], it has been shown that the applicability range of PIMC simulations can extend to lower temperatures when a number of n_s atomic orbitals are introduced into the nodes,

$$\rho^{[1]}(\boldsymbol{r}, \boldsymbol{r}', \beta) = \rho_0^{[1]}(\boldsymbol{r}, \boldsymbol{r}'; \beta) + \sum_{I=1}^{N} \sum_{s=0}^{n_s} e^{-\beta E_s} \Psi_s(\boldsymbol{r} - \boldsymbol{R}_I) \Psi^*_s(\boldsymbol{r}' - \boldsymbol{R}_I)\,. \tag{5.4}$$

Here, we tested various methods on one sodium in a 5-Bohr cubic box, and compared the results in Fig. 5.2 and Table 5.1.

Figure 5.2 shows that, at temperatures of $T \geq 2 \times 10^6$ K, all PIMC energies and pressures are systematically higher than our DFT-MD results within LDA or generalized gradient approximation in the Perdew-Burke-Ernzerhof type (GGA-PBE) [146]. This can be attributed

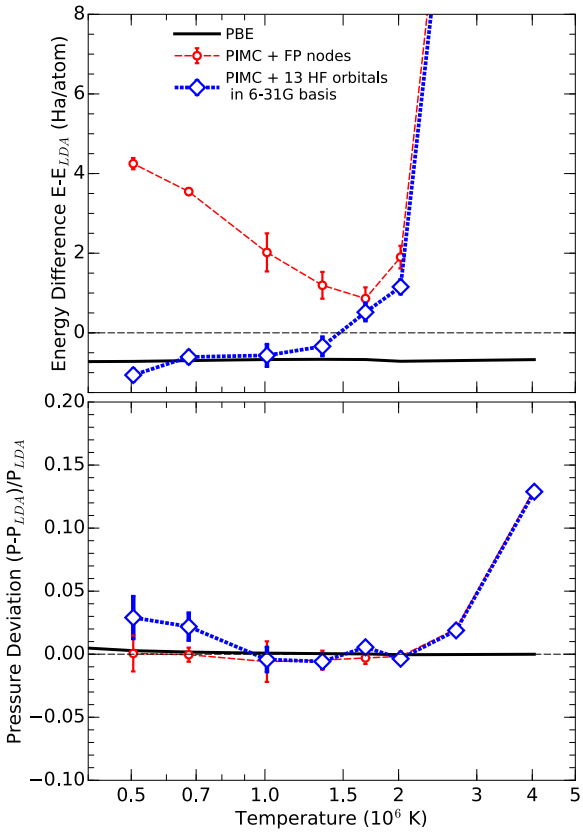

Figure 5.2: Internal energies and pressures of a single Na atom in a 5-Bohr-edge cubic cell calculated using different methods. Dark lines represent DFT-MD within generalized gradient approximation in the Perdew-Burke-Ernzerhof type (GGA-PBE, solid lines) or within local density approximation (LDA, dashed lines). Colored dash lines represent PIMC results within fixed-node approximation by means of free-particle (FP, in red) nodes or Hartree-Fock (HF) nodes using a 6-31 G basis set (in blue).

to the excitations of 1s electrons, which are similarly treated as the other outer-shell electrons in PIMC, but frozen in DFT-MD by the usage of pseudopotentials.

At temperatures of $T \leq 2 \times 10^6$ K, the energies from PIMC computations with FP nodes are systematically too high, while the pressures remain quite reasonable. This suggests that FP nodes do not lead to the correct K and L shell structures of the atom, which is more a local property, so the error in the energy does not depend too much on density. This leads to the still correct pressure, which is the volume (density)-derivative of the energy. In contrast, using PIMC with HF nodes, the results are in much better agreement with PBE predictions.

Table 5.1 lists additional PIMC results for two temperatures. In all cases, the orbitals were derived with spin-restricted GAMESS [168] calculations of the Na^+ ion so that we can use the same orbitals for both spin channels in PIMC calculations. This is a reasonable

Table 5.1: Comparison of energies and pressures calculated using different methods. The internal energies are in units of Ha/atom, pressures are in GPa.

Method		Basis	n_s	E	σ_E	E-E_{LDA}	P	σ_P	P-P_{LDA}
T=	2020958 K								
LDA				-60.61	0.00	0.00	11354.6	0.0	0.0
PBE				-61.32	0.00	-0.71	11349.6	0.0	-4.9
PIMC	FP		0	-58.67	0.46	1.93	11356.4	68.1	1.8
PIMC	HF	6-31G	6	-59.06	0.37	1.55	11357.7	56.0	3.1
PIMC	HF	6-31G	13	-59.45	0.19	1.16	11313.6	29.7	-41.0
PIMC	HF	6-31+G	13	-59.15	0.27	1.46	11362.1	42.6	7.5
PIMC	HF	6-31+G	17	-59.13	0.31	1.48	11360.8	49.3	6.2
PIMC	LDA	6-31G	13	-59.77	0.43	0.83	11283.4	66.3	-71.2
PIMC	PBE	6-31G	13	-59.28	0.34	1.32	11340.0	53.0	-14.6
PIMC	PBEX	6-31G	13	-58.92	0.39	1.69	11405.4	59.9	50.8
T=	1010479 K								
LDA				-112.87	0.00	0.00	4528.0	0.0	0.0
PBE				-113.54	0.00	-0.67	4531.8	0.0	3.8
PIMC	FP		0	-111.14	0.80	1.73	4474.0	125.2	-54.0
PIMC	HF	6-31G	6	-113.12	0.33	-0.24	4544.7	51.5	16.7
PIMC	HF	6-31G	13	-113.44	0.29	-0.57	4508.9	45.8	-19.1
PIMC	HF	6-31+G	13	-113.47	0.23	-0.60	4508.2	37.0	-19.8
PIMC	HF	6-31+G	17	-112.73	0.31	0.15	4627.1	49.9	99.1
PIMC	LDA	6-31G	13	-113.53	0.36	-0.65	4473.6	55.7	-54.4
PIMC	PBE	6-31G	13	-113.67	0.32	-0.80	4466.6	52.6	-61.4
PIMC	PBEX	6-31G	13	-113.38	0.32	-0.51	4507.5	50.8	-20.5

approximation because the spin state is of minor importance in calculations of electrons that are highly excited by temperature. DFT-MD calculations within LDA and GGA-PBE confirmed that the spin-polarized (5+6) and spin-unpolarized calculations yield similar results for the temperature range under consideration.

We need at least 6 atomic orbitals to provide a bound state for every electron. Table 5.1 shows that we found no statistically significant difference between using 6 and 13 HF orbitals in PIMC calculations, for both temperatures. At $T \approx 2 \times 10^6$ K, the PIMC pressure becomes too high when we increase the number of orbitals to 17. We attribute this deviation to our small simulation cell of 5.0 Bohr edge. The highest atomic orbitals are too delocalized to fit into this cell.

We also found no statistically significant differences between using a 6-31G and a slightly more accurate 6-31+G basis set. Both yield similar HF energies that are 0.176 Ha higher

than basis set-converged HF calculations with a TZV basis. Therefore, in the following we choose 13 HF orbitals that are generated with 6-31+G basis in Eq. 5.4.

Furthermore we tested whether there would be an advantage in deriving the atomic orbitals with LDA or PBE methods rather than with HF theory. However, no significant differences could be found. In addition, orbitals derived with just PBE exchange (PBEX) lead to similar PIMC results.

Equation of state

Figure 5.3 shows the calculated internal energies and pressures along nine isochores. In order to verify the consistency of present PIMC results with existing EOS theories for warm dense matter, we compare the calculated internal energies and pressures with the Debye-Hückel model, which screens each electron in a spherical region to approximate the deviation from ideal plasmas, and the ideal Fermi electron gas model, which is exact when the system is fully ionized at high temperature[2].

Our calculations show that, both internal energies and pressures increase with temperature, because of the growing contribution of the kinetic energy and the thermal pressure. At low temperatures, the ideal Fermi electron gas model significantly overestimates the energy and the pressure, because of the neglecting of bound-state energies and their contributions to the pressure. The curves are lowered down in the Debye-Hückel model, which introduces a screening length that better counts the deviation from ideal plasmas. However, because of its simplicity, the accuracy of the Debye-Hückel model is questionable at low temperatures when thermal ionization is weak.

We find excellent agreement between PIMC and DFT-MD at 10^6 K. At high temperatures of $T > 2 \times 10^7$ K, our PIMC results agree with that from the Debye-Hückel model as well as the Fermi electron gas theory, because the temperatures are so high that the atoms are fully ionized. As T decreases, the system gradually deviates from the ideal Fermi electron gas and becomes better described by the Debye-Hückel model, until 6×10^6 K. The success in bridging analytical models in the high-temperature limit, and DFT-MD at 10^6 K, validates the EOS data from present PIMC simulations with fixed-node approximation, and the use of a frozen core and a zero-temperature exchange-correlation functional in DFT-MD.

We also compare the nuclear pair correlation functions $g_{\text{Na-Na}}(r)$ in DFT-MD and in PIMC simulations. As an example, Fig. 5.4 shows $g_{\text{Na-Na}}(r)$ from PIMC and DFT-MD at 10^6 K and 8-fold compression. The consistency between the two supports the reliability of the present PIMC simulations in predicting correct ionic plasma structures.

[2]Here, we include the kinetic energy of the nuclei when calculating the total internal energy of the ideal Fermi electron gas model, but have not considered the charge and interaction of the nuclei.

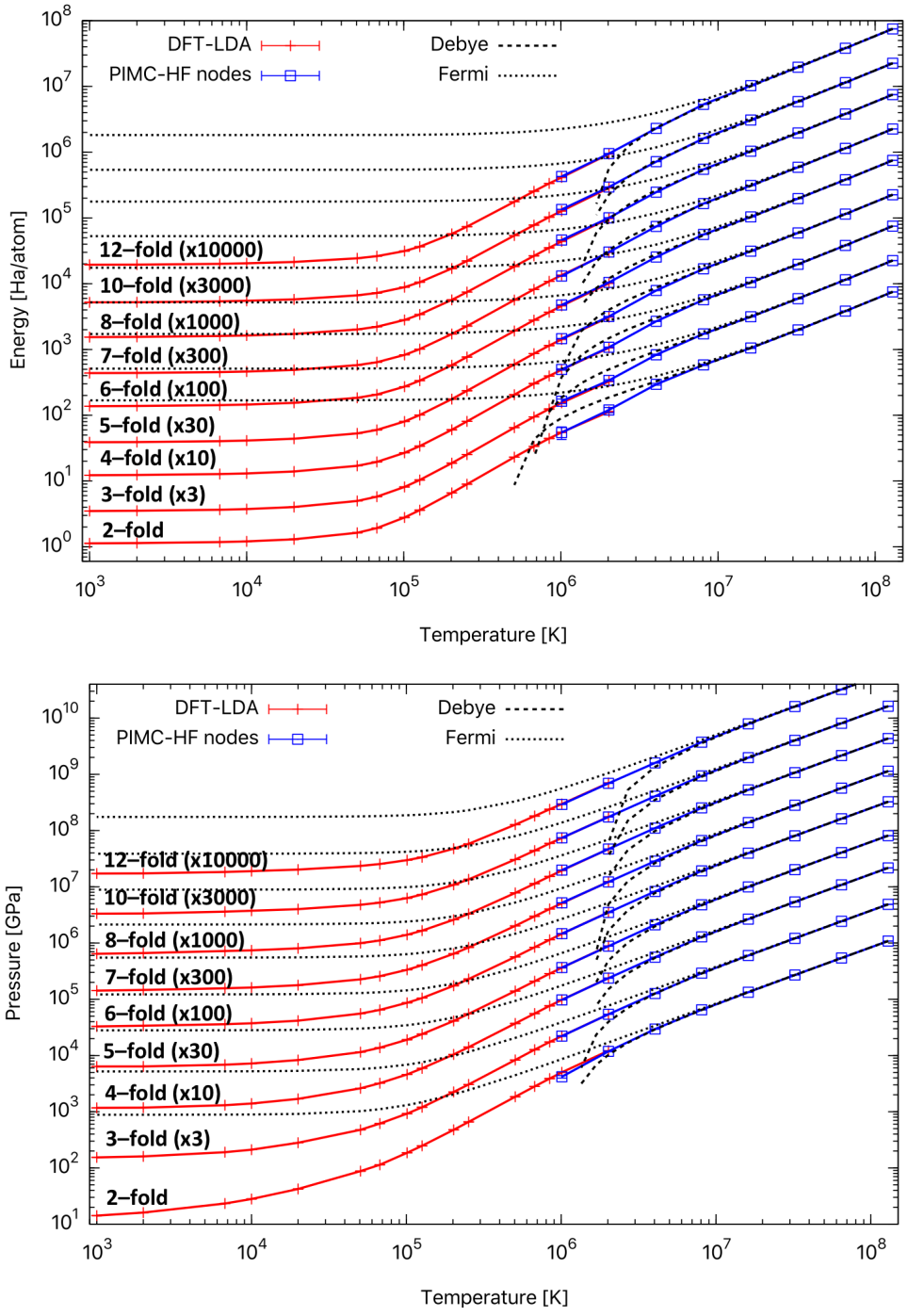

Figure 5.3: Energies and pressures of a 8-Na system along nine isochores (2, $\cdots$, 12-fold compression) from first-principles (DFT and PIMC) computations and modeling (Debye-Hückel theory or Fermi gas model). The energies (after shifting up by 162.5 Ha/atom) and the pressures have been multiplied by integers (shown in parentheses) for clarity of the plotting. The agreements of PIMC with DFT at 10^6 K, and with analytic models above 2×10^7 K, are remarkable.

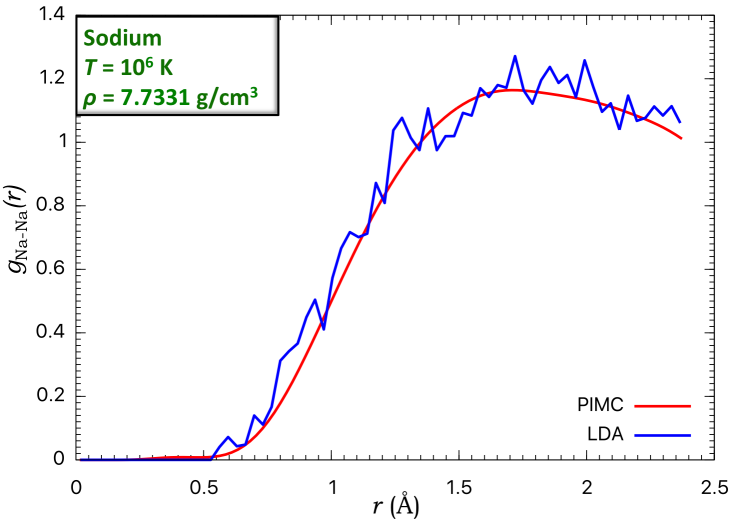

Figure 5.4: Comparison of the nuclear pair correlation function obtained from DFT-MD (LDA) and PIMC for 8-atom simulation cells at 10^6 K and under 8-fold compression.

Shock compression

Shock waves are used for many high pressure and temperature studies. Due to conservation of mass, momentum, and energy, a steady shock follows the Rankine-Hugoniot equation [30]

$$(E - E_0) + \frac{1}{2}(P + P_0)(V - V_0) = 0, \tag{5.5}$$

where (E_0, P_0, V_0) represents the internal energy, pressure, and volume of the initial state. The grid of E-P-V data obtained above allows one to estimate the Hugoniot curves by fitting E and P as functions of T and V.

Considering that samples in shock experiments may be pre-compressed for reaching the interesting locus of states off the principle Hugoniot, here we consider four different initial conditions corresponding to 0.75-, 1.0-, 1.5-, and 2.0-fold (relative to ρ_{ambient}, the ambient density of a body-centered cubic structure [169]) pre-compressions. DFT simulations are performed at each of these densities to determined the corresponding pressures and internal energies. The calculated initial conditions are listed in Table 5.2.

We calculated the Hugoniot curves and represented them with pressure-density (P-ρ) and pressure-temperature (P-T) plots in Fig. 5.5. Two scenarios obtained from the SESAME[3] database [170] are also shown for comparison, corresponding to initial conditions ($\rho_0 = 0.96999$ g/cm^3 $\approx \rho_{\text{ambient}}, E_0 = -7.055 \times 10^{-9}$ Ha/atom, $P_0 = 10^{-5}$ GPa) and ($\rho_0 = 1.93999$ g/cm^3 $\approx 2\rho_{\text{ambient}}, E_0 = 1.912 \times 10^{-2}$ Ha/atom, $P_0 = 16.68873$ GPa) for "1.0,SESAME" and "2.0,SESAME", respectively.

[3]SESAME is a tabular database for the thermodynamic properties of materials. It is constructed by connecting available shock wave data with Thomas-Fermi-Dirac theory and Mie-Grüneisen theory at high densities, and some simple analytic form at low densities.

Table 5.2: Four different initial conditions for determining the Hugoniot equations considered in this work. The energy and pressure values are from DFT calculations of a body-centered cubic structure [169].

ρ/ρ_0	ρ_0[g/cm^3]	V_0[Å^3/atom]	E_0[Ha/atom]	P_0[GPa]
0.75	0.72497	52.65780749	-161.3850268	-1.728
1.00	0.96663	39.49335562	-161.3900007	-1.075
1.50	1.44995	26.32890375	-161.3889424	3.422
2.00	1.93326	19.74667781	-161.3781935	12.958

In the high-temperature limit, the system is near-fully ionized and close to uniform electron gas that can be well described by the Thomas-Fermi-Dirac theory, as is shown by the remarkable consistency between SESAME and our present first-principles calculations at $T > 2 \times 10^7$ K. However, at lower temperatures when the system includes complicated electron-electron and electron-ion interactions, SESAME becomes deficient and only exhibits one density peak along each Hugoniot, whereas our accurate first-principles calculations predict two peaks. One of the peaks appears at $T < 10^6$, when DFT-MD works, and the other above 2×10^6 K when DFT-MD has become too inefficient and PIMC is important in obtaining the feature.

The above findings are also shown in Fig. 5.6 by plotting T and P as functions of the compression ratio ρ/ρ_0. When the initial density is the lowest ($\rho_0 = 0.75\rho_{\text{ambient}}$), a maximum compression ratio of ∼5.6 is reached at $T < 10^6$ K. The value of this peak decreases with ρ_0, and reduces to 4.7 when $\rho_0 = 2.0\rho_{\text{ambient}}$, with which the other peak at higher temperature has slightly larger compression ratio (4.9). In the high-pressure, temperature limit, the compression ratio approximates 4 (the ideal Fermi electron gas limit), regardless of the initial density. This is because the system are fully ionized and the kinetic energy dominates over the potential energy.

5.4 Discussion

According to tests on different methods to generate atomic orbitals in PIMC, we see no advantage in using any DFT method over deriving the atomic orbitals with Hartree-Fock methods. Also using a small number of atomic orbitals (between 6 and 13) that are expressed in a relatively simple basis (such as 6-31G) yields sufficiently accurate PIMC results.

We show that the applicability of DFT-MD within LDA and GGA-PBE at $T > 2 \times 10^6$ K is invalidated, because the K-shell that is frozen by pseudopotentials should have been partially ionized. When $T < 2 \times 10^6$ K, PIMC with HF nodes yields remarkable agreement with DFT-MD predictions, whereas energies from PIMC with FP nodes are systematically too high, suggesting that FP nodes do not lead to the correct shell structure in the atom.

At 10^6 K, our PIMC simulations with localized, HF nodes bridge with DFT-MD in

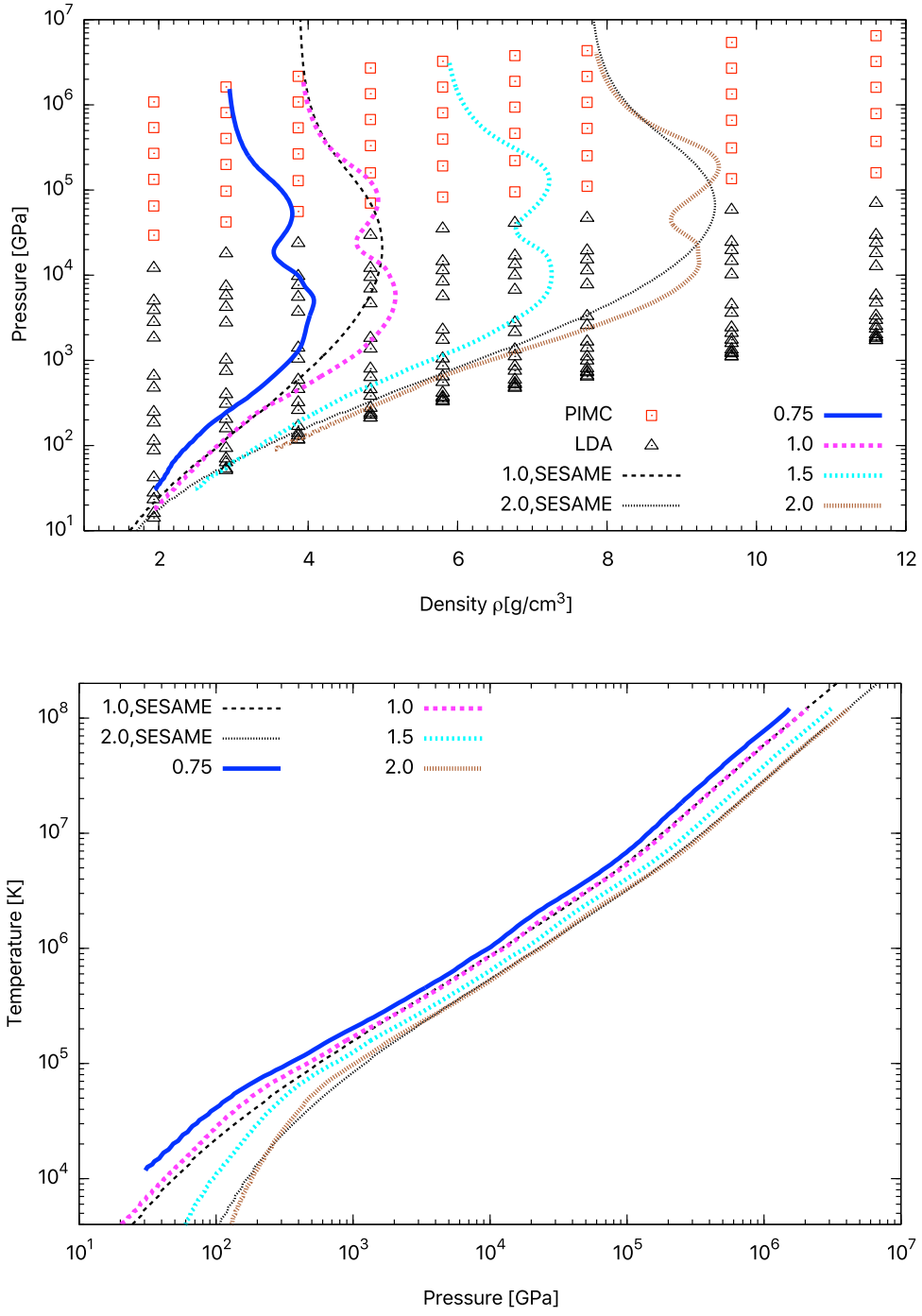

Figure 5.5: Shock Hugoniot curves (colored lines) corresponding to four different initial densities 0.75-, 1.0-, 1.5-, and 2-times ρ_{ambient}. In the upper panel, red squares and dark triangles represent the pressure and density conditions of our PIMC and DFT-MD simulations, respectively.

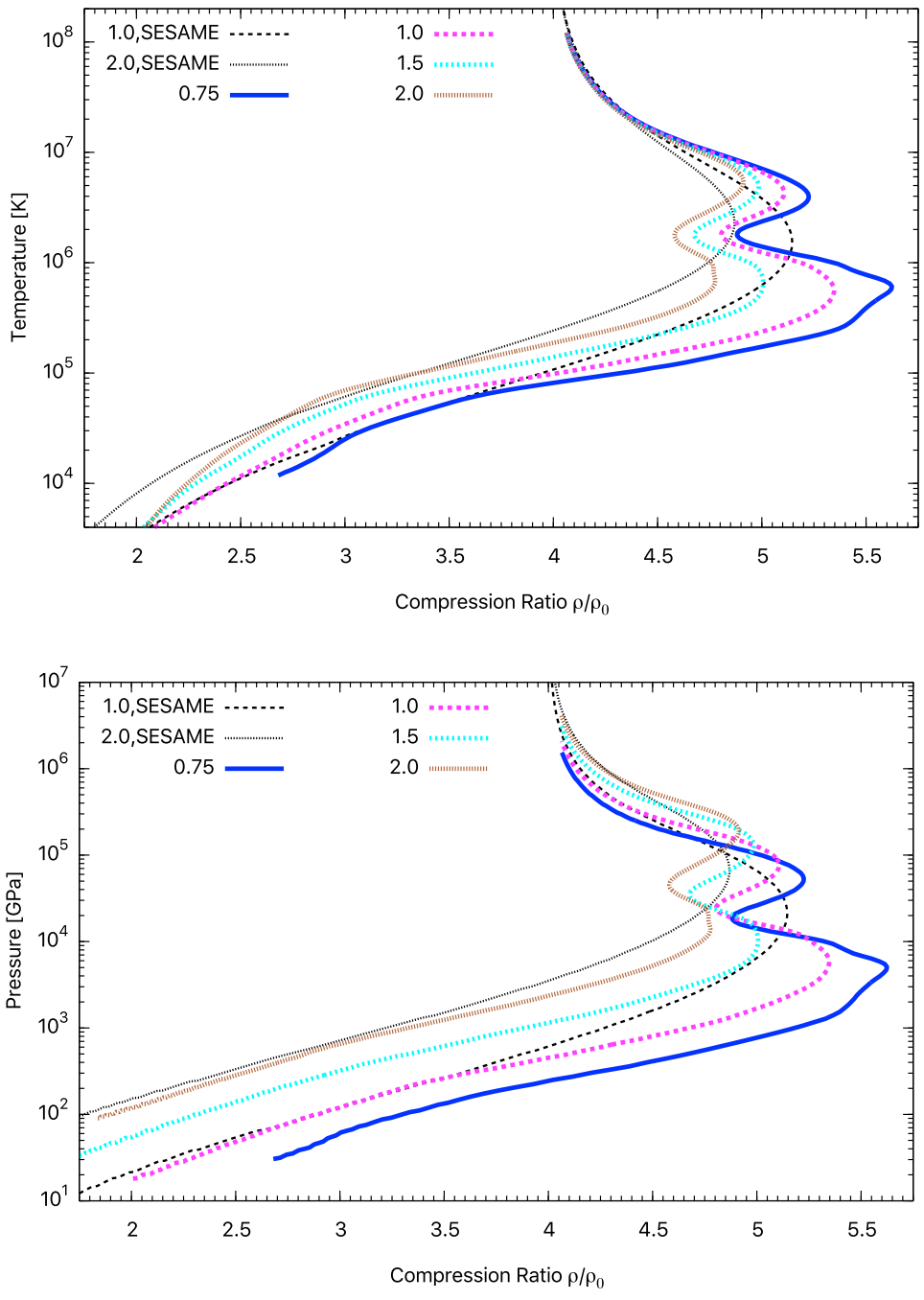

Figure 5.6: Compression ratio and temperature or pressure relations along four shock Hugoniot curves (colored lines) corresponding to four different initial densities 0.75-, 1.0-, 1.5-, and 2-times ρ_{ambient}.

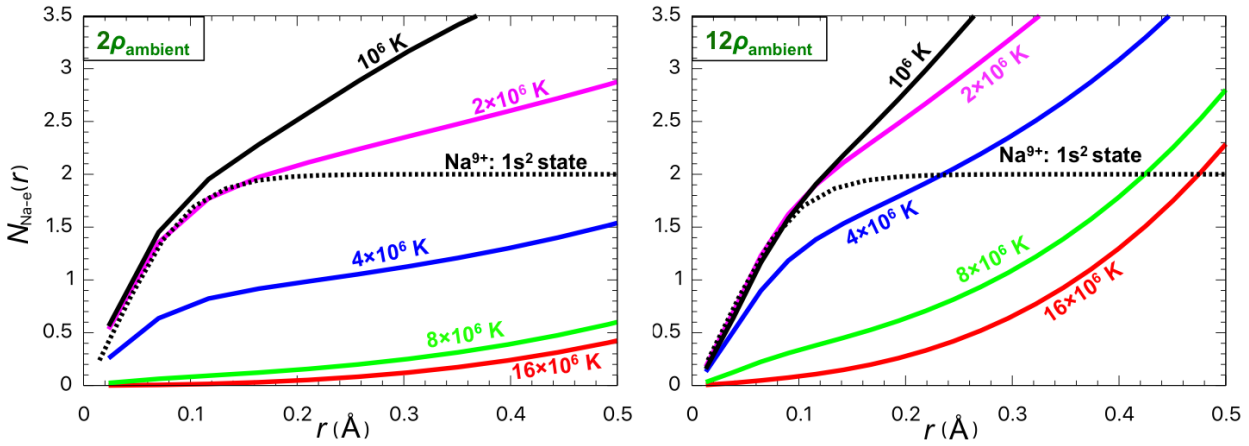

Figure 5.7: Number of electrons near the nucleus at two densities and a series of temperatures. The profile of the $1s^2$ electronic state of Na^{9+} (helium-like ion with $Z = 11$, calculated with GAMESS), is also shown for comparison.

energy, pressure, and ionic structure. We have thus been able to construct a coherent first-principles EOS table for warm dense sodium, in a wide range of density (2-12 ρ_{ambient}) and temperatures (10^3-1.29×10^8 K). The difference between PIMC and DFT-MD is typically less than 3 Ha/atom in internal energy and within 3% in pressure.

The EOS data allow us to construct shock compression Hugoniots. Similar to Si [51], Ne [50], and O [49], two density peaks are predicted along each of the Hugoniot curves—one at below 10^6 K, for which DFT-MD works fine; the other above 2×10^6 K, for which PIMC is important. Compression ratio of $\sim$5 can be reached with initial density between 0.75- and 1.5-times ambient density.

The origin of the peaks can be explained by different stages of electron ionization. Figure 5.7 compares the number of electrons near the nucleus $N(r)$ with that of a helium-like ion Na^{9+} (calculated with GAMESS) at two densities and a series of temperatures. The results show that $N(r)$ decreases with T, indicating the gradual ionization of the atoms with temperature. The 1s electrons become excited at over 2×10^6 K. This indicates that the upper peak along the Hugoniots in Figs. 5.5 and 5.6 is related to the ionization of the 1s electrons, while the lower peak correspond to the ionization of outer-shell electrons. The multi-peak feature of compression along Hugoniots is determined by the ionization process and interaction effects, as has been discussed in details previously in [48]. SESAME does not consider sufficient electronic shell information, thus the peaks have been merged. Similar multi-peak features are also found in other EOS models that better account for Coulomb interactions or electronic configurations [171].

5.5 Appendix: EOS table of sodium

Table 5.3: EOS table of sodium from DFT-MD (LDA) and PIMC simulations in this work. The data are based on simulations on 8-atom cells unless otherwise specified.

ρ [g/cm^3]	T [K]	E [Ha/atom]	$\sigma(E)$ [Ha/atom]	P [GPa]	$\sigma(P)$ [GPa]	Method
1.93328†	1000.00	-161.373275	0.000456	14.1876	0.0541	LDA
1.93328†	2000.00	-161.362200	0.000660	16.0868	0.0671	LDA
1.93328†	6736.47	-161.321127	0.001111	23.3239	0.1872	LDA
1.93328†	10000.00	-161.292271	0.001864	28.0283	0.2268	LDA
1.93328†	20000.00	-161.200020	0.001905	42.2836	0.3131	LDA
1.93328	50523.50	-160.866617	0.001832	87.7294	0.5980	LDA
1.93328	67364.70	-160.578654	0.001404	113.6573	0.6299	LDA
1.93328	101047.00	-159.710769	0.001477	185.9401	1.3009	LDA
1.93328	126309.00	-158.894894	0.001986	247.3363	1.4924	LDA
1.93328	202095.00	-155.904890	0.001458	477.1452	0.9449	LDA
1.93328	252619.00	-153.559287	0.002389	659.3251	0.8812	LDA
1.93328	505239.00	-139.389141	0.012724	1842.3810	2.9380	LDA
1.93328	673652.60	-128.866887	0.036004	2843.2556	3.3124	LDA
1.93328	842065.80	-118.079891	0.003260	3859.0165	1.0447	LDA
1.93328	1010479.00	-107.529075	0.009934	5021.0920	4.7770	LDA
1.93328	2020958.00	-49.310792	0.111457	12166.1570	11.0920	LDA
1.93328	1010479	-107.928000	1.466000	4186.7000	216.1000	PIMC
1.93328	2020958	-42.076000	1.368000	11839.1000	201.4000	PIMC
1.93328	4041916	133.096000	1.199000	29481.7000	173.0000	PIMC
1.93328	8083831	420.284000	1.536000	64923.1000	225.7000	PIMC
1.93328	16167663	891.233000	2.071000	133306.5000	304.7000	PIMC
1.93328	32335325	1821.117000	2.779000	269840.0000	408.8000	PIMC
1.93328	64670651	3665.296000	3.288000	541096.5000	483.7000	PIMC
1.93328	129341301	7348.466000	3.249000	1083108.6000	478.2000	PIMC
2.89991†	1000.00	-161.333561	0.000397	51.3638	0.0581	LDA
2.89991†	2000.00	-161.322609	0.000294	53.4171	0.0370	LDA
2.89991†	6736.47	-161.280860	0.000612	63.4892	0.1889	LDA
2.89991†	10000.00	-161.253520	0.002084	70.3387	0.2872	LDA
2.89991†	20000.00	-161.158054	0.002469	93.4420	0.6721	LDA
2.89991	50523.50	-160.840667	0.002068	158.9335	1.0288	LDA
2.89991	67364.70	-160.574006	0.003453	205.1694	2.4130	LDA
2.89991	101047.00	-159.789638	0.002568	308.2577	1.6962	LDA
2.89991	126309.00	-159.041984	0.001963	400.0095	1.7858	LDA
2.89991	202095.00	-156.266956	0.002523	749.3564	4.8675	LDA

Table 5.3: ... continued

ρ [g/cm^3]	T [K]	E [Ha/atom]	$\sigma(E)$ [Ha/atom]	P [GPa]	$\sigma(P)$ [GPa]	Method
2.89991	252619.00	-154.093419	0.002406	1018.8557	2.3969	LDA
2.89991	505239.00	-140.906184	0.032725	2777.2213	10.2005	LDA
2.89991	673652.60	-131.069015	0.035519	4228.9316	8.5763	LDA
2.89991	842065.80	-121.024323	0.018003	5784.8852	9.5901	LDA
2.89991	1010479.00	-110.930244	0.010290	7395.9040	7.4640	LDA
2.89991	2020958.00	-53.499534	0.119828	18023.6060	18.7930	LDA
2.89991	1010479	-108.043000	1.621000	7365.2000	357.9000	PIMC
2.89991	2020958	-49.507000	1.057000	18024.4000	232.9000	PIMC
2.89991	4041916	114.364000	2.287000	42176.3000	503.4000	PIMC
2.89991	8083831	413.799000	1.913000	96966.9000	421.7000	PIMC
2.89991	16167663	887.261000	2.200000	199649.9000	485.3000	PIMC
2.89991	32335325	1813.266000	2.373000	403512.5000	523.4000	PIMC
2.89991	64670651	3663.550000	3.245000	811666.6000	716.4000	PIMC
2.89991	129341301	7341.000000	3.262000	1623370.4000	720.0000	PIMC
3.86655†	1000.00	-161.275576	0.000156	116.9225	0.0550	LDA
3.86655†	2000.00	-161.265118	0.000315	118.2260	0.0890	LDA
3.86655†	6736.47	-161.224402	0.000389	130.4228	0.2524	LDA
3.86655†	10000.00	-161.195763	0.000735	139.8094	0.1861	LDA
3.86655†	20000.00	-161.102626	0.000945	169.2074	0.4102	LDA
3.86655†	50523.50	-160.795842	0.002210	260.5405	1.2539	LDA
3.86655†	67364.70	-160.547697	0.002755	321.5188	1.1030	LDA
3.86655	101047.00	-159.814659	0.002783	460.1099	3.0158	LDA
3.86655	126309.00	-159.105042	0.000838	590.2279	1.3041	LDA
3.86655	202095.00	-156.487644	0.001192	1044.7998	1.6831	LDA
3.86655	252619.00	-154.431237	0.002116	1405.4943	2.3236	LDA
3.86655	505239.00	-141.974946	0.020770	3709.9242	6.7351	LDA
3.86655	673652.60	-132.206248	0.401475	5560.8565	12.5634	LDA
3.86655	842065.80	-122.907708	0.029601	7639.4047	17.4958	LDA
3.86655	1010479.00	-113.282048	0.011095	9774.1780	11.3550	LDA
3.86655	2020958.00	-56.688022	0.106933	23800.9490	25.1370	LDA
3.86655	1010479	-112.837000	1.404000	9741.0000	413.4000	PIMC
3.86655	2020958	-54.435000	0.975000	23691.9000	286.6000	PIMC
3.86655	4041916	105.927000	1.580000	55999.8000	461.7000	PIMC
3.86655	8083831	407.996000	1.262000	128739.0000	369.7000	PIMC
3.86655	16167663	884.363000	1.232000	266032.3000	361.0000	PIMC
3.86655	32335325	1810.725000	1.605000	537764.9000	471.0000	PIMC
3.86655	64670651	3658.639000	1.579000	1081196.1000	464.4000	PIMC

Table 5.3: ... continued

ρ [g/cm^3]	T [K]	E [Ha/atom]	$\sigma(E)$ [Ha/atom]	P [GPa]	$\sigma(P)$ [GPa]	Method
3.86655	129341301	7344.554000	1.477000	2165931.0000	434.2000	PIMC
4.83319†	1000.00	-161.203737	0.000098	212.6039	0.2430	LDA
4.83319†	2000.00	-161.195523	0.000146	212.9332	0.1787	LDA
4.83319†	6736.47	-161.154966	0.000431	228.4419	0.3922	LDA
4.83319†	10000.00	-161.125579	0.001636	239.8965	0.6217	LDA
4.83319†	20000.00	-161.034761	0.001073	276.5173	0.6824	LDA
4.83319	50523.50	-160.733750	0.002195	382.6727	2.0613	LDA
4.83319	67364.70	-160.506200	0.003237	457.7738	2.9670	LDA
4.83319	101047.00	-159.817730	0.001786	635.3526	2.5712	LDA
4.83319	126309.00	-159.138778	0.002212	799.2979	2.2130	LDA
4.83319	202095.00	-156.634007	0.002631	1371.4686	4.5015	LDA
4.83319	252619.00	-154.651350	0.004644	1833.6730	5.6729	LDA
4.83319	505239.00	-142.736283	0.023464	4667.5389	9.7123	LDA
4.83319	673652.60	-133.660154	0.063295	6966.3249	20.4804	LDA
4.83319	842065.80	-124.326376	0.052830	9510.2093	16.4176	LDA
4.83319	1010479.00	-115.048431	0.015076	12147.2890	13.8150	LDA
4.83319	2020958.00	-59.112353	0.102383	29593.8910	29.7360	LDA
4.83319	1010479	-113.790000	1.047000	12194.9000	385.3000	PIMC
4.83319	2020958	-56.613000	1.199000	29277.6000	440.4000	PIMC
4.83319	4041916	100.467000	2.484000	70264.4000	910.9000	PIMC
4.83319	8083831	399.428000	1.981000	159313.5000	727.7000	PIMC
4.83319	16167663	880.477000	1.513000	331849.8000	556.0000	PIMC
4.83319	32335325	1811.084000	2.526000	672886.5000	929.4000	PIMC
4.83319	64670651	3659.214000	3.406000	1352187.1000	1253.6000	PIMC
4.83319	129341301	7346.945000	2.890000	2708695.7000	1062.4000	PIMC
5.79983†	1000.00	-161.125429	0.000487	328.7436	0.3694	LDA
5.79983†	2000.00	-161.115826	0.000289	338.4720	0.3474	LDA
5.79983†	6736.47	-161.075166	0.000401	359.9758	0.3740	LDA
5.79983†	10000.00	-161.047235	0.000434	373.4672	0.3449	LDA
5.79983†	20000.00	-160.957149	0.000735	416.0938	0.8103	LDA
5.79983†	50523.50	-160.657429	0.001638	555.7379	1.7658	LDA
5.79983†	67364.70	-160.434619	0.003296	647.4362	2.1403	LDA
5.79983†	101047.00	-159.781362	0.004000	864.5054	4.3322	LDA
5.79983†	126309.00	-159.143328	0.002100	1050.7955	2.8038	LDA
5.79983	202095.00	-156.730181	0.002142	1737.7634	5.7041	LDA
5.79983	252619.00	-154.823970	0.004699	2291.0427	9.8892	LDA
5.79983	505239.00	-143.380682	0.005503	5666.8484	7.0430	LDA

Table 5.3: ... continued

ρ [g/cm^3]	T [K]	E [Ha/atom]	$\sigma(E)$ [Ha/atom]	P [GPa]	$\sigma(P)$ [GPa]	Method
5.79983	673652.60	-134.572287	0.055685	8416.5223	31.2485	LDA
5.79983	842065.80	-125.665986	0.004054	11399.8957	6.5393	LDA
5.79983	1010479.00	-116.415830	0.010256	14577.4350	13.1800	LDA
5.79983	2020958.00	-61.336567	0.083924	35301.2550	31.6920	LDA
5.79983	1010479	-114.963000	1.438000	14648.5000	635.4000	PIMC
5.79983	2020958	-57.820000	1.193000	34903.1000	526.2000	PIMC
5.79983	4041916	91.600000	1.331000	82799.3000	585.8000	PIMC
5.79983	8083831	398.388000	1.628000	191986.3000	716.4000	PIMC
5.79983	16167663	875.024000	2.209000	396585.5000	974.0000	PIMC
5.79983	32335325	1807.732000	4.481000	806579.0000	1979.7000	PIMC
5.79983	64670651	3650.708000	2.687000	1619342.8000	1187.8000	PIMC
5.79983	129341301	7346.342000	2.512000	3250600.0000	1109.0000	PIMC
6.76647†	1000.00	-161.041754	0.001034	474.4666	0.5016	LDA
6.76647†	2000.00	-161.031768	0.001035	487.3729	0.6567	LDA
6.76647†	6736.47	-160.989065	0.000440	521.8808	0.5912	LDA
6.76647†	10000.00	-160.960549	0.001025	539.0450	1.0636	LDA
6.76647†	20000.00	-160.868810	0.000919	593.0557	1.1222	LDA
6.76647†	50523.50	-160.573855	0.001469	753.9158	2.4722	LDA
6.76647†	67364.70	-160.366543	0.002332	856.3814	3.5047	LDA
6.76647†	101047.00	-159.739601	0.003530	1113.7496	4.4413	LDA
6.76647†	126309.00	-159.121090	0.003634	1343.0674	5.6181	LDA
6.76647	202095.00	-156.770932	0.011403	2147.0417	13.5065	LDA
6.76647	252619.00	-154.944088	0.009756	2778.1610	14.4336	LDA
6.76647	505239.00	-143.694337	0.034418	6733.2303	19.0564	LDA
6.76647	673652.60	-135.129505	0.049150	9962.9638	38.8526	LDA
6.76647	842065.80	-126.260046	0.051156	13441.2436	31.0371	LDA
6.76647	1010479.00	-117.549454	0.016441	17002.3890	18.5200	LDA
6.76647	2020958.00	-63.004967	0.096921	41092.7670	43.1560	LDA
6.76647	1010479	-118.892000	1.531000	17293.2000	771.5000	PIMC
6.76647	2020958	-61.554000	1.340000	40659.1000	689.6000	PIMC
6.76647	4041916	85.169000	1.252000	95152.3000	638.5000	PIMC
6.76647	8083831	389.835000	1.701000	221303.2000	869.9000	PIMC
6.76647	16167663	874.035000	2.116000	462980.9000	1088.5000	PIMC
6.76647	32335325	1804.170000	2.445000	939844.6000	1260.7000	PIMC
6.76647	64670651	3650.494000	3.341000	1889667.5000	1721.9000	PIMC
6.76647	129341301	7341.374000	3.275000	3790282.6000	1688.2000	PIMC
7.73310†	1000.00	-160.956118	0.001444	643.0967	0.6172	LDA

Table 5.3: ... continued

ρ [g/cm^3]	T [K]	E [Ha/atom]	$\sigma(E)$ [Ha/atom]	P [GPa]	$\sigma(P)$ [GPa]	Method
7.73310†	2000.00	-160.944004	0.001589	663.2929	0.9916	LDA
7.73310†	6736.47	-160.895773	0.000482	720.7726	0.7223	LDA
7.73310†	10000.00	-160.867530	0.000559	741.0072	0.8062	LDA
7.73310†	20000.00	-160.775532	0.000883	804.3878	1.2888	LDA
7.73310†	50523.50	-160.483902	0.002176	994.0541	2.6511	LDA
7.73310†	67364.70	-160.283598	0.004164	1111.2320	5.2549	LDA
7.73310†	101047.00	-159.689190	0.002430	1399.1140	4.1664	LDA
7.73310†	126309.00	-159.091287	0.003823	1659.0481	4.6762	LDA
7.73310	202095.00	-156.819661	0.001960	2591.9315	4.2549	LDA
7.73310	252619.00	-155.037328	0.003585	3303.7522	8.3595	LDA
7.73310	505239.00	-144.219935	0.005683	7780.2687	11.7932	LDA
7.73310	673652.60	-136.000577	0.007023	11381.4358	12.8701	LDA
7.73310	842065.80	-127.367914	0.014046	15308.8086	28.9460	LDA
7.73310	1010479.00	-118.467497	0.012484	19520.2510	15.4230	LDA
7.73310	2020958.00	-64.232611	0.095180	46973.5420	48.7520	LDA
7.73310	1010479	-116.336000	1.221000	19794.1000	723.4000	PIMC
7.73310	2020958	-61.990000	1.084000	46898.8000	638.5000	PIMC
7.73310	4041916	84.563000	1.554000	110719.3000	910.5000	PIMC
7.73310	8083831	387.232000	0.986000	252891.3000	576.0000	PIMC
7.73310	16167663	872.869000	1.256000	529362.0000	740.0000	PIMC
7.73310	32335325	1797.875000	1.441000	1071009.1000	846.2000	PIMC
7.73310	64670651	3647.683000	2.036000	2158572.2000	1196.0000	PIMC
7.73310	129341301	7338.912000	1.907000	4330748.7000	1119.1000	PIMC
9.66638†	1000.00	-160.763329	0.002281	1108.9544	1.7427	LDA
9.66638†	2000.00	-160.757751	0.002238	1117.9050	0.9820	LDA
9.66638†	6736.47	-160.700623	0.000838	1206.3649	1.2929	LDA
9.66638†	10000.00	-160.666544	0.000547	1249.4653	1.1191	LDA
9.66638†	20000.00	-160.574934	0.001132	1335.6529	2.3048	LDA
9.66638†	50523.50	-160.281609	0.001445	1593.0760	2.4184	LDA
9.66638†	67364.70	-160.092017	0.002154	1743.4288	4.5795	LDA
9.66638†	101047.00	-159.547589	0.003760	2095.2938	6.3452	LDA
9.66638†	126309.00	-158.981276	0.003366	2430.6113	4.3911	LDA
9.66638†	202095.00	-156.820222	0.005199	3612.0554	9.1592	LDA
9.66638	252619.00	-155.096642	0.008258	4514.5875	19.2810	LDA
9.66638	505239.00	-144.483554	0.037575	10200.1580	29.5964	LDA
9.66638	673652.60	-136.568063	0.038936	14670.0977	31.5179	LDA
9.66638	842065.80	-128.155594	0.068417	19669.8582	31.4497	LDA

Table 5.3: ... continued

ρ [g/cm^3]	T [K]	E [Ha/atom]	$\sigma(E)$ [Ha/atom]	P [GPa]	$\sigma(P)$ [GPa]	Method
9.66638	1010479.00	-119.969866	0.016834	24565.0420	27.6270	LDA
9.66638	2020958.00	-66.861995	0.058230	58584.1410	41.2640	LDA
9.66638	1010479	-117.575000	1.432000	24725.0000	1054.7000	PIMC
9.66638	2020958	-64.105000	1.254000	58060.7000	924.1000	PIMC
9.66638	4041916	76.621000	1.275000	136020.9000	929.0000	PIMC
9.66638	8083831	377.813000	0.993000	312790.2000	723.3000	PIMC
9.66638	16167663	866.507000	1.095000	659064.1000	804.5000	PIMC
9.66638	32335325	1799.394000	1.222000	1341369.2000	899.4000	PIMC
9.66638	64670651	3643.026000	1.696000	2695921.6000	1248.4000	PIMC
9.66638	129341301	7332.346000	1.663000	5409701.9000	1224.5000	PIMC
11.59965[†]	1000.00	-160.556691	0.002603	1719.9465	0.6790	LDA
11.59965[†]	2000.00	-160.549624	0.002687	1734.4533	0.6942	LDA
11.59965[†]	6736.47	-160.494142	0.001451	1833.0641	1.5908	LDA
11.59965[†]	10000.00	-160.454046	0.000783	1897.7867	1.0451	LDA
11.59965[†]	20000.00	-160.355545	0.001170	2022.3007	1.5306	LDA
11.59965[†]	50523.50	-160.063500	0.001899	2349.8379	4.2682	LDA
11.59965[†]	67364.70	-159.876707	0.001938	2540.6714	4.3457	LDA
11.59965[†]	101047.00	-159.363492	0.003447	2974.5097	4.9778	LDA
11.59965[†]	126309.00	-158.840330	0.003573	3347.3112	6.4394	LDA
11.59965[†]	202095.00	-156.770616	0.004559	4761.0257	8.5925	LDA
11.59965	252619.00	-155.119359	0.024345	5807.0426	23.9536	LDA
11.59965	505239.00	-144.891864	0.052034	12747.5746	44.6722	LDA
11.59965	673652.60	-137.045917	0.052582	18128.3780	35.0137	LDA
11.59965	842065.80	-128.968403	0.071694	23913.8340	60.2987	LDA
11.59965	1010479.00	-121.152641	0.013657	29716.0040	28.9940	LDA
11.59965	2020958.00	-68.870947	0.131268	70310.0410	114.6000	LDA
11.59965	1010479	-119.776000	1.794000	29143.8000	1584.5000	PIMC
11.59965	2020958	-67.258000	1.296000	69127.9000	1145.1000	PIMC
11.59965	4041916	67.656000	1.748000	159648.2000	1545.8000	PIMC
11.59965	8083831	370.894000	1.201000	372985.2000	1047.7000	PIMC
11.59965	16167663	863.496000	1.446000	790329.6000	1275.7000	PIMC
11.59965	32335325	1795.869000	1.694000	1608152.2000	1496.3000	PIMC
11.59965	64670651	3642.936000	2.232000	3236363.8000	1971.2000	PIMC
11.59965	129341301	7333.173000	2.321000	6493496.8000	2051.3000	PIMC

[†]54-atom cell.

Chapter 6

Outlook

The work of the Revolution is not yet done, let all our comrades strive on for their consummation. - Sun Yat-sen

First-principles methods have been shown to be useful in studies of Earth and planetary materials. Not only the phase relations and equation of state can be accurately determined, but also many interesting properties of materials at high pressure that are very difficult to measure in the lab, such as viscosity, diffusivity, and structure factors, which simply require autocorrelation analysis of quantities, such as the stress, velocity, and electron density, acquired from the outputs of density functional theory-based molecular dynamics (DFT-MD) simulations, can be readily calculated. This makes the DFT-MD simulations powerful and worthwhile tools for predictions as well as the guidance to design of experiments.

There are many interesting questions regarding the formation and evolution, and structure and dynamics, of the Earth, other planets, and their moons. Aside from those described in Sec. 1.2 and explored in Chapters 3-5, some other exciting topics have also become eye-catching. For example, the giant impacts that may have re-shaped the Earth and formed the Moon, evolution of the early magma ocean that is related to the formation and growth of the core and powering of the geodynamo, interior structure of the Jovian and extrasolar planets. Frontiers of research in these aspects have called for accurate knowledge of how major planet-forming materials (e.g., iron and silicates) behave, mix, and transform, i.e., their physical properties and phase relations, under various temperature, pressure conditions [172]. Fortunately, the progress in computer science and technology, simulation methods, and experimental technologies in recent decades have opened more doors toward this end. It has also become possible to consider and re-evaluate problems that were difficult or impossible to tackle in the past. To name a few, water solubility in the lower mantle, and noble gas partitioning during magma-ocean crystallization.

Water solubility in the lower mantle. The Earth's lower mantle could store water that is either primordial [173] or transported from the surface via subduction [174]. The existence of water could lower the melting temperature, seismic velocities, and viscosity of minerals, which are important in understanding the temperature and composition profiles of the lower

mantle and the convection that drives plate tectonics. Despite progresses [175, 176, 177] in studying the dense hydrous magnesium silicates (phases D and H), the solubility of water in major lower-mantle minerals, including bridgmanite, post-bridgmanite, and ferropericlase, is uncertain with large discrepancies between studies (see [178] and Table 21.1 in [177]). This could be studied with accurate Gibbs free energy calculations on reactions such as

$$(\mathrm{Fe/Al\text{-}})\mathrm{MgSiO_3}\ (\mathrm{liquid}) + \mathrm{H_2O}\ (\mathrm{liquid}) \Leftrightarrow (\mathrm{Fe/Al\text{-}})\mathrm{MgSiO_3{:}H_2O}\ (\mathrm{liquid}), \tag{6.1}$$

which is related to the solubility of water during and after the cooling of a magma ocean. DFT-MD based thermodynamic integration methods provide an option for such calculations, and similar methods have been implemented on the solubility of rock material in Jupiter's core [179] and the equation of states of superionic and liquid water in Neptune and Uranus [12, 13].

Noble gas partitioning during magma-ocean crystallization. Noble gas isotopes provide important signatures to constrain the evolution of the Earth. For example, ^{3}He and ^{20,22}Ne in oceanic island basalts are thought to originate from dense primordial piles at the bottom of the lower mantle where they were trapped upon cooling of the early magma ocean. A modest amount of these isotopes is entrained from sources of hotspots toward the surface by mantle convection [180, 181]. Another important example of interest is the well-known Xe paradox. The Earth's atmosphere is strongly depleted in xenon, especially ^{129}Xe [182], which could suggest that the Earth experienced extensive loss of its primordial atmosphere, and subsequent degassing of the lower mantle transferred little Xe in the modern atmosphere [183]. Several mechanisms have been proposed to reconcile the Xe paradox, including seawater subduction [184], Xe entrapment by zeolites [185], weakly siderophile behavior of iodine [186], and Xe alloying with iron and nickel in the inner core [187, 188, 189]. However, direct mineralogical evidence of these mechanisms is still lacking. First-principles calculations are feasible in studying the partitioning of elements between solids and melts, providing a means to study the noble gas problems.

Ideas of multi-scale simulations, by integrating standard first-principles methods with macroscopic computational techniques to consider the joint effects of textures, defects, grain boundaries, coexisting phases, etc., are other important directions for work.

It should be minded that theoretical models involve approximations, such as the form of the exchange-correlation functional and pseudopotentials in DFT simulations, as have been discussed in Chapter 2. Similarly, diamond-anvil cell experiments entail non-hydrostaticity when reaching high pressures, because none of the practical pressure mediums is ideally soft when pressure exceeds some 10s GPa [190], and Soret diffusion in large temperature gradients during laser heating [191]. Therefore, proper modeling, strong symbiosis with careful experiments, and interplay with other disciplines, such as physics and materials sciences for new computational and experimental techniques, or geochemistry, biology, environmental science, and planetary science on evolution of life and the universe, is important for achieving major progresses.

Bibliography

[1] S. Karato, *The Dynamic Structure of the Deep Earth: An Interdisciplinary Approach*. Princeton and Oxford: Princeton University Press, 2003.

[2] M. J. Gillan, D. Alfè, J. Brodholt, L. Vočadlo, and G. D. Price, "First-principles modelling of Earth and planetary materials at high pressures and temperatures," *Rep. Prog. Phys.*, vol. 69, pp. 2365–2441, 2006.

[3] F. Birch, "Elasticity and constitution of the Earth's interior," *J. Geophys. Res.*, vol. 57, pp. 227–286, 1952.

[4] Mcdonough, W. F. and Sun, S.-s., "The Composition of the Earth," *Chem. Geol.*, vol. 120, pp. 223–253, 1995.

[5] R. Jeanloz, "Earth's Mantle (Geophysics)," in *Ency Phys. Sci. Technol.* (R. A. Meyers, ed.), vol. 4, ch. 4, pp. 783–799, Academic Press, New York, 3 ed., 2001.

[6] R. G. Trønnes, "Structure, mineralogy and dynamics of the lowermost mantle," *Mineral. Petrol.*, vol. 99, pp. 243–261, 2010.

[7] M. Mattesini, A. B. Belonoshko, E. Buforn, M. Ramírez, S. I. Simak, A. Udías, H.-K. Mao, and R. Ahuja, "Hemispherical anisotropic patterns of the Earth's inner core," *Proc. Natl. Acad. Sci. USA*, vol. 107, pp. 9507–9512, 2010.

[8] T. Guillot, "Probing the Giant Planets," *Phys. Today*, pp. 63–69, 2004.

[9] D. J. Stevenson, "Gas and Ice Giant Interiors," in *Planets, Stars and Stellar Systems*, vol. 3, pp. 195–221, Dordrecht: Springer Netherlands, 2013.

[10] C. Cavazzoni, "Superionic and Metallic States of Water and Ammonia at Giant Planet Conditions," *Science*, vol. 283, pp. 44–46, 1999.

[11] H. F. Wilson, M. L. Wong, and B. Militzer, "Superionic to Superionic Phase Change in Water: Consequences for the Interiors of Uranus and Neptune," *Phys. Rev. Lett.*, vol. 110, p. 151102, 2013.

[12] B. Militzer and S. Zhang, "Ab initio simulations of novel superionic H2O, H2O2, and H9O4 compounds," *Phys. Rev. B*, 2016 (in revision).

[13] B. Militzer and S. Zhang, "Equation of states of water in giant-planet interiors," *Astrophys. J.*, 2016 (in preparation).

[14] http://kepler.nasa.gov/.

[15] S. Seager, M. J. Kuchner, C. A. Hier-Majumder, and B. Militzer, "Mass-Radius Relationships for Solid Exoplanets," *Astrophys. J.*, vol. 669, p. 1279, 2007.

[16] L. Zeng, D. Sasselov, and S. Jacobsen, "MASS-RADIUS RELATION FOR ROCKY PLANETS BASED ON PREM," *Astrophys. J.*, vol. 819, p. 127, 2016.

[17] J. Badro, A. S. Côté, and J. P. Brodholt, "A seismologically consistent compositional model of Earth's core," *Proc. Natl. Acad. Sci. USA*, vol. 111, pp. 7542–5, 2014.

[18] K. Hirose, S. Labrosse, and J. Hernlund, "Composition and State of the Core," *Annu. Rev. Earth Planet. Sci.*, vol. 41, pp. 657–691, 2013.

[19] J. G. O'Rourke and D. J. Stevenson, "Powering Earth's dynamo with magnesium precipitation from the core," *Nature*, vol. 529, pp. 387–389, 2016.

[20] G. Aquilanti, A. Trapananti, A. Karandikar, I. Kantor, C. Marini, O. Mathon, S. Pascarelli, and R. Boehler, "Melting of iron determined by X-ray absorption spectroscopy to 100 GPa," *Proc. Natl. Acad. Sci. USA*, vol. 112, pp. 12042–12045, 2015.

[21] K. Ohta, Y. Kuwayama, K. Hirose, K. Shimizu, and Y. Ohishi, "Experimental determination of the electrical resistivity of iron at Earth's core conditions," *Nature*, vol. 534, pp. 95–98, 2016.

[22] Z. Konôpková, R. S. McWilliams, N. Gómez-Pérez, and A. F. Goncharov, "Direct measurement of thermal conductivity in solid iron at planetary core conditions," *Nature*, vol. 534, pp. 99–101, 2016.

[23] B. Chen, J. M. Jackson, W. Sturhahn, D. Zhang, J. Zhao, J. K. Wicks, and C. A. Murphy, "Spin crossover equation of state and sound velocities of (Mg0.65Fe0.35)O ferropericlase to 140 GPa," *J. Geophys. Res.*, vol. 117, p. B08208, 2012.

[24] H. Marquardt, S. Speziale, H. J. Reichmann, D. J. Frost, F. R. Schilling, and E. J. Garnero, "Elastic shear anisotropy of ferropericlase in Earth's lower mantle," *Science*, vol. 324, pp. 224–6, 2009.

[25] J. Badro, G. Fiquet, F. Guyot, J.-P. Rueff, V. V. Struzhkin, G. Vankó, and G. Monaco, "Iron partitioning in Earth's mantle: toward a deep lower mantle discontinuity," *Science*, vol. 300, pp. 789–791, 2003.

[26] Z. Wu and R. M. Wentzcovitch, "Spin crossover in ferropericlase and velocity heterogeneities in the lower mantle," *Proc. Natl. Acad. Sci. USA*, 2014.

[27] W. Zhang, A. R. Oganov, A. F. Goncharov, Q. Zhu, S. E. Boulfelfel, A. O. Lyakhov, E. Stavrou, M. Somayazulu, V. B. Prakapenka, and Z. Konôpková, "Unexpected stable stoichiometries of sodium chlorides," *Science*, vol. 342, pp. 1502–1505, 2013.

[28] E. Ito, "Multi-Anvil Cells and High Pressure Experimental Methods," in *Treatise on Geophysics*, pp. 233–261, Elsevier, 2015.

[29] H. K. Mao and W. L. Mao, "Theory and Practice - Diamond-Anvil Cells and Probes for High P-T Mineral Physics Studies," in *Treatise on Geophysics*, pp. 231–267, Elsevier, 2007.

[30] T. J. Ahrens, "Shock Wave Experiments," in *Encyclopedia of Geomagnetism and Paleomagnetism* (D. Gubbins and E. Herrero-Bervera, eds.), pp. 912–920, Dordrecht: Springer Netherlands, 2003.

[31] R. M. Martin, *Electronic Structure : Basic Theory and Practical Methods*. Cambridge: Cambridge University Press, 2004.

[32] P. Hohenberg and W. Kohn, "Inhomogeneous Electron Gas," *Phys. Rev.*, vol. 136, pp. B864–871, 1964.

[33] W. Kohn and L. J. Sham, "Self-Consistent Equations Including Exchange and Correlation Effects," *Phys. Rev.*, vol. 140, pp. A1133–1138, 1965.

[34] J. P. Perdew and A. Zunger, "Self-interaction correction to density-functional approximations for many-electron systems," *Phys. Rev. B*, vol. 23, p. 5048, 1981.

[35] D. M. Ceperley and B. J. Alder, "Ground state of the electron gas by a stochastic method," *Phys. Rev. Lett.*, vol. 45, pp. 566–569, 1980.

[36] J. Kohanoff, *Electronic Structure Calculations for Solids and Molecules: Theory and Computational Methods*. Cambridge: Cambridge University Press, 2006.

[37] D. Alfè, "PHON: A program to calculate phonons using the small displacement method," *Comput. Phys. Commun.*, vol. 180, pp. 2622–2633, 2009.

[38] S. Baroni, S. de Gironcoli, A. Dal Corso, and P. Giannozzi, "Phonons and related crystal properties from density-functional perturbation theory," *Rev. Mod. Phys.*, vol. 73, pp. 515–562, 2001.

[39] R. M. Wentzcovitch, K. Umemoto, T. Tsuchiya, and J. Tsuchiya, "Thermodynamic Properties and Stability Field of MgSiO3 Post-Perovskite," in *Post-Perovskite: The Last Mantle Phase Transition*, pp. 79–97, 2007.

[40] R. Car and M. Parrinello, "Unified approach for molecular dynamics and density-functional theory," *Phys. Rev. Lett.*, vol. 55, pp. 2471–2474, 1985.

[41] N. D. Mermin, "Thermal Properties of the Inhomogeneous Electron Gas," *Phys. Rev.*, vol. 137, pp. A1441–A1443, 1965.

[42] G. A. De Wijs, G. Kresse, and M. J. Gillan, "First-order phase transitions by first-principles free-energy calculations: the melting of Al," *Phys. Rev. B*, vol. 57, pp. 8223–8234, 1998.

[43] R. P. Feynman, "Atomic theory of the λ transition in helium," *Phys. Rev.*, vol. 91, pp. 1291–1301, 1953.

[44] D. M. Ceperley, "Path integrals in the theory of condensed helium," *Rev. Mod. Phys.*, vol. 67, p. 279, 1995.

[45] D. M. Ceperley, "Fermion nodes," *J. Stat. Phys.*, vol. 63, pp. 1237–1267, 1991.

[46] B. Militzer, "Equation of state calculations of hydrogen-helium mixtures in solar and extrasolar giant planets," *Phys. Rev. B*, vol. 79, p. 155105, 2009.

[47] K. P. Driver and B. Militzer, "All-Electron Path Integral Monte Carlo Simulations of Warm Dense Matter: Application to Water and Carbon Plasmas," *Phys. Rev. Lett.*, vol. 108, p. 115502, 2012.

[48] K. P. Driver and B. Militzer, "First-Principles Equation of State Calculations of Warm Dense Nitrogen," *Phys. Rev. B*, vol. 93, p. 064101, 2016.

[49] K. P. Driver, F. Soubiran, S. Zhang, and B. Militzer, "First-principles equation of state and electronic properties of warm dense oxygen," *J. Chem. Phys.*, vol. 143, p. 164507, 2015.

[50] K. P. Driver and B. Militzer, "First-principles simulations and shock hugoniot calculations of warm dense neon," *Phys. Rev. B*, vol. 91, p. 045103, 2015.

[51] B. Militzer and K. P. Driver, "Development of path integral monte carlo simulations with localized nodal surfaces for second-row elements," *Phys. Rev. Lett.*, vol. 115, p. 176403, 2015.

[52] D. Alfè, M. Alfredsson, J. Brodholt, M. Gillan, M. Towler, and R. Needs, "Quantum Monte Carlo calculations of the structural properties and the B1-B2 phase transition of MgO," *Phys. Rev. B*, vol. 72, p. 014114, 2005.

[53] Y. Lin, R. E. Cohen, S. Stackhouse, K. P. Driver, B. Militzer, L. Shulenburger, and J. Kim, "Equations of state and stability of MgSiO3 perovskite and post-perovskite phases from quantum Monte Carlo simulations," *Phys. Rev. B*, vol. 90, p. 184103, 2014.

[54] K. Ohta, R. Cohen, K. Hirose, K. Haule, K. Shimizu, and Y. Ohishi, "Experimental and Theoretical Evidence for Pressure-Induced Metallization in FeO with Rocksalt-Type Structure," *Phys. Rev. Lett.*, vol. 108, p. 026403, 2012.

[55] D. Frenkel and B. Smit, *Understanding Molecular Simulation: From Algorithms to Applications*. San Diego: Academic, 2002.

[56] L. Vočadlo and D. Alfè, "Ab initio melting curve of the fcc phase of aluminum," *Phys. Rev. B*, vol. 65, p. 214105, 2002.

[57] M. A. Morales, E. Schwegler, D. Ceperley, C. Pierleoni, S. Hamel, and K. Caspersen, "Phase separation in hydrogen-helium mixtures at Mbar pressures," *Proc. Natl. Acad. Sci. USA*, vol. 106, pp. 1324–1329, 2009.

[58] H. F. Wilson and B. Militzer, "Sequestration of noble gases in giant planet interiors," *Phys. Rev. Lett.*, vol. 104, p. 121101, 2010.

[59] A. Samanta, M. A. Morales, and E. Schwegler, "Exploring the free energy surface using ab initio molecular dynamics," *J. Chem. Phys.*, vol. 144, p. 164101, 2016.

[60] C. J. Pickard and R. J. Needs, "Ab initio Random Structure Searching," *J. Phys. Condens. Matter*, vol. 23, p. 053201, 2011.

[61] C. W. Glass, A. R. Oganov, and N. Hansen, "USPEX-Evolutionary crystal structure prediction," *Comput. Phys. Commun.*, vol. 175, pp. 713–720, 2006.

[62] Y. Wang, J. Lv, L. Zhu, and Y. Ma, "CALYPSO: A method for crystal structure prediction," *Comput. Phys. Commun.*, vol. 183, pp. 2063–2070, 2012.

[63] D. C. Lonie and E. Zurek, "XtalOpt: An open-source evolutionary algorithm for crystal structure prediction," *Comput. Phys. Commun.*, vol. 182, pp. 372–387, 2011.

[64] T. Irifune, T. Shinmei, C. A. McCammon, N. Miyajima, D. C. Rubie, and D. J. Frost, "Iron partitioning and density changes of pyrolite in Earth's lower mantle," *Science*, vol. 327, pp. 193–195, 2010.

[65] S. Xu, S.-H. Shim, and D. Morgan, "Origin of Fe3+ in Fe-containing , Al-free mantle silicate perovskite," *Earth Planet. Sci. Lett.*, vol. 409, pp. 319–328, 2015.

[66] W. L. Mao, G. Shen, V. B. Prakapenka, Y. Meng, A. J. Campbell, D. L. Heinz, J. Shu, R. J. Hemley, and H.-k. Mao, "Ferromagnesian postperovskite silicates in the D″ layer of the Earth," *Proc. Natl. Acad. Sci. USA*, vol. 101, pp. 15867–15869, 2004.

[67] M. Murakami, Y. Ohishi, N. Hirao, and K. Hirose, "A perovskitic lower mantle inferred from high-pressure, high-temperature sound velocity data," *Nature*, vol. 485, pp. 90–4, 2012.

[68] Z. Zhang, L. Stixrude, and J. Brodholt, "Elastic properties of MgSiO3-perovskite under lower mantle conditions and the composition of the deep Earth," *Earth Planet. Sci. Lett.*, vol. 379, pp. 1–12, 2013.

[69] A. E. Ringwood, *Composition and Petrology of the Earth's Mantle.* New York: McGraw-Hill, 1975.

[70] K. K. M. Lee, B. O'Neill, W. R. Panero, S. H. Shim, L. R. Benedetti, and R. Jeanloz, "Equations of state of the high-pressure phases of a natural peridotite and implications for the Earth's lower mantle," *Earth Planet. Sci. Lett.*, vol. 223, pp. 381–393, 2004.

[71] A. R. Oganov, J. P. Brodholt, and G. D. Price, "Ab initio elasticity and thermal equation of state of MgSiO3 perovskite," *Earth Planet. Sci. Lett.*, vol. 184, pp. 555–560, 2001.

[72] R. Wentzcovitch, B. Karki, M. Cococcioni, and S. de Gironcoli, "Thermoelastic Properties of MgSiO3-Perovskite: Insights on the Nature of the Earth's Lower Mantle," *Phys. Rev. Lett.*, vol. 92, p. 018501, 2004.

[73] R. M. Wentzcovitch, T. Tsuchiya, and J. Tsuchiya, "MgSiO3 postperovskite at D″ conditions," *Proc. Natl. Acad. Sci. USA*, vol. 103, pp. 543–6, 2006.

[74] S. Stackhouse, J. P. Brodholt, J. Wookey, J.-M. Kendall, and G. D. Price, "The effect of temperature on the seismic anisotropy of the perovskite and post-perovskite polymorphs of MgSiO3," *Earth Planet. Sci. Lett.*, vol. 230, pp. 1–10, 2005.

[75] S. Stackhouse and J. P. Brodholt, "The High-Temperature Elasticity of MgSiO3 Post-Perovskite," in *Post-Perovskite: The Last Mantle Phase Transition*, pp. 99–113, 2007.

[76] B. Kiefer, L. Stixrude, and R. M. Wentzcovitch, "Elasticity of (Mg,Fe)SiO3 -Perovskite at high pressures," *Geophys. Res. Lett.*, vol. 29, p. 34, 2002.

[77] R. Caracas and R. E. Cohen, "Theoretical determination of the Raman spectra of MgSiO3 perovskite and post-perovskite at high pressure," *Geophys. Res. Lett.*, vol. 33, p. L12S05, 2006.

[78] L. Li, J. Brodholt, S. Stackhouse, D. Weidner, M. Alfredsson, and G. Price, "Elasticity of (Mg, Fe)(Si, Al)O3-perovskite at high pressure," *Earth Planet. Sci. Lett.*, vol. 240, pp. 529–536, 2005.

[79] S. Stackhouse, J. P. Brodholt, D. P. Dobson, and G. D. Price, "Electronic spin transitions and the seismic properties of ferrous iron-bearing MgSiO3 post-perovskite," *Geophys. Res. Lett.*, vol. 33, p. L12S03, 2006.

[80] S. Stackhouse, J. P. Brodholt, and G. D. Price, "Electronic spin transitions in iron-bearing MgSiO3 perovskite," *Earth Planet. Sci. Lett.*, vol. 253, pp. 282–290, 2007.

[81] T. Tsuchiya and J. Tsuchiya, "Effect of impurity on the elasticity of perovskite and postperovskite: Velocity contrast across the postperovskite transition in (Mg,Fe,Al)(Si,Al)O3," *Geophys. Res. Lett.*, vol. 33, p. L12S04, 2006.

[82] J. Badro, J.-P. Rueff, G. Vankó, G. Monaco, G. Fiquet, and F. Guyot, "Electronic transitions in perovskite: possible nonconvecting layers in the lower mantle," *Science*, vol. 305, pp. 383–386, 2004.

[83] F. Zhang and A. R. Oganov, "Mechanisms of Al3+ incorporation in MgSiO3 postperovskite at high pressures," *Earth Planet. Sci. Lett.*, vol. 248, pp. 69–76, 2006.

[84] J. P. Brodholt, "Pressure-induced changes in the compression mechanism of aluminous perovskite in the Earth's mantle," *Nature*, vol. 407, pp. 620–622, 2000.

[85] H. Hsu, K. Umemoto, M. Cococcioni, and R. M. Wentzcovitch, "The Hubbard U correction for iron-bearing minerals: A discussion based on (Mg,Fe)SiO3 perovskite," *Phys. Earth Planet. Inter.*, vol. 185, pp. 13–19, 2011.

[86] Y. Yu, H. Hsu, M. Cococcioni, and R. M. Wentzcovitch, "Spin states and hyperfine interactions of iron incorporated in MgSiO3 post-perovskite," *Earth Planet. Sci. Lett.*, vol. 331-332, pp. 1–7, 2012.

[87] F. Zhang and A. R. Oganov, "Valence state and spin transitions of iron in Earth's mantle silicates," *Earth Planet. Sci. Lett.*, vol. 249, pp. 436–443, 2006.

[88] L. Li, J. P. Brodholt, S. Stackhouse, D. J. Weidner, M. Alfredsson, and G. D. Price, "Electronic spin state of ferric iron in Al-bearing perovskite in the lower mantle," *Geophys. Res. Lett.*, vol. 32, p. L17307, 2005.

[89] H. Hsu, P. Blaha, M. Cococcioni, and R. M. Wentzcovitch, "Spin-State Crossover and Hyperfine Interactions of Ferric Iron in MgSiO3 Perovskite," *Phys. Rev. Lett.*, vol. 106, p. 118501, 2011.

[90] H. Hsu, Y. G. Yu, and R. M. Wentzcovitch, "Spin crossover of iron in aluminous MgSiO3 perovskite and post-perovskite," *Earth Planet. Sci. Lett.*, vol. 359-360, pp. 34–39, 2012.

[91] A. Metsue and T. Tsuchiya, "Lattice dynamics and thermodynamic properties of (Mg,Fe2+)SiO3 postperovskite," *J. Geophys. Res.*, vol. 116, p. B08207, 2011.

[92] T. Tsuchiya and X. Wang, "Ab initio investigation on the high-temperature thermodynamic properties of Fe3+-bearing MgSiO3 perovskite," *J. Geophys. Res.*, vol. 118, pp. 83–91, 2013.

[93] G. Shukla, Z. Wu, H. Hsu, A. Floris, M. Cococcioni, and R. M. Wentzcovitch, "Thermoelasticity of Fe2+-bearing bridgmanite," *Geophys. Res. Lett.*, vol. 42, pp. 1741–1749, 2015.

[94] J. M. R. Muir and J. P. Brodholt, "Elastic properties of ferrous bearing MgSiO3 and their relevance to ULVZs," *Geophys. J. Int.*, vol. 201, pp. 496–504, 2015.

[95] S. Zhang, S. Cottaar, T. Liu, S. Stackhouse, and B. Militzer, "High-pressure, temperature elasticity of Fe- and Al-bearing MgSiO3: implications for the Earth's lower mantle," *Earth Planet. Sci. Lett.*, vol. 434, pp. 264–273, 2016.

[96] G. Kresse and J. Furthmüller, "Efficient iterative schemes for ab initio total-energy calculations using a plane-wave basis set," *Phys. Rev. B*, vol. 54, p. 11169, 1996.

[97] P. E. Blöchl, O. Jepsen, and O. K. Andersen, "Improved tetrahedron method for brillouin-zone integrations," *Phys. Rev. B*, vol. 49, pp. 16223–16233, 1994.

[98] S. Stackhouse, L. Stixrude, and B. B. Karki, "Determination of the high-pressure properties of fayalite from first-principles calculations," *Earth Planet. Sci. Lett.*, vol. 289, pp. 449–456, 2010.

[99] H. J. Monkhorst and J. D. Pack, "Special points for Brillouin-zone integrations," *Phys. Rev. B*, vol. 13, p. 5188, 1976.

[100] S. Nosé, "A unified formulation of the constant temperature molecular dynamics methods," *J. Chem. Phys.*, vol. 81, pp. 511–519, 1984.

[101] R. Caracas, H. Ozawa, K. Hirose, H. Ishii, N. Hiraoka, Y. Ohishi, and N. Hirao, "Identifying the spin transition in Fe2+-rich MgSiO3 perovskite from X-ray diffraction and vibrational spectroscopy," *Am. Mineral.*, vol. 99, pp. 1270–1276, 2014.

[102] G. Shukla and R. M. Wentzcovitch, "Spin crossover in (Mg,Fe3+)(Si,Fe3+)O3 bridgmanite: effects of disorder, iron concentration, and temperature," *arXiv:1603.08947*, 2016.

[103] B. Militzer, H.-R. Wenk, S. Stackhouse, and L. Stixrude, "First-principles calculation of the elastic moduli of sheet silicates and their application to shale anisotropy," *Am. Mineral.*, vol. 96, pp. 125–137, 2011.

[104] D. C. Wallace, *Thermodynamics of Crystals*. New York: Wiley, 1972.

[105] R. Caracas, "Spin and structural transitions in AlFeO3 and FeAlO3 perovskite and post-perovskite," *Phys. Earth Planet. Inter.*, vol. 182, pp. 10–17, 2010.

[106] K. Catalli, S.-H. Shim, P. Dera, V. B. Prakapenka, J. Zhao, W. Sturhahn, P. Chow, Y. Xiao, H. Cynn, and W. J. Evans, "Effects of the Fe3+ spin transition on the properties of aluminous perovskiteNew insights for lower-mantle seismic heterogeneities," *Earth Planet. Sci. Lett.*, vol. 310, pp. 293–302, 2011.

[107] K. Fujino, D. Nishio-Hamane, T. Nagai, Y. Seto, Y. Kuwayama, M. Whitaker, H. Ohfuji, T. Shinmei, and T. Irifune, "Spin transition, substitution, and partitioning of iron in lower mantle minerals," *Phys. Earth Planet. Inter.*, vol. 228, pp. 186–191, 2014.

[108] A. R. Oganov and S. Ono, "Theoretical and experimental evidence for a post-perovskite phase of MgSiO3 in Earth's D″ layer," *Nature*, vol. 430, pp. 445–448, 2004.

[109] T. Tsuchiya, J. Tsuchiya, K. Umemoto, and R. M. Wentzcovitch, "Phase transition in MgSiO3 perovskite in the earth's lower mantle," *Earth Planet. Sci. Lett.*, vol. 224, pp. 241–248, 2004.

[110] S.-H. Shim, "The Postperovskite Transition," *Annu. Rev. Earth Planet. Sci.*, vol. 36, pp. 569–599, 2008.

[111] Z. Wu, J. F. Justo, and R. M. Wentzcovitch, "Elastic Anomalies in a Spin-Crossover System: Ferropericlase at Lower Mantle Conditions," *Phys. Rev. Lett.*, vol. 110, p. 228501, 2013.

[112] J. M. Brown and T. J. Shankland, "Thermodynamic parameters in the Earth as determined from seismic profiies," *Geophys. J. R. Astron. Soc.*, vol. 66, pp. 579–596, 1981.

[113] S. Cottaar, M. Li, A. K. McNamara, B. Romanowicz, and H.-R. Wenk, "Synthetic seismic anisotropy models within a slab impinging on the core-mantle boundary," *Geophys. J. Int.*, vol. 199, pp. 164–177, 2014.

[114] L. Stixrude and C. Lithgow-Bertelloni, "Thermodynamics of mantle minerals - II. Phase equilibria," *Geophys. J. Int.*, vol. 184, pp. 1180–1213, 2011.

[115] A. M. Dziewonski and D. L. Anderson, "Preliminary reference Earth model," *Phys. Earth Planet. Inter.*, vol. 25, pp. 297–356, 1981.

[116] A. M. Walker and J. Wookey, "MSAT-A new toolkit for the analysis of elastic and seismic anisotropy," *Comput. Geosci.*, vol. 49, pp. 81–90, 2012.

[117] T. Komabayashi, K. Hirose, Y. Nagaya, E. Sugimura, and Y. Ohishi, "High-temperature compression of ferropericlase and the effect of temperature on iron spin transition," *Earth Planet. Sci. Lett.*, vol. 297, pp. 691–699, 2010.

[118] L. Vedran, S. Cottaar, A. Dziewonski, and B. Romanowicz, "Cluster analysis of global lower mantle tomography: A new class of structure and implications for chemical heterogeneity," *Earth Planet. Sci. Lett.*, vol. 68, pp. 68–77, 2012.

[119] M. Ishii and J. Tromp, "Normal-Mode and Free-Air Gravity Constraints on Lateral Variations in Velocity and Density of Earth's Mantle," *Science*, vol. 285, pp. 1231–1236, 1999.

[120] N. A. Simmons, A. M. Forte, L. Boschi, and S. P. Grand, "GyPSuM: A joint tomographic model of mantle density and seismic wave speeds," *J. Geophys. Res.*, vol. 115, p. B12310, 2010.

[121] J. Trampert, F. Deschamps, J. Resovsky, and D. Yuen, "Probabilistic tomography maps chemical heterogeneities throughout the lower mantle," *Science*, vol. 306, pp. 853–856, 2004.

[122] S. Cottaar, T. Heister, I. Rose, and C. Unterborn, "BurnMan: A lower mantlemineral physics toolkit Sanne," *Geochem. Geophys. Geosyst.*, vol. 15, pp. 1164–1179, 2014.

[123] R. A. Lebensohn and C. N. Tomé, "A self-consistent anisotropic approach for the simulation of plastic deformation and texture development of polycrystals: Application to zirconium alloys," *Acta Metall. Mater.*, vol. 41, pp. 2611–2624, 1993.

[124] G. Fiquet, A. Dewaele, D. Andrault, and M. Kunz, "Thermoelastic properties and crystal structure of MgSiO perovskite at lower mantle pressure and temperature conditions," *Geophys. Res. Lett.*, vol. 27, pp. 21–24, 2000.

[125] S. R. Shieh, T. S. Duffy, A. Kubo, G. Shen, V. B. Prakapenka, N. Sata, K. Hirose, and Y. Ohishi, "Equation of state of the postperovskite phase synthesized from a natural (Mg,Fe)SiO3 orthopyroxene," *Proc. Natl. Acad. Sci. USA*, vol. 103, pp. 3039–3043, 2005.

[126] F. Birch, "Finite strain isotherm and velocities for single-crystal and polycrystalline nacl at high pressures and 300°K," *J. Geophys. Res.*, vol. 83, pp. 1257–1268, 1978.

[127] P. Vinet, J. Ferrante, J. H. Rose, and J. R. Smith, "Compressibility of solids," *J. Geophys. Res.*, vol. 92, pp. 9319–9325, 1987.

[128] T. Komabayashi, K. Hirose, E. Sugimura, N. Sata, Y. Ohishi, and L. S. Dubrovinsky, "Simultaneous volume measurements of post-perovskite and perovskite in MgSiO3 and their thermal equations of state," *Earth Planet. Sci. Lett.*, vol. 265, pp. 515–524, 2008.

[129] Y. Tange, Y. Kuwayama, T. Irifune, K. I. Funakoshi, and Y. Ohishi, "P-V-T equation of state of MgSiO3 perovskite based on the MgO pressure scale: A comprehensive reference for mineralogy of the lower mantle," *J. Geophys. Res.*, vol. 117, p. B06201, 2012.

[130] S. M. Dorfman and T. S. Duffy, "Effect of Fe-enrichment on seismic properties of perovskite and post-perovskite in the deep lower mantle," *Geophys. J. Int.*, vol. 197, pp. 910–919, 2014.

[131] A. Polian and M. Grimsditch, "New High-Pressure of H2O: Ice X," *Phys. Rev. Lett.*, vol. 52, pp. 1312–1314, 1984.

[132] M. Benoit, M. Bernasconi, P. Focher, and M. Parrinello, "New High-Pressure Phase of Ice," *Phys. Rev. Lett.*, vol. 76, pp. 2934–2936, 1996.

[133] W. B. Hubbard, *Planetary Interiors*. Tucson, AZ: University of Arizona Press, 1984.

[134] B. Militzer and H. F. Wilson, "New phases of water ice predicted at megabar pressures," *Phys. Rev. Lett.*, vol. 105, p. 195701, 2010.

[135] Y. Wang, H. Liu, J. Lv, L. Zhu, H. Wang, and Y. Ma, "High pressure partially ionic phase of water ice," *Nature Commun.*, vol. 2, p. 563, 2011.

[136] J. M. McMahon, "Ground-state structures of ice at high pressures from ab initio random structure searching," *Phys. Rev. B*, vol. 84, p. 220104, 2011.

[137] M. Ji, K. Umemoto, C.-Z. Wang, K.-M. Ho, and R. M. Wentzcovitch, "Ultrahigh-pressure phases of H2O ice predicted using an adaptive genetic algorithm," *Phys. Rev. B*, vol. 84, p. 220105, 2011.

[138] A. Hermann, N. W. Ashcroft, and R. Hoffmann, "High pressure ices," *Proc. Natl. Acad. Sci. USA*, vol. 109, pp. 745–750, 2012.

[139] K. Umemoto and R. M. Wentzcovitch, "Two-stage dissociation in MgSiO3 post-perovskite," *Earth Planet. Sci. Lett.*, vol. 311, pp. 225–229, 2011.

[140] C. J. Pickard and R. J. Needs, "High-pressure phases of silane," *Phys. Rev. Lett.*, vol. 97, p. 045504, 2006.

[141] C. J. Pickard and R. J. Needs, "Highly compressed ammonia forms an ionic crystal," *Nature Mater.*, vol. 7, pp. 775–9, 2008.

[142] A. J. Morris, C. J. Pickard, and R. J. Needs, "Hydrogen/nitrogen/oxygen defect complexes in silicon from computational searches," *Phys. Rev. B*, vol. 80, p. 144112, 2009.

[143] A. D. Fortes, E. Suard, M.-H. Lemée-Cailleau, C. J. Pickard, and R. J. Needs, "Crystal structure of ammonia monohydrate phase ii," *J. Am. Chem. Soc.*, vol. 131, pp. 13508–13515, 2009.

[144] G. Kresse and J. Furthmüller, "Efficiency of ab-initio total energy calculations for metals and semiconductors using a plane-wave basis set," *Comput. Mater. Sci.*, vol. 6, p. 15, 1996.

[145] G. Kresse and D. Joubert, "From ultrasoft pseudopotentials to the projector augmented-wave method," *Phys. Rev. B*, vol. 59, p. 1758, 1999.

[146] J. P. Perdew, K. Burke, and M. Ernzerhof, "Generalized Gradient Approximation Made Simple," *Phys. Rev. Lett.*, vol. 77, p. 3865, 1996.

[147] J. D. Pack and H. J. Monkhorst, "'special points for brillouin-zone integrations'—a reply," *Phys. Rev. B*, vol. 16, p. 1748, 1977.

[148] M. Martinez-Canales, C. Pickard, and R. Needs, "Thermodynamically Stable Phases of Carbon at Multiterapascal Pressures," *Phys. Rev. Lett.*, vol. 108, p. 045704, 2012.

[149] J. Sun, M. Martinez-Canales, D. Klug, C. Pickard, and R. Needs, "Persistence and Eventual Demise of Oxygen Molecules at Terapascal Pressures," *Phys. Rev. Lett.*, vol. 108, p. 045503, 2012.

[150] H. Liu, H. Wang, and Y. Ma, "Quasi-Molecular and Atomic Phases of Dense Solid Hydrogen," *J. Phys. Chem. C*, vol. 116, pp. 9221–9226, 2012.

[151] J. M. McMahon and D. M. Ceperley, "Zero-Temperature Structures of Atomic Metallic Hydrogen," *Phys. Rev. Lett.*, vol. 106, p. 165302, 2011.

[152] H. Y. Geng, H. X. Song, J. F. Li, and Q. Wu, "High-pressure behavior of dense hydrogen up to 3.5 TPa from density functional theory calculations," *J. Appl. Phys.*, vol. 111, p. 063510, 2012.

[153] I. Opahle, G. K. H. Madsen, and R. Drautz, "High throughput density functional investigations of the stability, electronic structure and thermoelectric properties of binary silicides," *Phys. Chem. Chem. Phys.*, vol. 14, pp. 16197–16202, 2012.

[154] H. F. Wilson and B. Militzer, "Solubility of Water Ice in Metallic Hydrogen: Consequences for Core Erosion in Gas Giant Planets," *Astrophys. J.*, vol. 745, p. 54, 2012.

[155] http://elk.sourceforge.net/.

[156] R. C. Clay, J. McMinis, J. M. McMahon, C. Pierleoni, D. M. Ceperley, and M. A. Morales, "Benchmarking exchange-correlation functionals for hydrogen at high pressures using quantum Monte Carlo," *Phys. Rev. B*, vol. 89, p. 184106, 2014.

[157] F. Ancilotto, G. L. Chiarotti, S. Scandolo, and E. Tosatti, "Dissociation of Methane into Hydrocarbons at Extreme (Planetary) Pressure and Temperature," *Science*, vol. 275, pp. 1288–1290, 1997.

[158] E. Gregoryanz, L. F. Lundegaard, M. I. McMahon, C. Guillaume, R. J. Nelmes, and M. Mezouar, "Structural diversity of sodium," *Science*, vol. 320, pp. 1054–1057, 2008.

[159] A. Lazicki, A. F. Goncharov, V. V. Struzhkin, R. E. Cohen, Z. Liu, E. Gregoryanz, C. Guillaume, H.-K. Mao, and R. J. Hemley, "Anomalous optical and electronic properties of dense sodium," *Proc. Natl. Acad. Sci. USA*, vol. 106, pp. 6525–6528, 2009.

[160] J. Ibañez Azpiroz, B. Rousseau, A. Eiguren, and A. Bergara, "Ab initio analysis of plasmon dispersion in sodium under pressure," *Phys. Rev. B*, vol. 89, p. 085102, 2014.

[161] M. Marqués, M. Santoro, C. L. Guillaume, F. A. Gorelli, J. Contreras-García, R. T. Howie, A. F. Goncharov, and E. Gregoryanz, "Optical and electronic properties of dense sodium," *Phys. Rev. B*, vol. 83, p. 184106, 2011.

[162] H. Eshet, R. Z. Khaliullin, T. D. Kühne, J. Behler, and M. Parrinello, "Microscopic origins of the anomalous melting behavior of sodium under high pressure," *Phys. Rev. Lett.*, vol. 108, p. 115701, 2012.

[163] M.-s. Miao and R. Hoffman, "High-Pressure Electrides: The Chemical Nature of Interstitial Quasiatoms," *J. Am. Chem. Soc.*, vol. 137, pp. 3631–3637, 2015.

[164] Y. Li, Y. Wang, C. J. Pickard, R. J. Needs, Y. Wang, and Y. Ma, "Metallic Icosahedron Phase of Sodium at Terapascal Pressures," *Phys. Rev. Lett.*, vol. 114, p. 125501, 2015.

[165] I. I. Naumov and R. J. Hemley, "Origin of Transitions between Metallic and Insulating States in Simple Metals," *Phys. Rev. Lett.*, vol. 114, p. 156403, 2015.

[166] J. N. Bahcall and M. H. Pinsonneault, "What do we (not) know theoretically about solar neutrino fluxes?," *Phys. Rev. Lett.*, vol. 92, p. 121301, 2004.

[167] http://opium.sourceforge.net.

[168] http://www.msg.ameslab.gov/gamess/.

[169] http://www.crystallography.net/cod/9008545.html.

[170] S. P. Lyon and J. D. Johnson, eds., *SESAME: The Los Alamos National Laboratory Equation of State Database*. Group T-1, Report No. LA-UR-92-3407, 1992.

[171] B. F. Rozsnyai, J. R. Albritton, D. A. Young, V. N. Sonnad, and D. A. Liberman, "Theory and experiment for ultrahigh pressure shock Hugoniots," *Phys. Lett. A*, vol. 291, pp. 226–231, 2001.

[172] S. T. Stewart and S. J. Lock, "The Thermal States of Accreting Planets: From Mars-like Embryos to a MAD Earth," AGU Fall Meeting MR21D-02, 2015.

[173] L. J. Hallis, G. R. Huss, K. Nagashima, G. J. Taylor, S. A. Halldórsson, D. R. Hilton, M. J. Mottl, and K. J. Meech, "Evidence for primordial water in Earth's deep mantle," *Science*, vol. 350, p. 795, 2015.

[174] C. Sanchez-Valle, F. Gaillard, S. Ghosh, and K. Mezger, "Fluids and melts in planetary interiors: From crust to core-mantle boundaries," *Chem. Geol.*, vol. 418, pp. 1–5, 2015.

[175] M. G. Pamato, R. Myhill, T. Boffa Ballaran, D. J. Frost, F. Heidelbach, and N. Miyajima, "Lower-mantle water reservoir implied by the extreme stability of a hydrous aluminosilicate," *Nature Geosci.*, vol. 8, pp. 75–79, 2014.

[176] J. Tsuchiya and M. Mookherjee, "Crystal structure, equation of state, and elasticity of phase H (MgSiO4H2) at Earth's lower mantle pressures," *Sci. Rep.*, vol. 5, p. 15534, 2015.

[177] E. Ohtani, Y. Amaike, S. Kamada, I. Ohira, and I. Mashino, "Stability of Hydrous Minerals and Water Reservoirs in the Deep Earth Interior," in *Deep Earth: Physics and Chemistry of the Lower Mantle and Core* (H. Terasaki and R. A. Fischer, eds.), ch. 21, pp. 265–275, John Wiley & Sons, Inc., 2016.

[178] E. R. Hernández, D. Alfè, and J. Brodholt, "The incorporation of water into lower-mantle perovskites: A first-principles study," *Earth Planet. Sci. Lett.*, vol. 364, pp. 37–43, 2013.

[179] H. F. Wilson and B. Militzer, "Rocky Core Solubility in Jupiter and Giant Exoplanets," *Phys. Rev. Lett.*, vol. 108, p. 111101, 2012.

[180] S. Labrosse, J. W. Hernlund, and N. Coltice, "A crystallizing dense magma ocean at the base of the Earth's mantle," *Nature*, vol. 450, pp. 866–869, 2007.

[181] N. Coltice, M. Moreira, J. Hernlund, and S. Labrosse, "Crystallization of a basal magma ocean recorded by Helium and Neon," *Earth Planet. Sci. Lett.*, vol. 308, pp. 193–199, 2011.

[182] E. Anders and T. Owen, "Mars and Earth: Origin and Abundance of Volatiles," *Science*, vol. 198, pp. 453–465, 1977.

[183] S. S. Shcheka and H. Keppler, "The origin of the terrestrial noble-gas signature," *Nature*, vol. 390, pp. 531–534, 2012.

[184] G. Holland and C. J. Ballentine, "Seawater subduction controls the heavy noble gas composition of the mantle," *Nature*, vol. 441, pp. 186–191, 2006.

[185] D. Seoung, Y. Lee, H. Cynn, C. Park, K.-Y. Choi, D. a. Blom, W. J. Evans, C.-C. Kao, T. Vogt, and Y. Lee, "Irreversible xenon insertion into a small-pore zeolite at moderate pressures and temperatures," *Nature Chem.*, vol. 6, pp. 835–839, 2014.

[186] R. M. G. Armytage, A. P. Jephcoat, M. A. Bouhifd, and D. Porcelli, "Metal-silicate partitioning of iodine at high pressures and temperatures: Implications for the Earth's core and 129*Xe budgets," *Earth Planet. Sci. Lett.*, vol. 373, pp. 140–149, 2013.

[187] K. K. M. Lee and G. Steinle-Neumann, "High-pressure alloying of iron and xenon: "Missing" Xe in the Earth's core?," *J. Geophys. Res.*, vol. 111, p. B02202, 2006.

[188] D. Nishio-Hamane, T. Yagi, N. Sata, T. Fujita, and T. Okada, "No reactions observed in Xe-Fe system even at Earth core pressures," *Geophys. Res. Lett.*, vol. 37, pp. 35–38, 2010.

[189] Q. Zhu, D. Y. Jung, A. R. Oganov, C. W. Glass, C. Gatti, and A. O. Lyakhov, "Stability of xenon oxides at high pressures," *Nature Chem.*, vol. 5, pp. 61–65, 2013.

[190] S. Klotz, J.-C. Chervin, P. Munsch, and G. Le Marchand, "Hydrostatic limits of 11 pressure transmitting media," *J. Phys. D: Appl. Phys.*, vol. 42, p. 075413, 2009.

[191] R. Sinmyo and K. Hirose, "The Soret diffusion in laser-heated diamond-anvil cell," *Phys. Earth Planet. Inter.*, vol. 180, pp. 172–178, 2010.